Faculty of Electrical Engineering, Mathematics and Computer Science
Transducers Science and Technology

Modeling, design, fabrication and characterization of a biomimetic angular acceleration sensor

J.A.J. van Tiem, BSc

Master Thesis
Electrical Engineering

Supervisors
ir. J. Groenesteijn
prof. dr. ir. G.J.M. Krijnen
prof. dr. J.C.T. Eijkel
dr. ir. R.J. Wiegerink

December 2014

UNIVERSITY OF TWENTE.

Abstract

This thesis describes the modeling, design, fabrication and characterization of a micromachined and a 3D printed angular acceleration sensor inspired by the human vestibular system. Both sensors comprise a fully circular channel filled with water. When the sensor is subjected to an angular acceleration, the fluid will start to move relative to the channel due to its inertia. This fluid movement is sensed.

The micromachined sensor uses thermal readout principles. This technique measures the flow velocity by means of heat convection through the liquid. An analytical model describing the sensor in the space and frequency domain has been constructed and is in accordance with numerical simulations. A variety of designs has been made and the sensors have been fabricated successfully.

Electromagnetic flow sensing is used in the 3D printed sensors. This principle of flow measurement is based on the potential difference that arises when a conducting liquid moves through a magnetic field. An analytical model describing the physics of the sensor has been constructed. Electromagnetic readout has been demonstrated for an alternating magnetic field.

Contents

Nomenclature

Symbols with a bar ($\vec{v}$) denote vectors, hat symbols ($\hat{n}$) denote unit vectors and normal symbols (ρ) denote scalars. When possible, the symbol common in literature is used. Therefore, sometimes one symbol is used for two different quantities. This is indicated in this table by one symbol with multiple descriptions.

Symbol	Description	Unit
α	Angular acceleration	s^{-2}
α_R	Temperature coefficient of resistance	K^{-1}
A	Area	m^2
β	Coefficient, equal to $\rho c_p v/k$	m^{-1}
$\vec{B}$	Magnetic flux density	T
B_r	Remanence	T
c_p	Heat capacity	$J\,kg^{-1}K^{-1}$
c_b	Bulk ion concentration	$mol\,m^{-3}$
C_H	Fluidic capacitance	$m^3\,Pa^{-1}$
γ	Angle	rad
δ	Boundary layer thickness	m
δT	Temperature difference	K
d	Diameter	m
$\vec{D}$	Electric displacement field	$C\,m^2$
D	Height (of the magnet)	m
$\hat{e}_z$	Unit vector in the axial direction	-
ϵ	Permittivity	$F\,m^{-1}$
E	Young's modulus	Pa
$\vec{E}$	Electric field	$V\,m^{-1}$
ζ	Frequency dependent coefficient equal to $\sqrt{\rho c_p \omega/2k}$	m^{-1}
	Zeta potential	V
ϕ	Angle	rad
$\vec{F}_L$	Lorentz force	N
f	Body force	$N\,m^{-3}$
	Frequency	Hz
i	Current	A
i_s	Streaming current	A
i_c	Current	A
j	(Heat) flux	$W\,m^{-2}$
	Imaginary unit: $j^2 \equiv -1$	-
$\vec{j}$	Current density	$A\,m^{-2}$
$\vec{j}_D$	Displacement current density	$A\,m^{-2}$
k	Thermal conductivity	$W\,m^{-1}K^{-1}$

k_b	Boltzmann constant	$m^2\ kg\ s^{-2} K^{-1}$
k_{eff}	Effective thermal conductivity	$W\ m^{-1} K^{-1}$
κ_D	Reciprocal debye length	m^{-1}
L	Length	m
L_H	Fluidic inductance	$kg\ m^{-4}$
μ	Dynamic viscosity	Pa s
	Permeability	$H\ m^{-1}$
ν	Kinematic viscosity	$m^2\ s^{-1}$
	Poisson ratio	-
$\hat{n}$	Unit vector in the normal direction	-
N_A	Avogrado's number	mol^{-1}
p	Pressure	Pa
P	Power	W
q	Charge	C
Q	Heat source	$W\ m^{-3}$
r	Component in the radial direction	m
R	Radius	m
	Resistance	Ω
R_c	System radius	m
R_H	Fluidic resistance	$Pa\ s\ m^{-3}$
R_s	Skin depth	m
Re	Reynold's number	-
ρ	Density	$kg\ m^{-3}$
	Integration dummy variable	m
σ	Conductivity	$S\ m^{-1}$
S	Responsivity	[1]
t	Time	s
T	Temperature	K
U	Potential	V
v	Velocity	$m\ s^{-1}$
V	Potential	V
V_{sp}	Streaming potential	V
x_h	Position of the heater	m
ω	Angular frequency	s^{-1}
$\vec{\Omega}$	Angular velocity vector	s^{-1}

[1] S has been defined for multiple situations. The unit therefore depends on the situation.

Chapter 1

Introduction

This thesis describes the development of an angular acceleration sensor that is inspired by the human vestibular system. This system is composed of two parts, one to sense linear accelerations and one to sense angular accelerations. The latter consists of three semicircular channels that sense angular accelerations in three planes. Each semicircular channel is filled with a fluid and the two ends are connected to a compartment containing hair cells. When the system is rotating, the fluid will start to move relative to the channel due to its inertia. This movement is sensed by the hair cells that send a signal to the brain [1]. The sensors described in this thesis mimic the human vestibular system. Their basic geometry is designed to be a fully circular channel.

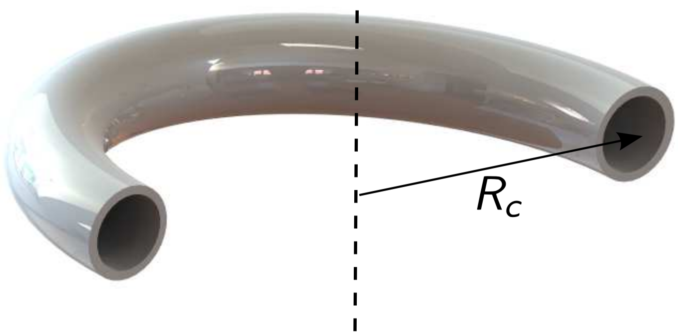

FIGURE 1.1: The geometry of the sensors in this thesis mimic the human vestibular system. A fully circular, torus shaped channel with system radius R_c is used.

The flow velocity in the channel depends linearly on the applied angular acceleration, which makes it an excellent instrument to measure angular acceleration. The main advantage of this geometry is that it is not sensitive to linear accelerations. In order to actually *measure* the flow velocity two readout techniques are used: thermal and electromagnetic.

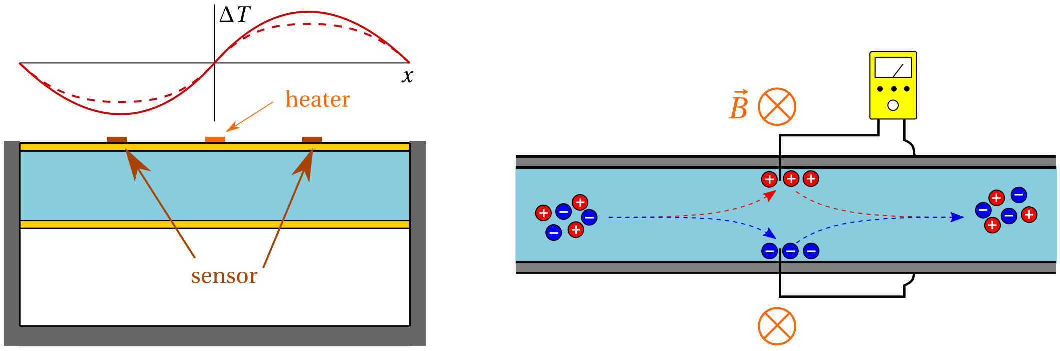

(a) Thermal readout (b) Electromagnetic readout

FIGURE 1.2: Two readout principles to measure the flow velocity are used in this thesis: thermal and electromagnetic.

Thermal readout exploits the (linear) relation between temperature and resistance of a resistor. Let us consider three resistors, one at the left, center and right, and heat the center one. Next, if we apply a flow to it, the resistor left of the center one (upstream) will cool down slightly whereas the resistor at the right (downstream) will heat up. The change in resistance is a measure for the change is temperature, which is in turn a measure for the flow velocity. From that, we can calculate the angular acceleration using the linear relation between angular acceleration and flow velocity. The principle of thermal readout has proved to be an effective readout mechanism in (micro) flow sensors [2–5].

The force acting on a charge in a magnetic field, the Lorentz force, is the basis of electromagnetic readout. When a magnetic field is applied to a moving (conducting) liquid, the positive ions will be deflected one way whereas the negative ones will move in the opposite direction. Because the ions are separated an electric field builds up and hence a potential difference over the channel. The latter can be measured using electrodes in the fluid. This effect is very similar to the well known *Hall*-effect in metal conductors [6, 7].

Electromagnetic readout is commercially used in meso- and macroscopic applications. The principle has been used in a micromachined chip by e.g. Yoon et al. in 2000 [8], but has, to the best of our knowledge, never been used in an angular acceleration sensor.

First, the fluid dynamics of the fluid inside the channel is studied, since it is the same for both sensors. Next, the physics for the thermal and electromagnetic readout is modeled to obtain the optimal sensor design. Finally, the sensors are fabricated and characterized.

Chapter 2

Fluid dynamics

To understand the physics of the sensor it is important to consider the fluid dynamics inside the channel in the space, time and frequency domain. The flow profile inside the channel can be described by the Navier-Stokes equations for incompressible flow [9]:

$$\rho\left(\frac{\partial \vec{v}}{\partial t} + (\vec{v}\cdot\nabla)\vec{v}\right) = -\nabla p + \mu\nabla^2\vec{v} + \vec{f} \tag{2.1}$$

In which $\vec{v}$ is the flow velocity, p the pressure, μ the viscosity of the fluid, and $\vec{f}$ a body force[1]. In order to characterize the sensor, we need to apply an angular acceleration. To do so, the sensor can be rotated harmonically with an angle $\phi(t) = \phi_0 \exp(j\omega t)$. This is illustrated graphically in Figure 2.1.

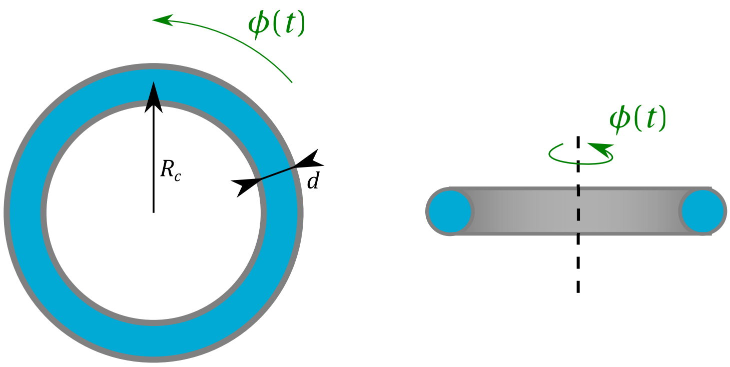

FIGURE 2.1: Left: top view, right: cross sectional view. The sensor, which has a system radius R_c and a channel diameter d, rotates harmonically with angle $\phi(t)$.

The body force is the force that drives the fluid movement. Since the fluid movement is sensed in the channel, we would like to describe the fluid dynamics with respect to the channel. This reference frame is moving with respect to the reference frame of the torus, so we need to define the acceleration $\vec{a}'$ in the rotating reference frame, i.e. the reference of the channel. The acceleration transformation formula reads [10]:

[1] $[\vec{f}] = \mathrm{N\,m^{-3}}$

$$\vec{a}' = \vec{a} - 2\vec{\Omega} \times \vec{v}' - \vec{\Omega} \times (\vec{\Omega} \times \vec{r}') - \frac{d\vec{\Omega}}{dt} \times \vec{r}' \tag{2.2}$$

In which $\vec{\Omega}$ denotes the angular velocity vector, $\vec{v}$ the velocity and $\vec{r} = \vec{r}_0 + \vec{r}_c$ the position vector. Parameters with a prime denote the moving reference frame (the channel), whereas no prime refers to the stationary frame.

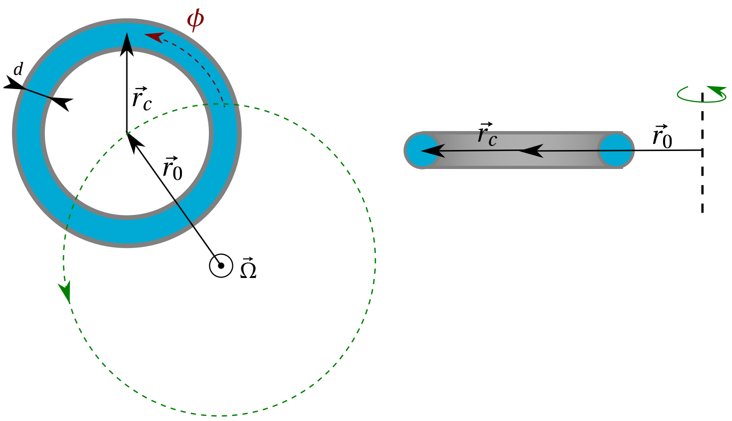

FIGURE 2.2: The center of the torus is located at $\vec{r}_0$ and rotates with an angular velocity $\vec{\Omega}$, which is pointing out of the sheet.

To investigate what terms contribute to the induced fluid movement inside the channel, we will consider each of the four terms in Equation 2.2. Since we are interested in the net contribution of each term, we will integrate over the axial direction of the channel.

From Stokes' Theorem, we know that the first term integrated over the channel length yields zero:

$$\oint_0^{2\pi} \vec{a} \cdot R_c d\vec{\phi} = \iint_A (\nabla \times \vec{a}) \cdot R_c d\vec{A} = 0 \tag{2.3}$$

Since the curl of $\vec{a}$ is equal to zero. This result means that the sensor is insensitive to linear acceleration, as expected from the fully circular symmetry. $\vec{v}'$ in the second term is constraint, because of the incompressibility of water. So the only contribution that could yield a nonzero result when integrated over the torus volume, is the $\vec{\phi}$-direction. Because the integrand is perpendicular $d\vec{\phi}$ the integral yields zero:

$$\oint_0^{2\pi} (-2\vec{\Omega} \times \vec{v}') \cdot R_c d\vec{\phi} = 0 \tag{2.4}$$

Hence the dot product yields zero. Because all operators in Equation 2.2 are linear, we can split the integral of the third term in two parts:

$$\oint_0^{2\pi} \vec{\Omega} \times (\vec{\Omega} \times (\vec{r}_0 + \vec{r}_1)) \cdot R_c d\vec{\phi} = \oint_0^{2\pi} \vec{\Omega} \times (\vec{\Omega} \times \vec{r}_0) \cdot R_c d\vec{\phi} + \oint_0^{2\pi} \vec{\Omega} \times (\vec{\Omega} \times \vec{r}_1) \cdot R_c d\vec{\phi} = 0 \tag{2.5}$$

Since $\vec{r}_0$ is constant, the first term of the right hand side equals zero. The second term is zero because $\vec{\Omega} \times (\vec{\Omega} \times \vec{r}_1) \perp \mathrm{d}\vec{\phi}$ and hence the dot product yields zero. What remains is the fourth term. Using the same reasoning of linear operators, we find:

$$\oint_0^{2\pi} \left(\frac{\mathrm{d}\vec{\Omega}}{\mathrm{d}t} \times (\vec{r}_0 + \vec{r}_1) \right) \cdot R_c \mathrm{d}\vec{\phi} = \oint_0^{2\pi} \left(\frac{\mathrm{d}\vec{\Omega}}{\mathrm{d}t} \times \vec{r}_0 \right) \cdot R_c \mathrm{d}\vec{\phi} + \oint_0^{2\pi} \left(\frac{\mathrm{d}\vec{\Omega}}{\mathrm{d}t} \times \vec{r}_1 \right) \cdot R_c \mathrm{d}\vec{\phi} \tag{2.6}$$

Since $\vec{r}_0$ is constant, the first term of the right hand side is zero. The second term is, however, nonzero:

$$\oint_0^{2\pi} \left(\frac{\mathrm{d}\vec{\Omega}}{\mathrm{d}t} \times \vec{r}_1 \right) \cdot R_c \mathrm{d}\vec{\phi} = 2\pi R_c^2 \frac{\mathrm{d}\Omega}{\mathrm{d}t} \tag{2.7}$$

Hence Equation 2.2 reduces to a single nonzero term, which denotes the acceleration in the moving reference frame integrated over the axial direction of the channel. To find the corresponding body force f we find:

$$f = \rho \frac{2\pi R_c^2 \frac{\mathrm{d}\Omega}{\mathrm{d}t} A}{2\pi R_c A} \tag{2.8}$$

In which A is the cross sectional area of the channel. Hence we find that the body force that is induced by the applied angular acceleration reads

$$\boxed{f = \rho R_c \alpha} \tag{2.9}$$

In which $\alpha = \frac{\mathrm{d}\Omega}{\mathrm{d}t}$ is the applied angular acceleration. Note that this result only depends on the system radius R_c and *not* on the center of rotation [2]. From now on we will consider a coordinate system with respect to the channel.

If we assume the diameter of the channel to be small compared to the system radius ($d \ll R_c$), we can consider the channel to be an infinitely long cylinder and use cylindrical coordinates.

[2] Performing this analysis complicates the problem a lot. The problem statement is given in Appendix A

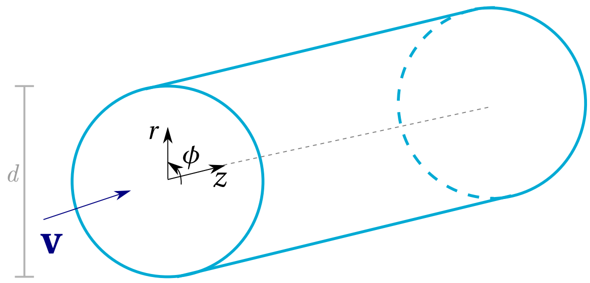

FIGURE 2.3: When the assumption that $d \ll R_c$ is made, the fluid dynamics can be described for an infinitely long cylinder and cylindrical coordinates can be used. The channel is indicated in cyan.

The body force then points in the axial direction (z). Since the sensor is rotated harmonically, the body force varies also harmonically in time:

$$\vec{f} = \rho R_c \alpha \exp(j\omega t)\hat{e}_z \tag{2.10}$$

Note that if the sensor is rotated harmonically with angle $\phi(t) = \phi_0 \exp(j\omega t)$, the magnitude of α reads:

$$\alpha = \left|\frac{\mathrm{d}^2\phi(t)}{\mathrm{d}t^2}\right| \tag{2.11}$$

$$= -\omega^2\phi_0 \tag{2.12}$$

Because of the cylindrical; symmetry in the sensor we assume that there is only a flow in the axial (z) direction and use the Navier-Stokes equations in cylindrical coordinates. This symmetry also allows us to assume no pressure gradients in the channel ($\nabla p = 0$). Equation 2.1 then reduces to:

$$\boxed{\mu\left[\frac{\partial^2 v}{\partial r^2} + \frac{1}{r}\frac{\partial v}{\partial r}\right] + \rho R_c \alpha \exp(j\omega t) = \rho\frac{\partial v}{\partial t}} \tag{2.13}$$

Here $r = 0$ is at the center of the *channel* and $r = R$ at the channel wall. This expression is valid for an incompressible Newtonian fluid with a Reynold's number in the fully laminar flow regime [1], that is:

$$\mathrm{Re} = \frac{\rho d v}{\mu} < 200 \tag{2.14}$$

In which d is a typical length scale, such as the channel's diameter. Because of the small dimensions, this condition is met in most microfluidic systems.

2.1 Oscillating flow profile

Equation 2.13 is an inhomogeneous partial differential equation which can be solved by imposing the no slip boundary condition: the flow at the wall of the channel should equal zero ($v(R,t)=0$). Note that R denotes the radius of the *channel*, whereas R_c denotes the *system* radius, i.e. the radius of the torus. As described by Schlichting [11], the solutions reads:

$$v(r,t) = -\frac{R_c\alpha}{\omega}\left[1-\frac{J_0\left(r\sqrt{\frac{\omega}{2\nu}}(1-j)\right)}{J_0\left(R\sqrt{\frac{\omega}{2\nu}}(1-j)\right)}\right]\exp(j\omega t) \tag{2.15}$$

In which $\nu=\mu/\rho$ is the kinematic viscosity and J_0 the zeroth order Bessel function.

If we take the limit for ω to zero, the flow profile can be seen as a quasi static solution. That is, Equation 2.13 can be solved by taking the time derivative term to be zero and imposing $v(r,t)=v(r)\exp(j\omega t)$. This will yield a simple differential equation with the following solution.

$$v(r,t) = \frac{R_c\alpha}{4\nu}\left(R^2-r^2\right)\exp(j\omega t) \tag{2.16}$$

Note that both Equation 2.15 and Equation 2.16 oscillate harmonically in time and are proportional to the applied acceleration α. The quasi static solution is in phase with the applied body force. The solution in Equation 2.15 has, however, a phase lag with respect to the body force applied.

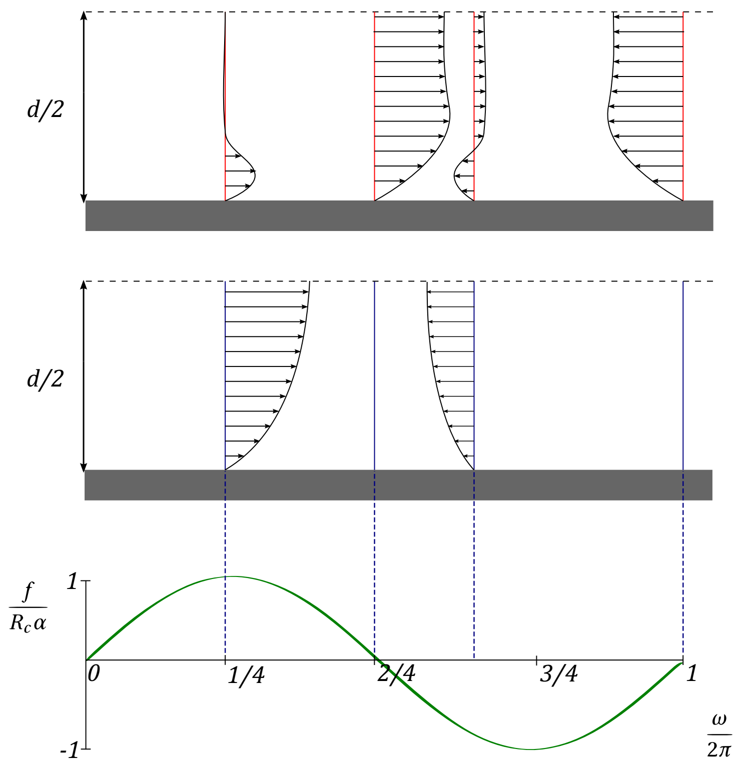

FIGURE 2.4: Illustration of the two different flow profile solutions. Top: full solution, middle: quasi static solution, bottom: applied body force. The figure is not to scale: for the same body force the average flow velocity is higher for the quasi static solution than for the full one.

The quasi static solution is valid when the *boundary layer* thickness is sufficiently large, i.e. larger than the channel radius. The boundary layer is a fluid layer close to a surface where the effects of viscosity are significant. In pipe flow this means the region where the profile is parabolic. The smaller the boundary layer, the more the quasistatic solution (2.16) converges to the full one (2.15). It can be observed from the latter that the boundary thickness δ can be described as:

$$\delta = \sqrt{\frac{2\nu}{\omega}} \tag{2.17}$$

It is desirable to work within the quasi static solution region since the flow profile can then be described in a relatively simple expression, it is in phase with the body force applied and it does not have modes in which the fluid is not flowing in the same direction over the entire channel diameter. Furthermore, for the same angular acceleration, the quasi static solution will yield a higher average flow velocity than the full one. To work within this regime, δ should exceed the dimension of the channel:

$$\delta > d/2 \tag{2.18}$$

Hence the angular frequency should not exceed a certain value to stay within the quasi static regime.

If we rewrite this to frequency f we obtain the following condition:

$$f < \frac{4\nu}{\pi d^2} \tag{2.19}$$

2.2 Fluidic connections

The sensors have to be filled and are therefore (fluidically) connected to the outside world. These connections can have a significant influence on the flow profile and therefore on the output signal. There are three basic elements we need to consider.

First, the sensor and connecting tubing do not always have the same diameter. Therefore, they have a different fluidic resistance R_H. Analogous to the derivation in the previous section we find for a pressure driven flow:

$$\Delta P = \frac{8\mu L\phi}{\pi r^4} \tag{2.20}$$

In which ϕ is the volumetric flow velocity (m^3 s^{-1}). Next, if we define R_H as the pressure over volumetric flow velocity fraction, we find:

$$R_H = \frac{8\mu}{\pi r^4} L \tag{2.21}$$

This is analogous to Ohm's law in the electrical domain. We can extend this analogy to a fluidic capacitance and inductance.

The tubing does not have an infinite stiffness, so it is able to stretch. This gives rise to a capacitor-like behavior. Analogous to the electrical domain, we define the fluidic capacitance C_H:

$$\phi = C_H \frac{\mathrm{d}\Delta P}{\mathrm{d}t} \tag{2.22}$$

In order to find an expression for C_H we need to know the deformation of the channel as a function of the applied pressure. Let k be the stiffness of the channel, which we define as:

$$\begin{aligned} k &= \frac{\partial V}{\partial p} && (2.23)\\ &= \frac{\partial V}{\partial r}\frac{\partial r}{\partial p} && (2.24)\\ &= 2\pi r L \frac{\partial r}{\partial p} && (2.25) \end{aligned}$$

The evaluation of the $\partial r/\partial p$ term is rather tedious. A very careful analysis of the stress and strain relations has to be performed. For a uniform pressure applied to a thin walled cylinder with inner diameter R_1 and outer diameter R_2 the result reads [12]:

$$\frac{\partial r}{\partial p} = \frac{1+\nu}{\left(\frac{R_2^2}{R_1^2}-1\right)E}\left(\frac{R_2^2}{r}+\frac{1-\nu}{1+\nu}r\right) \tag{2.26}$$

In which E is young's modulus and ν the Poisson ratio. The volumetric flow velocity ϕ is defined as the change in volume per unit time. Combining this definition with Equation 2.22 and Equation 2.23 we find:

$$\phi = \frac{\partial V}{\partial t} \tag{2.27}$$

$$= \frac{\partial k\Delta P}{\partial t} \rightarrow C_H = k \tag{2.28}$$

Evaluating the $\partial r/\partial p$ in the middle of the channel wall ($r = (R_2 - R_1)/2$) yields the fluidic capacitance C_H:

$$C_H = \frac{2\pi(1+\nu)}{\left(\frac{R_2^2}{R_1^2}-1\right)E}\left(R_2^2+\frac{1-\nu}{1+\nu}\left(\frac{R_2-R_1}{2}\right)^2\right)L \tag{2.29}$$

In a similar fashion we can define a fluidic inductance, which is caused by the inertia of the fluid inside the channel. Because of this nonzero inertia a step in the driving pressure will not *immediately* cause a step in the volumetric flow. It needs some time to reach this value. Hence we define the fluidic inductance L_H as:

$$\Delta P = L_H\frac{\mathrm{d}\phi}{\mathrm{d}t} \tag{2.30}$$

To find an expression for L_H we should write the differential equation in the fluidic domain rather than the electrical one. That is, instead of Kirchhoff, we use Newton and obtain [13]:

$$L_H = \frac{\rho L}{A} \tag{2.31}$$

In which A is the cross section of the tubing and L its length. Note that R_H, C_H and L_H all scale linearly with the length of the channel. These definitions are very useful, since we can use our knowledge of electrical networks to solve the fluidic one.

Let's assume we have flow source that makes a step at $t = 0$. So we have:

$$\phi_{\text{driving}}(t) = \begin{cases} 0 & \text{if } t \leq 0 \\ \phi_0 & \text{if } t > 0 \end{cases} \tag{2.32}$$

This flow source is connected via tubing to the sensor. The electrical analogue is shown in Figure 2.5.

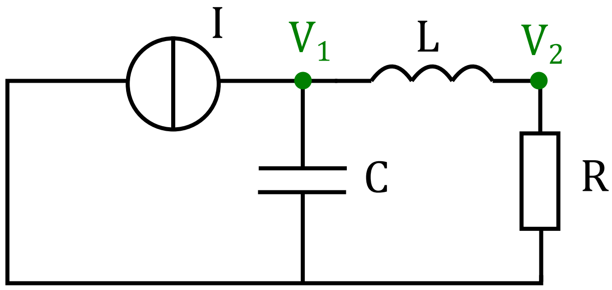

FIGURE 2.5: Electrical analogue for a sensor actuated by a flow source.

Since we are using a *flow* source the elctrical equivalent is a current source. We assume the diameter of the channel in the sensor is much smaller than the one in the tubing and therefore all resistance in the network comes from the sensor. The opposite is true for the capacitance; the sensor is assumed to be infinitely stiff and therefore the capacitance is caused by the deformation of the tubing. Since the tubing can expand with respect to the ambient pressure it is in parallel with R and L.

In order to solve this network we use complex impedances and apply Kirchhoff's current law and obtain two equations:

$$-I + \frac{V_1}{Z_C} + \frac{V_1 - V_2}{Z_L} = 0 \tag{2.33}$$

$$\frac{V_1 - V_2}{Z_L} = \frac{V_2}{R} \tag{2.34}$$

Combining these two equations yields:

$$\frac{V_2}{I} = \frac{Z_R Z_C}{Z_C + Z_L + Z_R} \tag{2.35}$$

$$= \frac{R \cdot 1/j\omega C}{1/j\omega C + j\omega L + R} \tag{2.36}$$

$$= \frac{R}{1 - \omega^2 LC + j\omega RC} \tag{2.37}$$

Hence we obtain the original differential equation for V_2:

$$LC\frac{\mathrm{d}^2 V_2}{\mathrm{d}t^2} + RC\frac{\mathrm{d}V_2}{\mathrm{d}t} + V_2 = IR \tag{2.38}$$

With the corresponding initial conditions:

$$V_2(0) = 0 \tag{2.39}$$

$$\left.\frac{\mathrm{d}V_2}{\mathrm{d}t}\right|_{t=0} = 0 \tag{2.40}$$

Which leads to a solution for the current through the resistor:

$$\boxed{i_R = \frac{V_2}{R} = I\left[1 - \frac{RC+\gamma}{\gamma}\exp\left(-\left(\frac{RC-\gamma}{2LC}\right)t\right) + \frac{RC-\gamma}{\gamma}\exp\left(-\left(\frac{RC+\gamma}{2LC}\right)t\right)\right]} \tag{2.41}$$

In which $\gamma = \sqrt{C^2R^2 - 4LC}$. Translating this back to the fluidic domain, i_R translates to the volumetric flow through the sensor. This flow clearly does not instantaneously follow ϕ from the flow source. It can, depending on the values of R, C and L, show damped oscillations.

Chapter 3

Thermal readout

This chapter deals with the development of a micromachined sensor that uses thermal readout to measure the flow velocity in the channel and hence the applied angular acceleration. It exploits the linear relation[1] between temperature and resistance of a resistor [14, 15]:

$$R(T) = R_0[1 + \alpha_R(T - T_0)] \tag{3.1}$$

$$\Delta T = T - T_0 = \frac{\Delta R}{\alpha_R R_0} \tag{3.2}$$

In which R is the resistance, T the temperature and T_0 a reference temperature. Note that α_R denotes the temperature coefficient of resistance and *not* the angular acceleration.

The sensor consists of a fully circular channel made of siliconrich nitride (SiRN) with a diameter of 40 μm. Parts of the channel are buried in silicon and parts hang freely. On the freely hanging parts gold electrodes are placed to be used in the thermal readout. For a detailed explanation about the fabrication process, refer to subsection 5.1.1.

Figure 3.1 provides a two and three dimensional representation of the sensor.

[1] For small temperature differences

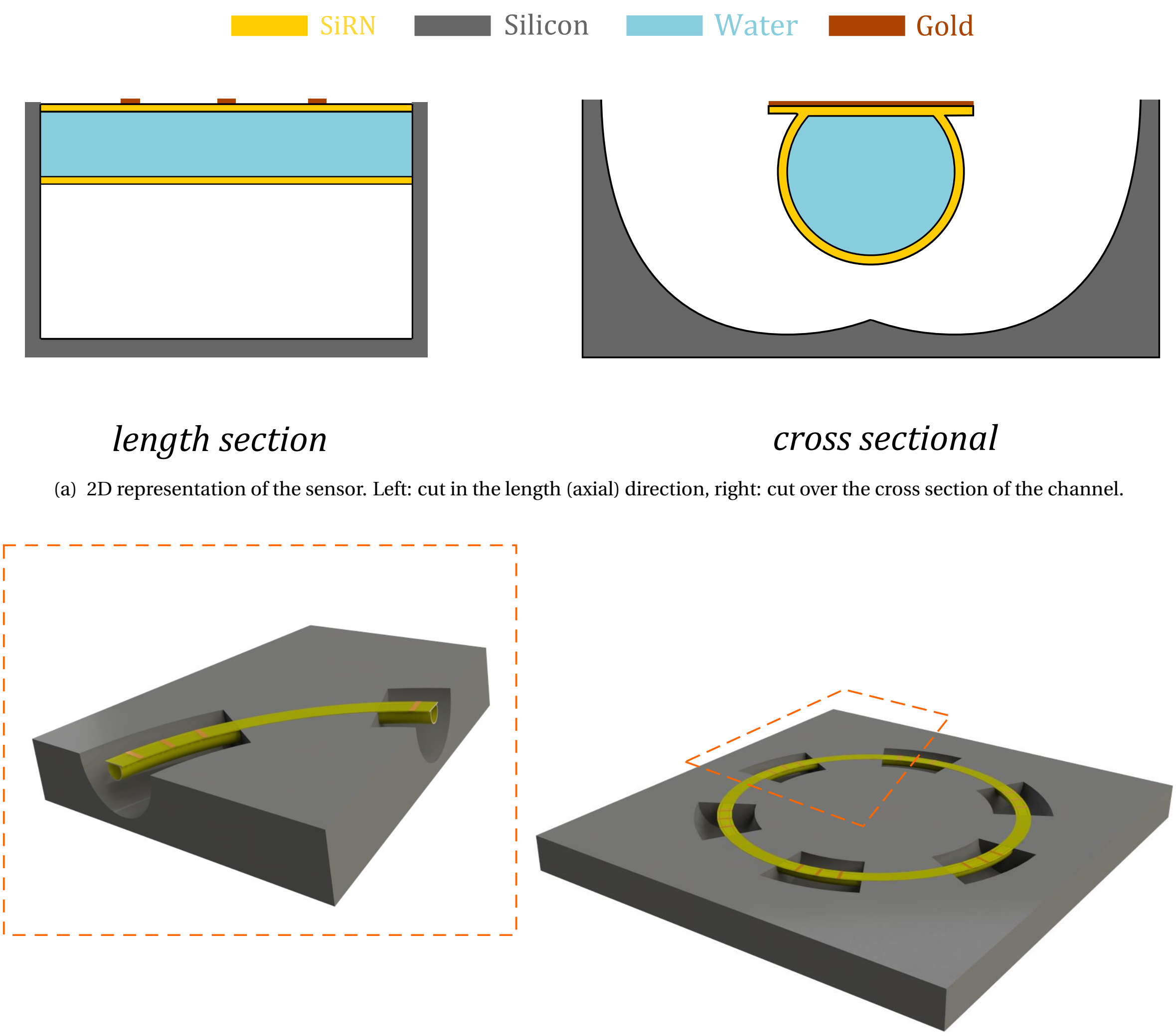

(a) 2D representation of the sensor. Left: cut in the length (axial) direction, right: cut over the cross section of the channel.

(b) 3D impression of the sensor. The channel (indicated in yellow) is partly released from the silicon and partly buried in silicon. The gold electrodes (indicated in brown) are connected to the outside world.

FIGURE 3.1: Two and three dimensional illustration of the sensor. Parts of the channel are insulated from the silicon, parts are in (thermal) contact with it.

3.1 Theory and modeling

A variety of physical phenomena is involved in describing the physics of the device. The basic equation governing the thermodynamics of the readout mechanics is the heat equation:

$$\rho c_p \left[\frac{\partial T}{\partial t} + (\vec{v} \cdot \nabla) T \right] = k \nabla^2 T + Q \tag{3.3}$$

In which ρ is the fluid's density, c_p its heat capacity at constant pressure, T the temperature, v the fluid flow velocity, k the thermal conductivity and Q a heat source (density). Because of the complex channel geometry it is not possible to solve the heat equation analytically in three dimensions. It is therefore of paramount importance to develop an accurate model that is able to describe the sensor's performance accurately while also being simple enough to provide insight.

Several models describing thermal readout systems similar to the one discussed in this thesis have been developed. Van Honschoten and Svetovoy (refer to e.g. [16–18]) constructed a model that describes the behavior of a two wire thermal sensor very accurately. It describes the temperature change of the wire as a function of the applied velocity field for both constant and alternating fluid flow. Lammerink et al. [19] have constructed a much simpler model. The temperature profile is described with only one (one dimensional) differential equation. This model is also very useful, but lacks an analysis of the system's characteristics when subjected to oscillatory flow.

Both models are in principle very helpful. However, the sensor geometry used in developing these models is rather different from the one in this thesis.

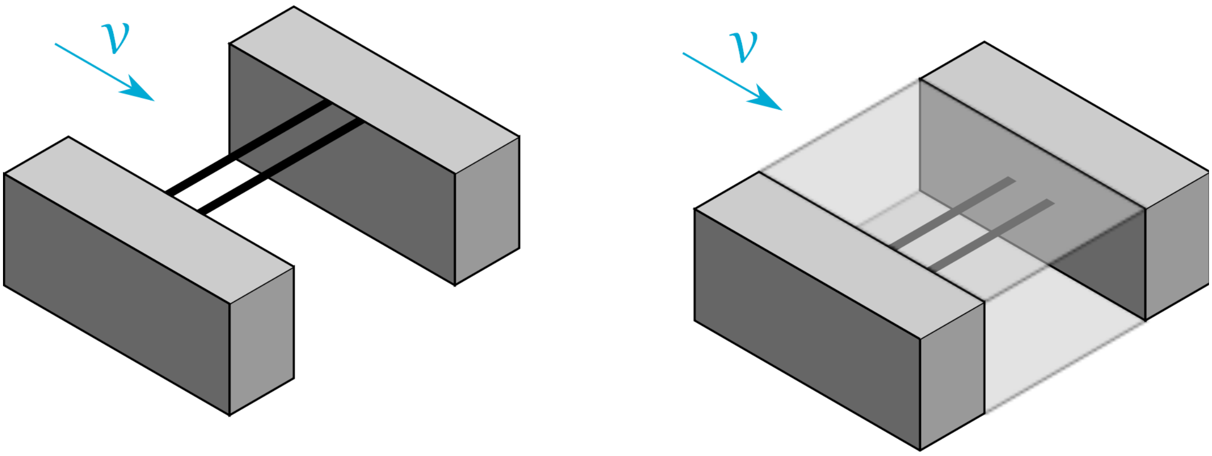

FIGURE 3.2: Left: van Honschoten et al. [16], right: Lammerink et al. [19]. In the left model two very long wires (with respect to its hight and width) are considered. The walls in the vertical direction are assumed to be at infinite height. The right model also considers two long wires, but now they are within a confined channel. The temperature of the top and bottom wall is set to a fixed reference temperature. In both models a uniform flow velocity v is applied.

Applying one of these models to the sensor described in this report gives rise to a couple of complications since a lot of assumptions made in developing the models are not met in the sensor in this thesis. First, the heaters are not very long in one dimension with respect to the other two. So it will not be trivial to describe the system's physics in a one or two dimensional model. Second, the heater are not placed directly in the fluid flow. The heat has to flow through the nitride channel wall into the fluid. Because silicon nitride is a good conductor there will also be heat conduction in the flow direction through the nitride. Third, the walls of the channel do not have a fixed temperature. The silicon underneath it does, but above the channel there is no fixed temperature. We only know that far away from the sensor the temperature is equal to the ambient temperature. And last, the applied velocity is not uniform, especially for high frequencies in which the steady state flow velocity approximation is not valid anymore.

All the complicating factors mentioned make it hard to apply the models to the sensor. It is therefore favorable to view the problem from a different angle. In the models of Van Honschoten and Svetovoy and Lammerink and Tas the heat sinks are in the direction perpendicular to the flow. That is not entirely true for the sensor in this thesis. Since only parts of the channel are released, some parts of the channel are also in direct contact with the silicon. Since silicon is also very good conductor and has a high heat capacity it is a valid assumption to take the silicon as a heat sink at a fixed temperature. This can simplify the problem a lot, as the heat flow and heat sink are in the same direction, the x-direction (parallel to the fluid flow). This is illustrated graphically in figure 3.3.

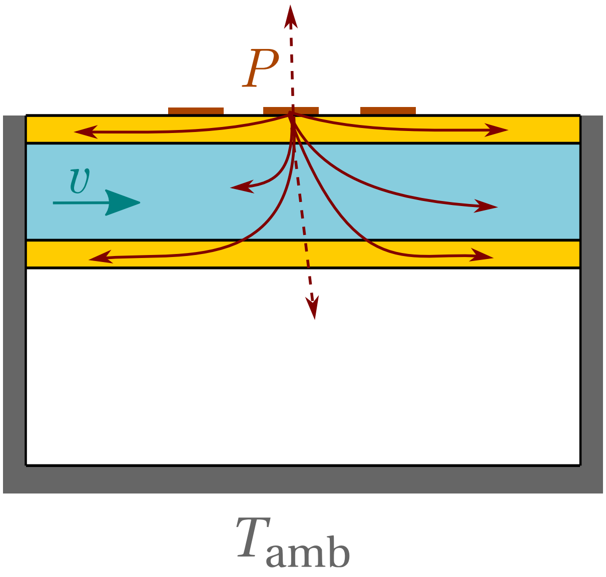

FIGURE 3.3: Illustration of the heat sink in the x-direction. The power P in the heater generates a heat flow (depicted by the red arrows). Parts of the heat will flow to the air above and the air and silicon under the channels. These contributions are, however, assumed to be small compared to the heat flow in the direction of the flow since the thermal conductivities of silicon nitride and water are much higher than that of air.

The thermal conductivity of silicon nitride and water is much higher than that of air so the heat transfer in the radial direction through air is neglected.

3.1.1 Analytical model

We will only consider the heat transfer in the direction of flow, the x-direction, so we can construct a one dimensional model. We start from the full, three dimensional heat equation:

$$\rho c_p \left[\frac{\partial T}{\partial t} + (\vec{v} \cdot \nabla) T \right] = k \nabla^2 T + Q \tag{3.4}$$

We will first try to find a steady state temperature profile without any flow applied to the sensor. Hence the $\partial T / \partial t$ and $\vec{v}$ terms are zero. There is no additional heat source, except at the heater itself. Hence the heat equation reduces to:

$$-k \frac{\mathrm{d}^2 T}{\mathrm{d}x^2} = \begin{cases} Q, & \text{if } |x| \leq x_h \\ 0, & \text{otherwise} \end{cases} \tag{3.5}$$

In which the heater is located in between $-x_h$ and x_h.

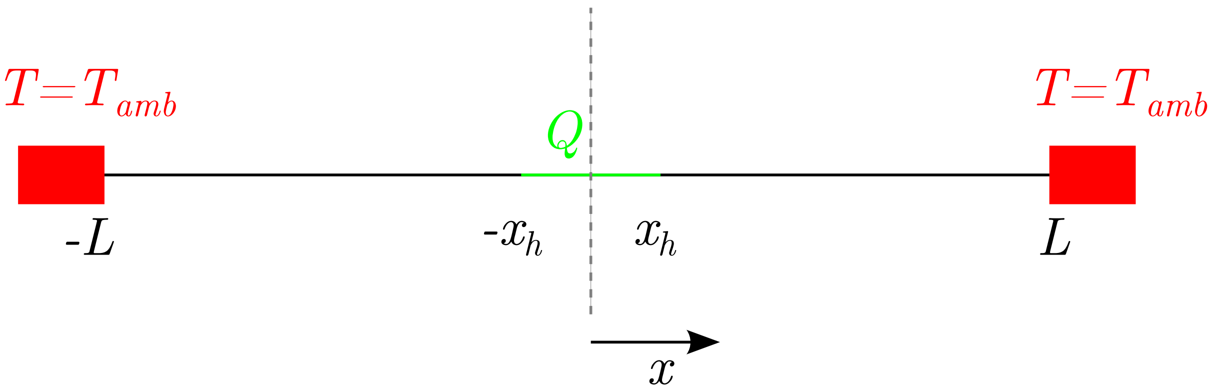

FIGURE 3.4: Sketch of the one dimensional model. At $x = \pm L$ the silicon acts as a heat sink at fixed temperature, T_{amb}. In between $\pm x_h$ the heater dissipates Q watts per cubic meter.

To obtain a proper value for the thermal conductivity in the one dimensional equation, we take a weighted average k_{eff} between silicon nitride and water:

$$k = k_{\text{eff}} = \frac{k_{\text{SiRN}} A_{\text{SiRN}} + k_{\text{water}} A_{\text{water}}}{A_{\text{total}}} \tag{3.6}$$

In which A is the cross sectional area. Note that the unit of k_{eff} is the same as the unit of k_{SiRN} and k_{water} ($\mathrm{W\,m^{-1}\,K^{-1}}$) We should also define a 'weighted' heat source. If we would just plug Q in Equation 3.5 we would obtain a temperature profile as if were heating over the *entire* channel cross section. Therefore we define:

$$Q = Q_{\text{total}} \frac{A_{\text{heater}}}{A_{\text{channel}}} \tag{3.7}$$

In which Q_{total} is the total heat source density applied to the sensor, A_{heater} the cross sectional area of the heater and A_{channel} the cross sectional area of the channel. Note that Q is the heat source *density* ($\mathrm{W\,m^{-3}}$).

Equation 3.5 is a linear, second order differential equation which is only nonhomogeneous for $|x| \leq x_h$. The solution is readily found:

$$T(x) = \begin{cases} A_1 x + B_1, & \text{if } -L \leq x \leq -x_h \\ -\frac{Q}{2k}x^2 + Cx + D, & \text{if } |x| \leq x_h \\ A_2 x + B_2, & \text{if } x_h \leq x \leq L \end{cases} \tag{3.8}$$

In order two find the values of the constants (six in total), we need to impose six boundary conditions. The first two are found by setting the temperature at the silicon to ambient temperature:

$$T(-L) = T(L) = T_{\text{amb}} \tag{3.9}$$

The other four boundary conditions are found at the edges of the heater. First, the temperature should be continuous at $\pm x_h$. Hence the solution for $x \le x_h$ should yield the same temperature as the solution for $|x| \le x_h$.

$$T_{\text{left}}(-x_h) = T_{\text{heater}}(-x_h) \quad \text{and} \quad T_{\text{heater}}(x_h) = T_{\text{right}}(+x_h) \tag{3.10}$$

The same should hold for the heat fluxes at $x = \pm x_h$:

$$k\left.\frac{\mathrm{d}T_{\text{left}}}{\mathrm{d}x}\right|_{x=-x_h} = k\left.\frac{\mathrm{d}T_{\text{heater}}}{\mathrm{d}x}\right|_{x=-x_h} \quad \text{and} \quad k\left.\frac{\mathrm{d}T_{\text{heater}}}{\mathrm{d}x}\right|_{x=+x_h} = k\left.\frac{\mathrm{d}T_{\text{right}}}{\mathrm{d}x}\right|_{x=+x_h} \tag{3.11}$$

Solving these six equations yields the values for A_1, A_2, B_1, B_2, C and D [2]:

$$\boxed{T(x) = \begin{cases} \frac{Q}{k}x_h(L+x) + T_{\text{amb}}, & \text{if } -L \le x \le -x_h \\ -\frac{Q}{2k}x^2 + \frac{Q}{k}x_h\left(L - \frac{x_h}{2}\right) + T_{\text{amb}}, & \text{if } |x| \le x_h \\ \frac{Q}{k}x_h(L-x) + T_{\text{amb}}, & \text{if } x_h \le x \le L \end{cases}} \tag{3.12}$$

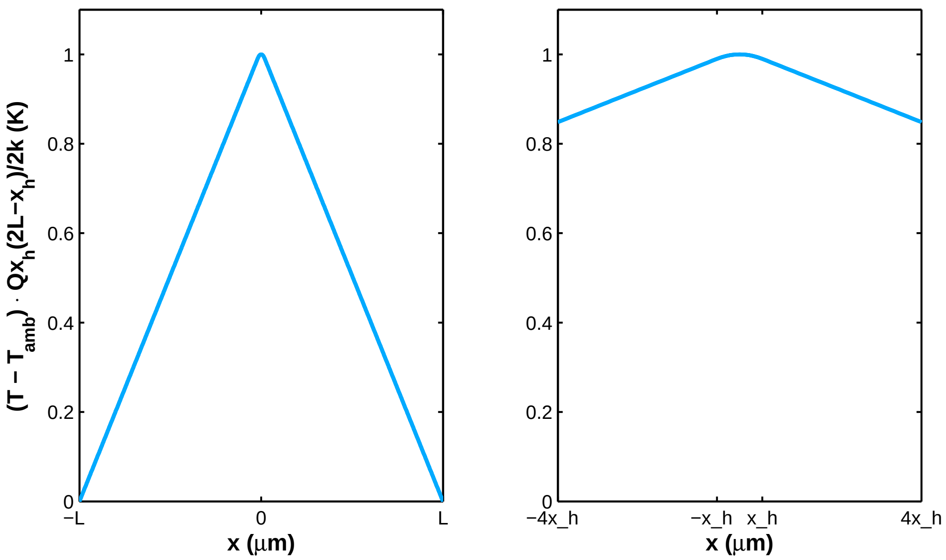

FIGURE 3.5: Equation 3.12 normalized to 1 at $x = 0$. Left: $(T - T_{\text{amb}})\frac{Qx_h(2L-x_h)}{2k}$ for the full x-axis. Outside the heater the temperature decreases linearly. Right: close up of the heater. For $|x| \le x_h$ the temperature is quadratic with x.

[2] Here, we neglect the difference in thermal conductivity between a part of the channel with and without electrodes.

Constant flow

If we include the (constant) flow, the differential equation becomes a little more complicated, but the procedure remains the same. The heat equation becomes:

$$-k\frac{\mathrm{d}^2 T}{\mathrm{d}x^2} + \rho c_p v \frac{\mathrm{d}T}{\mathrm{d}x} = \begin{cases} Q, & \text{if } |x| \leq x_h \\ 0, & \text{otherwise} \end{cases} \tag{3.13}$$

Which has the solution:

$$T(x,v) = \begin{cases} A_1 \exp(\rho c_p x/k) + B_1, & \text{if } -L \leq x \leq -x_h \\ \frac{1}{\rho c_p v}\left[A_c k \exp(\rho c_p x/k) + Qx\right] + B_c, & \text{if } |x| \leq x_h \\ A_2 \exp(\rho c_p x/k) + B_2, & \text{if } x_h \leq x \leq L \end{cases} \tag{3.14}$$

The values for the constants can be found by imposing the same boundary conditions as in the previous case. The values of these constants can be found in Appendix B. If we take the limit of v to zero, we find the same expression as in Equation 3.12.

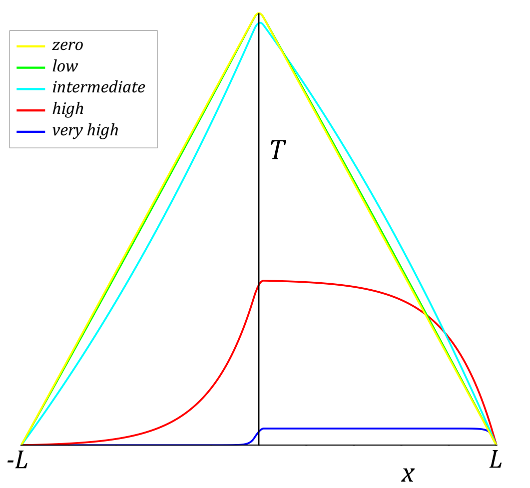

(a) Temperature profile for zero (yellow) to very high flow velocities (blue).

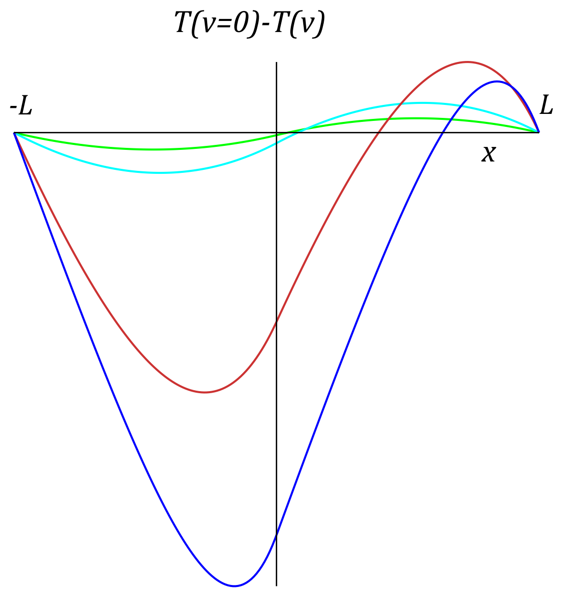

(b) The change in temperature when a flow is applied.

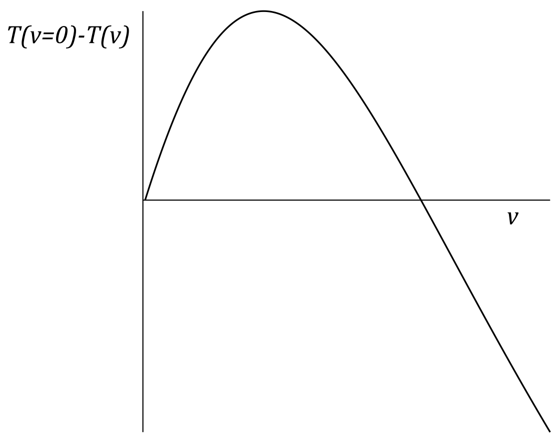

(c) The change in temperature as a function of velocity at $x = +L/2$.

FIGURE 3.6: The temperature profile for an applied flow. For small velocities, the change is temperature is symmetrical and linear with v. When the velocity becomes too high, the whole sensor is cooling down and the linear relation between temperature and velocity is not valid anymore.

Equation 3.14 is an expression in closed form, but because of the long constants it is rather hard analyze it. Furthermore, it does not have a full linear relation with v. This is only the case for small values of v. To gain more insight in we perform a Taylor expansion around a certain small velocity v_i[3]. Next, we take the limit for v_i to zero. We are interested in the regions outside of the center heater, so let's have look at the region downstream of it. A first order approximation then yields:

$$\boxed{T(x,v) = \frac{Qx_h}{k}\left[\frac{\rho c_p}{6k}\left(-3x^2 + \left(3L + \frac{x_h^2}{L}\right)x - x_h^2\right)v + (L-x)\right] \quad \text{for } x_h \leq x \leq L} \tag{3.15}$$

Which is a much more compact expression that provides insight. In addition, we are only interested

[3]Because of the $1/v$ therm we cannot directly perform at Taylor series around $v = 0$.

in the region of the sensor where it the temperature is linear with the applied flow. Hence we can use this expression in analyzing the temperature profile for a constant flow.

Alternating flow

The flow in the channel is, however, not necessarily constant in time. It can vary approximately harmonically in time: $v = v_0 \exp(j\omega t)$. The heat equation therefore becomes:

$$\rho c_p \left[\frac{\partial T(x,t)}{\partial t} + v_0 e^{j\omega t} \frac{\partial T(x,t)}{\partial x} \right] - k \frac{\partial^2 T(x,t)}{\partial x^2} = Q(x) \tag{3.16}$$

This a partial differential equation with time dependent constants. In general, this is not solvable in a closed form. Let us examine the two processes: heat conduction and convection. From a dimensional analysis we learn that the time needed for a particle to travel from a heater (at $x = 0$) to a sensor (at $x = L$) by conduction reads:

$$t_{\text{cond}} = \frac{\rho c_p L^2}{k} \tag{3.17}$$

The time needed for the same heat transfer by convection reads:

$$t_{\text{conv}} = \frac{L}{v} \tag{3.18}$$

If we assume that the difference in temperature profile due to convection is small we can solve the problem by seeing the temperature change as a perturbation, i.e. adding a small temperature δT to the temperature and solve the heat equation [16]. This assumption is valid when $t_{\text{cond}} \ll t_{\text{conv}}$, i.e.

$$v \ll \frac{k}{\rho c_p L} \tag{3.19}$$

We assume that the applied velocity is harmonic in time ($v = v_0 \exp(i\omega t)$), so the small temperature addition is also harmonic, i.e.

$$\delta T(x,t) = \delta T_0(x) \exp(j\omega t) \tag{3.20}$$

Hence we can write the total temperature $T_{\text{tot}}(x,t)$ as:

$$T_{\text{tot}}(x) = T(x) + \delta T_0(x) \exp(j\omega t) \tag{3.21}$$

Inserting this expression in Equation 3.16 yields:

$$\rho c_p \left[\frac{\partial (T(x) + \delta T_0(x)\exp(j\omega t))}{\partial t} + v_0 \exp(j\omega t) \frac{\partial (T(x) + \delta T_0(x)\exp(j\omega t))}{\partial x} \right] - k \frac{\partial^2 (T(x) + \delta T_0(x)\exp(j\omega t))}{\partial x^2} = Q(x) \tag{3.22}$$

Linearity of the heat equation allows us the split this into two equations:

$$\underbrace{\rho c_p \frac{\partial T(x)}{\partial t}}_{=0} - k \frac{\partial^2 T(x)}{\partial x^2} = Q(x) \tag{3.23}$$

$$\rho c_p \left[\frac{\partial \delta T_0(x)\exp(j\omega t)}{\partial t} + v_0 \exp(j\omega t) \frac{\partial (T(x) + \delta T_0(x)\exp(j\omega t))}{\partial x} \right] - k \frac{\partial^2 \delta T_0(x)\exp(j\omega t)}{\partial x^2} = 0 \tag{3.24}$$

Since we have already solved 3.23 before we can find the total solution by solving 3.24, which reduces to:

$$\rho c_p j\omega\, \delta T_0(x) \exp(j\omega t) + v_0 \left(\frac{\partial T(x)}{\partial x} + \underbrace{\frac{\partial \delta T_0(x)\exp(j\omega t)}{\partial x}}_{=0} \right) \exp(j\omega t) - k \frac{\partial^2 \delta T_0(x)}{\partial x^2} \exp(j\omega t) = 0 \tag{3.25}$$

$$\rho c_p j\omega\, \delta T_0(x) + v_0 \left(\frac{\partial T(x)}{\partial x} \right) - k \frac{\partial^2 \delta T_0(x)}{\partial x^2} = 0 \tag{3.26}$$

In which the $\partial T(x)/\partial x$ can be found by solving Equation 3.23, i.e. the solution in Equation 3.12[4]. The $\partial \delta T_0(x)\exp(j\omega t)/\partial x$ term is small compared to the $\partial T(x)/\partial x$ term and we therefore neglect it. Hence we obtain:

$$j\omega\, \delta T_0(x) - \frac{k}{\rho c_p} \frac{\partial^2 \delta T_0(x)}{\partial x^2} = \begin{cases} -v_0 \frac{Q}{k} x_h, & \text{if } -L \le x \le -x_h \\ +v_0 \frac{Q}{k} x, & \text{if } |x| \le x_h \\ +v_0 \frac{Q}{k} x_h, & \text{if } x_h \le x \le L \end{cases} \tag{3.27}$$

Unlike Equation 3.16, this is a system of three second order *ordinary*, inhomogeneous, differential equations, which we can solve.

Since we have *three* second order equations we need three sets of two boundary conditions. As a constant ambient temperature at the silicon at $x = \pm L$ is assumed there is no change in temperature there, hence:

$$\delta T_0(-L) = \delta T_0(L) = 0 \tag{3.28}$$

Analogous to the previous derivations the temperature and heat flux should be equal at the edge of

[4]Note that $Q(x)$ is a piecewise defined function, so is $\partial T(x)/\partial x$.

the heater:

$$\delta T_{0,\text{left}}(-x_h) = \delta T_{0,\text{heater}}(-x_h) \quad \text{and} \quad \delta T_{0,\text{heater}}(x_h) = \delta T_{0,\text{right}}(+x_h) \tag{3.29}$$

$$k\,\frac{\mathrm{d}\delta T_{0,\text{left}}}{\mathrm{d}x}\bigg|_{x=-x_h} = k\,\frac{\mathrm{d}\delta T_{0,\text{heater}}}{\mathrm{d}x}\bigg|_{x=-x_h} \quad \text{and} \quad k\,\frac{\mathrm{d}\delta T_{0,\text{heater}}}{\mathrm{d}x}\bigg|_{x=+x_h} = k\,\frac{\mathrm{d}\delta T_{0,\text{right}}}{\mathrm{d}x}\bigg|_{x=+x_h} \tag{3.30}$$

Careful analysis of Equation 3.27 yields the solution for $\delta T_0(x)$:

$$\delta T_0(x) = A_i \cos\left[\zeta(\omega)(1-j)x\right] - B_i \sin\left[\zeta(\omega)(1-j)x\right] + j\,\frac{v_0 Q x_h}{\omega k}\begin{cases} 1, & \text{if } -L \le x \le -x_h \\ -x/x_h, & \text{if } |x| \le x_h \\ -1, & \text{if } x_h \le x \le L \end{cases} \tag{3.31}$$

In which $\zeta(\omega) = \sqrt{\frac{\rho c_p \omega}{2k}}$ and A_i and B_i with $i = 1,2,3$ are constants (six in total) that can be found by the boundary conditions in Equation 3.28 and Equation 3.30. Note that the argument of the functions in Equation 3.31 are complex. The entire function can be written in the $a + jb$ form:

$$\cos\left[\zeta(1-j)x\right] = \cos(\zeta x)\left(\frac{\exp(\zeta x)+\exp(-\zeta x)}{2}\right) + j\sin(\zeta x)\left(\frac{\exp(\zeta x)-\exp(-\zeta x)}{2}\right) \tag{3.32}$$

$$\sin\left[\zeta(1-j)x\right] = \sin(\zeta x)\left(\frac{\exp(\zeta x)+\exp(-\zeta x)}{2}\right) - j\cos(\zeta x)\left(\frac{\exp(\zeta x)-\exp(-\zeta x)}{2}\right) \tag{3.33}$$

The expressions for A_i and B_i can be found in Appendix B. The most important issue to notice is that all these constants scale linearly with v_0 and Q, hence does $\delta T_0(x)$.

So we have found a closed expression for the change in temperature due to the applied velocity in both space and time:

$$\delta T(x,t) = \delta T_0(x) e^{j\omega t} \tag{3.34}$$

Equation 3.31 and Equation 3.34 are, however, still complex functions, whereas the physical change in temperature is of course real. In principle, we could find the real part of Equation 3.34, so that we know δT as a function of space and time. However, this will be a complex calculation and does not gain a lot of insight since we already know that the time dependence is harmonic. Therefore, it makes more sense to look at the *amplitude* of the function, that is the complex modulus:

$$|\delta T(x,t)| = |\delta T_0(x) e^{j\omega t}| = |\delta T_0(x)| \tag{3.35}$$

Hence we only need to consider the modulus of $\delta T_0(x)$, which is not a function of time.

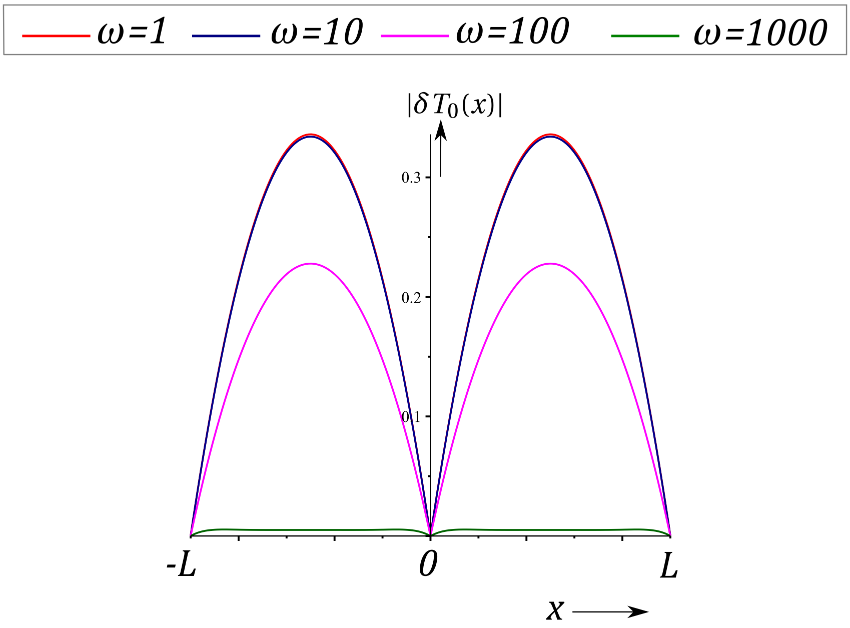

FIGURE 3.7: $|\delta T_0(x)|$ for increasing values of ω. The temperature difference decreases with increasing frequency. The velocity in this plot is taken at 1 mm s^{-1}.

$|\delta T_0(x)|$ is symmetrical around $x = 0$, has it maximum value at $x = \pm L/2$ and decreases for increasing frequencies. So the change in temperature is also a function of the frequency: $|\delta T_0| = |\delta T_0(\omega, x)|$. In the frequency domain the sensor can be seen as a 'black box' with an amplitude transfer function $H(\omega)$. We would like to describe the behavior of the sensor as a function of ω with respect to the signal at $\omega = 0$.

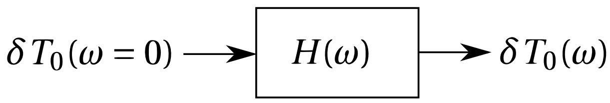

FIGURE 3.8: The definition of the amplitude transfer function $H(\omega)$.

Hence $H(\omega)$ is defined as:

$$H(\omega) = \left| \frac{\delta T_0(\omega)}{\delta T_0(\omega = 0)} \right| \tag{3.36}$$

The amplitude of a first order transfer function is defined as:

$$H(\omega) = \frac{1}{\sqrt{1 + \left(\frac{\omega}{\omega_c}\right)^2}} \tag{3.37}$$

In which ω_c is the corner frequency. Figure 3.9 shows $H(\omega)$ for a channel of 40 μm diameter with a 1 μm silicon nitride wall, filled with water. Therefore, the following parameters have been used:

Feature	Value	Unit
k	2.47	$\mathrm{W\,m^{-1}\,K^{-1}}$
T_{amb}	0	K
ρ	999	$\mathrm{kg\,m^{-3}}$
c_p	4200	$\mathrm{J\,kg^{-1}\,K^{-1}}$
L	250	μm
v	1	$\mathrm{mm\,s^{-1}}$
electrode	$0.2 \times 10 \times 40$	$\mu\mathrm{m}^3$
Q_{total}	$1.25 \cdot 10^{13}$	$\mathrm{W\,m^{-3}}$

The value of Q_{total} denotes a power of 1 mW supplied to a single heater electrode.

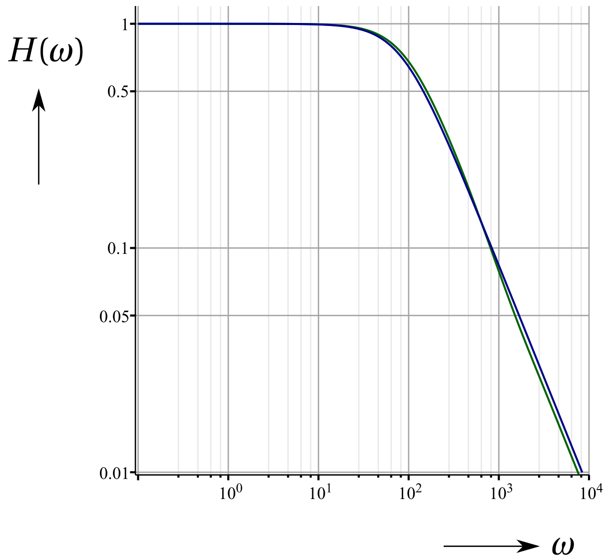

FIGURE 3.9: The transfer function for $|\delta T_0(\omega)/\delta T_0(\omega = 0)|$ (green) and $1/\sqrt{1+(\omega/\omega_c)^2}$ with $\omega_c = 84$ (blue). A strong similarity can be observed.

A very strong similarity between the thermal and first order transfer function can be observed. The corner frequency is equal to $84/2\pi \approx 13$ Hz.

So the signal of the sensor decays with $1/\sqrt{1+(\omega/\omega_c)^2}$. In this analysis, the velocity is taken constant. In reality, when the sensor is angularly accelerated with frequency ω, the velocity will also be a function of ω:

$$v_{\mathrm{avg}} = \frac{\rho R_c R}{6\mu}\alpha \tag{3.38}$$

$$= -\frac{\rho R_c R}{6\mu}\phi_0\omega^2 \tag{3.39}$$

Note that δT_0 scales linearly with v.

3.1.2 Responsivity

The responsivity is a measure for the output of a system per unit input. Hence it is defined as :

$$S = \frac{\partial}{\partial \alpha}\left(\frac{\Delta R}{R}\right)\bigg|_{x=x_s} \tag{3.40}$$

$$= \alpha_R \frac{\partial \Delta T}{\partial \alpha}\bigg|_{x=x_s} \tag{3.41}$$

Where x_s is the position of the sensor element, α_R the temperature coefficient of resistance and α the angular acceleration. Since we are only interested in the region in which ΔT is linear with v we can use the first order approximation. Furthermore, we take the average flow velocity:

$$v_{\text{avg}} = \frac{1}{R}\int_0^R \frac{\rho R_c \alpha}{4\mu}(R^2 - r^2)\,\mathrm{d}r = \frac{\rho R_c R^2}{6\mu}\alpha \tag{3.42}$$

Because of the symmetry of the sensor we only need to determine the responsivity in one region (so either upstream or downstream). We find:

$$\boxed{S(x_s) = \alpha_R \frac{Q x_h \rho^2 c_p R_c R^2}{36\mu k^2}\left(-3x_s^2 + \left(3L + \frac{x_h^2}{L}\right)x_s - x_h^2\right)} \tag{3.43}$$

There are a lot of terms in this expression, but a check learns that it is dimensionally correct. The responsivity is quadratic in x_s. This is illustrated graphically in Figure 3.10.

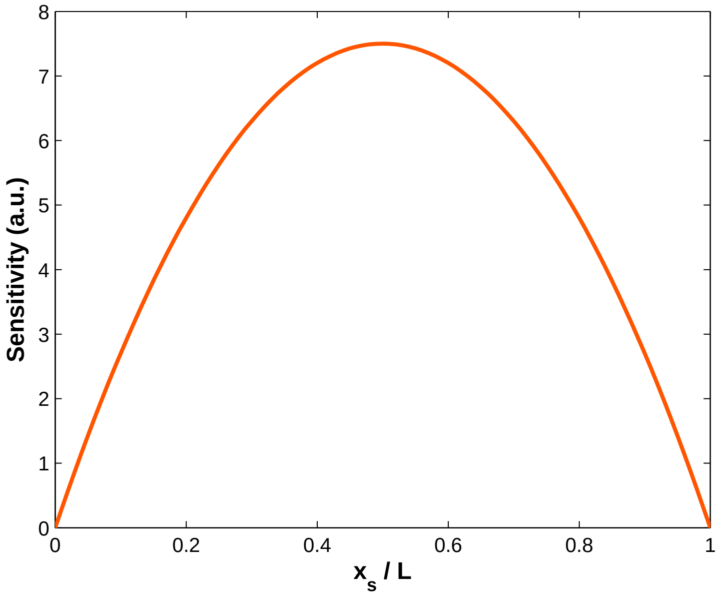

FIGURE 3.10: The responsivity is quadratic in x_s and has a maximum value at $x = L/2$.

The maximum responsivity is reached at $x_s = \pm L/2$ so that is the most sensible location to place the sensor electrodes. Since the flow velocity depends linearly on the angular acceleration, so does the responsivity. Therefore, $x = \pm L/2$ is also the most sensible location for a flow or pressure driven (rather than angular acceleration driven) device.

The responsivity for an *alternating* flow is, however, a little more complex. Recall that the change in temperature δT_0 for the downstream region reads (Equation 3.31):

$$\delta T_0(x) = A_3 \cos\left[\zeta(\omega)(1-j)x\right] - B_3 \sin\left[\zeta(\omega)(1-j)x\right] - j\frac{v_0 Q x_h}{\omega k} \tag{3.44}$$

Because both α, ζ and the constants A_3 and B_3 depend on ω, we find:

$$S = \alpha_R \left.\frac{\partial|\delta T_0|}{\partial \alpha}\right|_{x=x_s} \tag{3.45}$$

$$= \alpha_R \frac{\partial|\delta T_0|}{\partial \omega}\frac{\partial \omega}{\partial \alpha} \tag{3.46}$$

For the latter we find:

$$\alpha = -\phi_0\omega^2 \rightarrow \omega = \sqrt{\frac{-\alpha}{\phi_0}} \tag{3.47}$$

$$\frac{\partial \omega}{\partial \alpha} = \frac{-1}{2\sqrt{-\phi_0\alpha}} = \frac{-1}{2\omega\phi_0} \tag{3.48}$$

Hence the responsivity S is defined as:

$$\boxed{S = \frac{\alpha_R}{2\omega\phi_0}\frac{\partial|\delta T_0|}{\partial \omega}} \tag{3.49}$$

Evaluation yields a rather long expression. The result is plotted below.

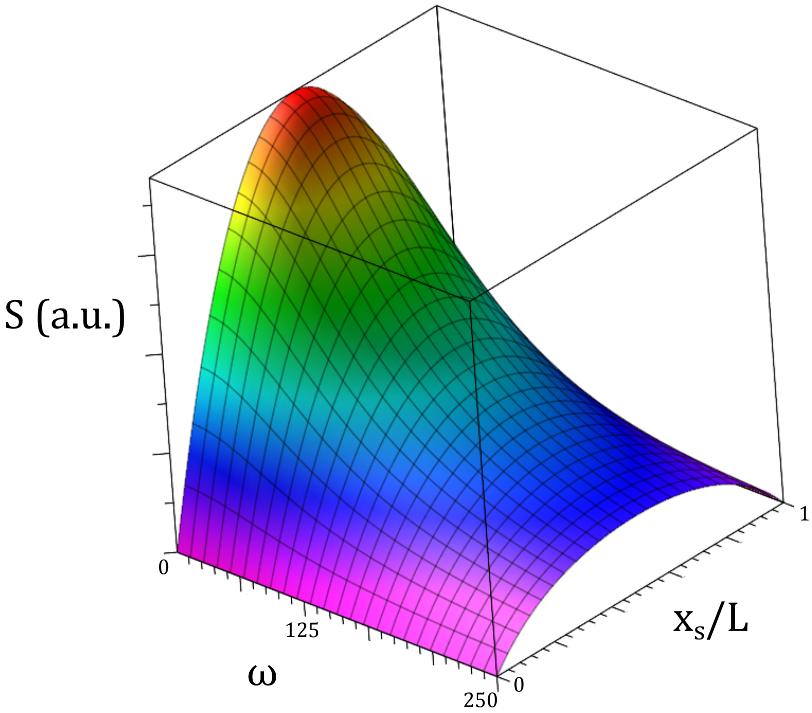

FIGURE 3.11: The responsivity as a function of ω and x.

Since δT_0 decreases with increasing ω, so does S. However, the maximum responsivity is still located at $x_s/L = 1/2$. So placing the sensor electrodes at $x = \pm L/2$ is also for an alternating flow the most sensible location.

3.1.3 Numerical simulations

To investigate the validity of the one dimensional model of the sensor a 3D simulation has been performed in COMSOL Multiphysics 4.3. The geometry is depicted in Figure 3.12.

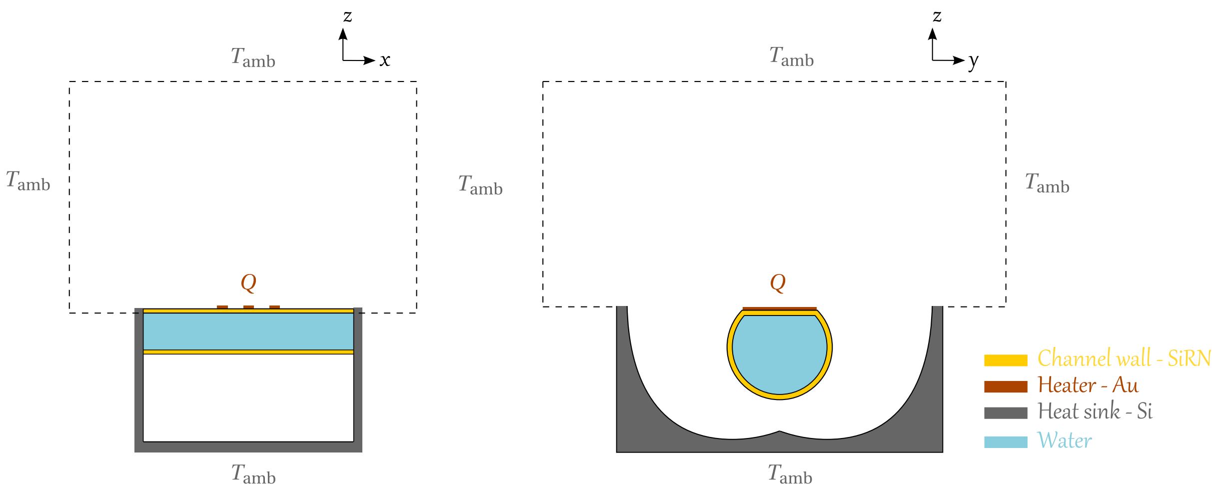

FIGURE 3.12: Three dimensional representation of the sensor. Left: cross section in the length direction. The silicon under the channel and and the silicon where the channel is submerged in is set to a fixed temperature T_{amb}. For away from the sensor the temperature is also at ambient temperature. Right: normal cross section of the tube. Similar to the left figure, the silicon under the channel is set to a reference temperature. The heater is given a fixed heat production per unit volume, Q. Note that these figures are illustrations only and they are not to scale.

At the silicon the temperature is fixed to a constant ambient temperature. Far away from the sensor, the temperature also has this value. To simulate this, a large 'box' of air is made around the sensor. Also, in reality, the channel is curved (torus shaped). This complicates the simulation a lot so a straight channel[5] is assumed. This is a valid assumption as long as the channel's diameter is small compared to the system radius R_c. The following values have been used in the simulation:

Feature	value
Resistor	$0.2 \times 10 \times 40\ \mu$m
Released part of the channel	500 μm
Distance from channel to silicon (radially)	200 μm
Channel wall thickness	1 μm
Channel cross section	$1.07 \cdot 10^{-3}$ mm^2
T_{amb}	293.15 K
Power	1 mW

TABLE 3.1: The values used in the simulation

The results are illustrated in Figure 3.13 until 3.16.

[5]straight in the direction parallel to the flow

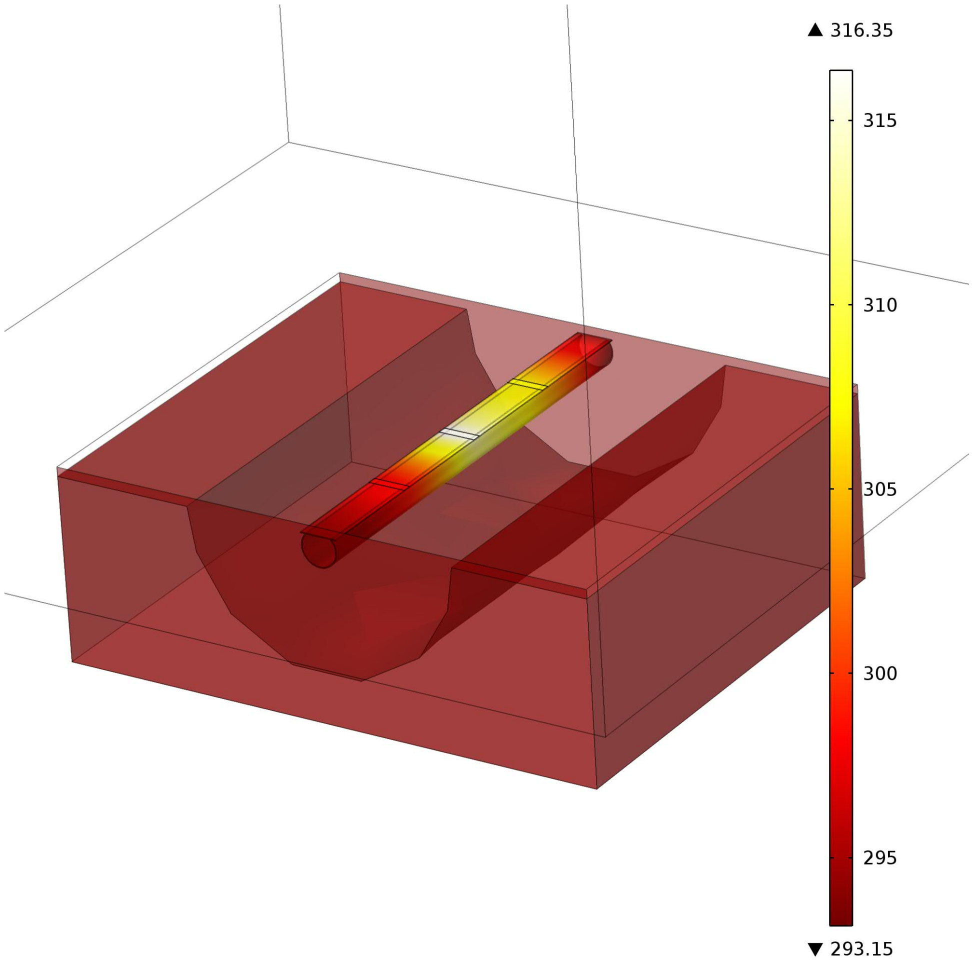

FIGURE 3.13: The temperature for a very high flow velocity (10 mm/s). The temperature downstream is higher than upstream.

A 3D plot is helpful in a brief understanding of the general system, but does not provide a lot of quantitative insight. We are interested in the change in temperature in the channel as a function of the applied flow. Therefore, the temperature and change in temperature in the center of the channel (water) and in the nitride layer (nitride) is plotted in Figure 3.14.

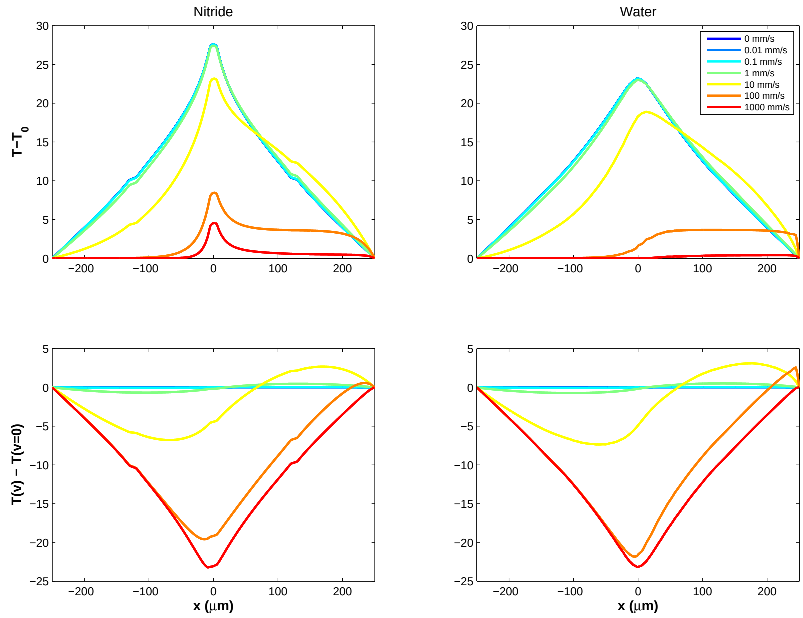

FIGURE 3.14: Top: temperature profile for the nitride layer and in the center of the channel for various flow velocities. Bottom: the change in temperature.

For small velocities, the temperature profile is fairly linear outside the heater and the change in temperature is symmetrical. The higher the velocity, the less linear the profile becomes. Also, the entire sensor starts to cool down: the change in temperature is entirely negative. To investigate the region of interest, that is where the temperature profile is linear, we take a closer look at velocities below 1 mm/s.

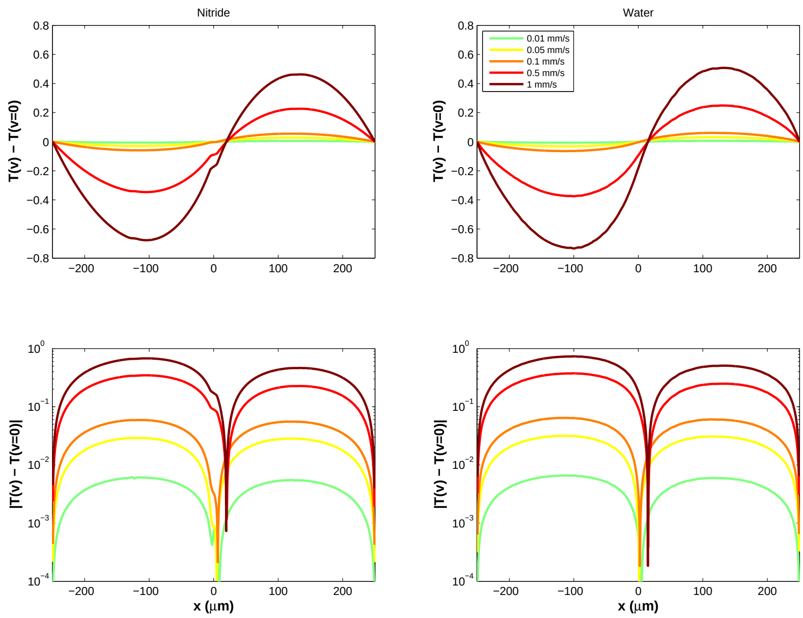

FIGURE 3.15: Top: change in temperature for various flow velocities on a linear scale. Bottom: the absolute value of the change in temperature on a semilogarithmic scale.

From Figure 3.15 we can observe that the temperature profile is symmetrical for velocities below approximately 0.1 - 1 mm/s. We are interested in the region where $\Delta T(v)$ is linear, since that is the regime where the applied angular acceleration scales linear with the voltage measured. This is illustrated in Figure 3.16

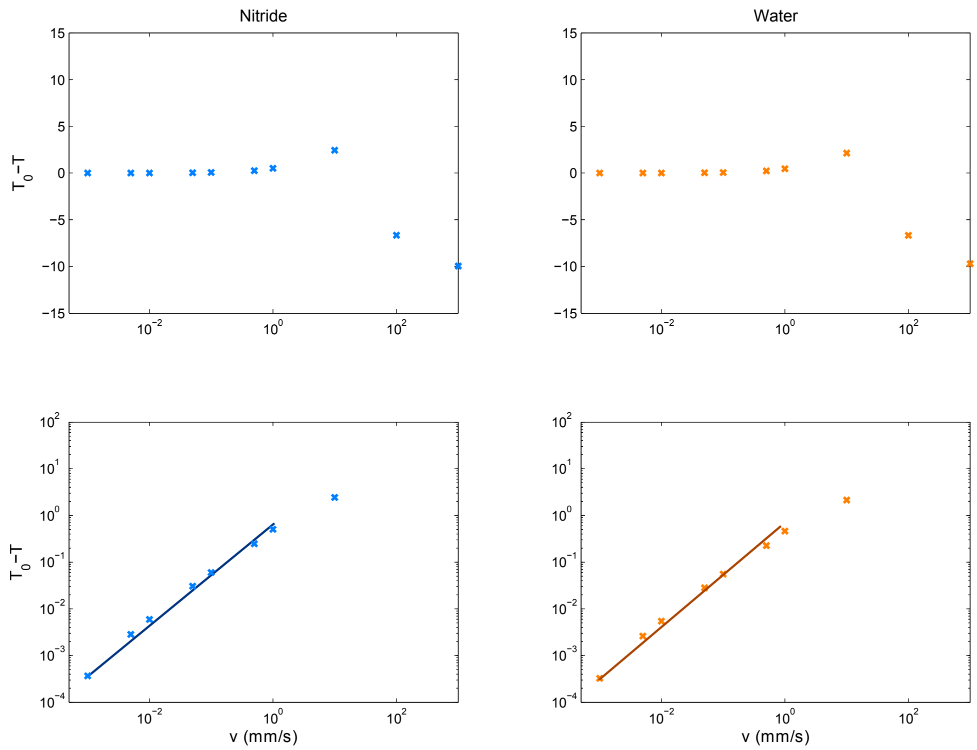

FIGURE 3.16: Temperature as a function of flow velocity for the nitride layer (left) and water (right). The top shows a linear plot, the bottom one a logarithmic one. For flow velocities up to approximately 0.1 -1 mm s^{-1} the temperature difference scales linearly. For higher velocities, the whole sensor cools down and the temperature difference becomes negative. This is not plotted in the logarithmic plots.

Note that all simulations have been performed for a constant flow velocity. The frequency dependent behavior has not been taken into account here.

Comparison to analytical model

To investigate the validity of the simulations the results are compared to the analytical model. For the analytical model the values from Table 3.1 are used. In addition, the effective k and Q read:

$$k = \frac{k_{\mathrm{SiRN}} A_{\mathrm{SiRN}} + k_{\mathrm{water}} A_{\mathrm{water}}}{A_{\mathrm{tot}}} = 2.47 \quad \mathrm{W\,m^{-1}K^{-1}} \tag{3.50}$$

$$Q = Q_{\mathrm{total}} \frac{A_{\mathrm{heater}}}{A_{\mathrm{channel}}} = Q_{\mathrm{total}} \cdot 7.4 \cdot 10^{-3} \quad \mathrm{W\,m^{-3}} \tag{3.51}$$

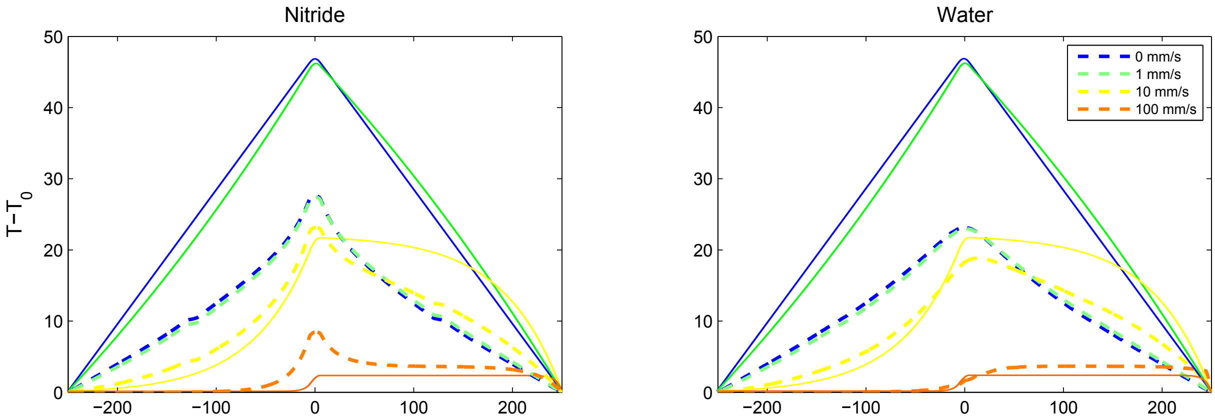

FIGURE 3.17: Comparison between the COMSOL simulations and the analytical model for the nitride layer (left) and the middle of the channel (right). The dashed line indicates the simulations results whereas the solid ones denote the analytical model.

It can be observed from Figure 3.17 that the analytical and COMSOL model are quite alike, especially for the temperature profile in the middle of the channel. The temperature profile in the nitride layer is slightly different from the analytical one in shape, as we could have expected: the 1D model assumes a constant cross sectional area, thermal conductivity and density. This is a very good approximation in the center of channel, but the geometrical details in the nitride layer are not taken into account in the analytical model.

For (relatively) low flow velocities the analytical model overestimates the temperature from the simulations. The more the flow velocity increases, the less the overestimation becomes. This can be explained by the fact that the analytical solution does not take heat conduction through the air into account whereas the numerical simulations do. The higher the flow velocity, the more heat is transfered through *convection* in the flow direction rather than conduction in the radial direction. Since the analytical model does take heat convection in the flow direction into account, the relative difference between the numerical and analytical solution becomes smaller.

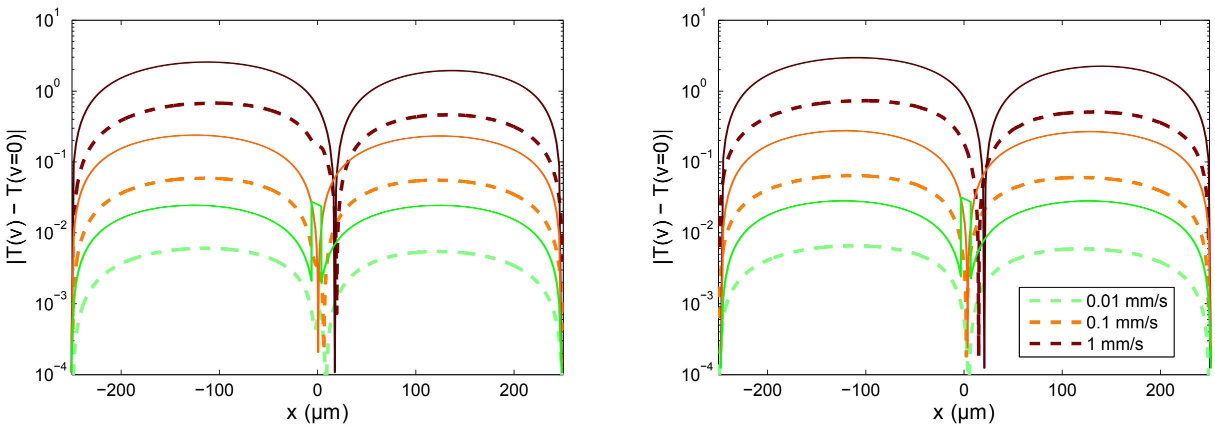

FIGURE 3.18: Comparison between the change in temperature (absolute value) for the COMSOL simulations (dashed lines) and the analytical model (solid lines) for low flow velocities. Left: the nitride layer, right: the middle of the channel.

The analytical and numerical results are also similar for small velocities (Figure 3.18). As indicated, the analytical solution overestimates the numerical one. This is more significant for these low velocities than for high ones. However, the shape of the curve, is very similar: the antisymmetry in absolute temperature for v =1 mm/s is visible for both the numerical and the analytical solution. Note that also the shift of the symmetry center (where $\Delta T \rightarrow 0$) shifts for both the analytical and numerical results. It should also be noted that the difference in the shape of the curve between the nitride layer and the middle of the channel is not as predominant as it is for high flow velocities. The spike in the temperature profile for v = 0.01 mm/s around $x = 0$ does not have a physical cause, but is caused by the finite resolution of the software used to plot these graphs. It converges to zero in this region.

So the numerical simulations are in accordance with the analytical model. The analytical model slightly overestimates the numerical model, but especially for low velocities, the shape temperature profile is very much alike.

3.2 Sensor design

The fabrication process is very briefly as follows. We start with a silicon on insulator (SOI) wafer and a deposit a layer of silicon nitride (SiRN) on it. A 40 μm diameter channel is etched and afterwards covered with silicon nitride again to close it. Electrodes that are used in the thermal readout are sputtered onto the channel. The entire channel is now buried in silicon, which is an extremely good heat conductor that prevents the thermal readout technique from working. Therefore, in the regions of the channel where the flow velocity is measured by thermal readout, the channel is released from the silicon so it is thermally insulated in the radial direction. A very brief overview is given in Figure 3.19.

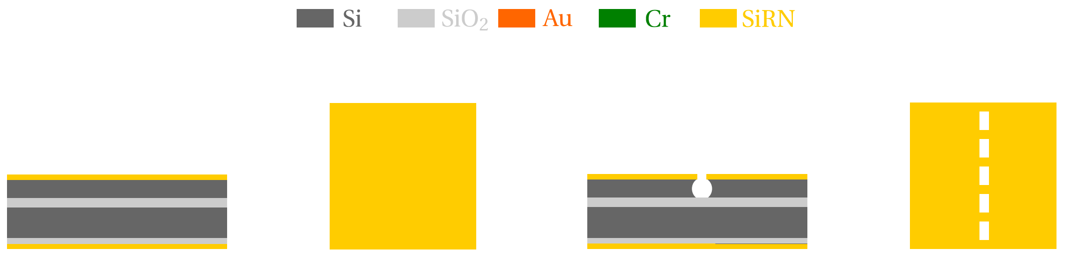

(a) A layer of SiRN is depositied on the wafer.

(b) The channel is created by etching. After this step the channel is still open.

(c) Another layer of SiRN is grown to close the channel.

(d) The electrodes are sputtered onto the channel.

(e) The silicon under the channel is etched to create a thermal insulation from channel to silicon.

FIGURE 3.19: Very brief overview of the fabrication process. Left: cross sectional view, right: top view.

The design of the sensor is limited by the design rules and constraints of the fabrication process. The most important constraints to be taken into account are listed in the table below.

Feature	value
Chip area	7.3×7.3 mm^2
Channel width	40 μm
Metal layers	1 (gold, 200nm thick)
Bondpad size	300×300 μm

There is, however, a number of important features that can be designed.

- Heater geometry (including release etch)
- Number of sensing configurations per chip
- Specific readout design

- System radius and channel diameter

We will briefly address these points to find the optimal design.

3.2.1 Heater geometry

The heater geometry is one of the most important features of the sensor. We need at least one heating- and one sensing resistor. So in principle we could use two 'hybride' electrodes: if the flow is to the left, the right one acts as heater and the left one as sensor, if the flow is to the right, the electrodes will act vice versa. The disadvantage is, however, that *both* electrodes will heat up as they both act as heater and sensor. The associated power spectral density of the noise reads [1]:

$$\bar{v}_n^2 = 4k_B TR \tag{3.52}$$

So it is favorable to keep both temperature and resistance as low a possible to reduce the noise contribution. Therefore, are three wire geometry is chosen: one heating element in the middle and two sensing element to the left and the right.

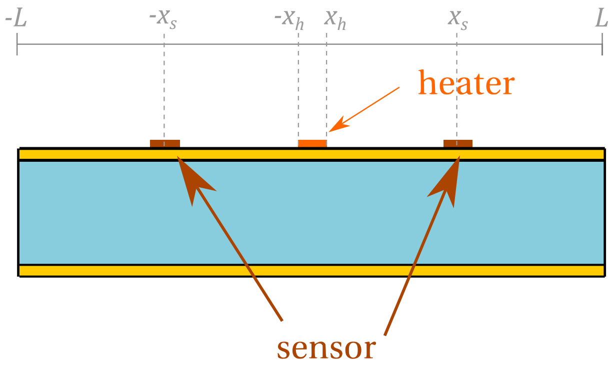

FIGURE 3.20: To reduce the thermal noise, a three wire geometry is used: one heating and two sensing elements. The sensors can still measure flow in two directions.

Since the sensors are not heated as much as the heater, the temperature remains lower and hence the thermal noise is reduced. Because two wires are used, flow can still be sensed in both directions (to the right and to the left).

A number of features to be designed remain: the distance of the sensors with respect to the heater and silicon, the length of the released part of the channel (that is, where thermal readout is active) and the specific dimensions of the heater and sensor elements.

The sensing elements measure the flow velocity by a change in temperature. Therefore, it is favorable to place them where the temperature change is maximum for a given flow velocity. Recalling the responsivity expression in Equation 3.43 learns that the maximum responsivity is in the middle between heater and silicon. Hence the location of the sensors x_s reads:

$$x_s = \pm\frac{L}{2} \tag{3.53}$$

The length of the channel that is released from the silicon ($2L$) should not be too large. First, the longer your make the channel, the fewer sensing configurations will fit on one chip. Furthermore, the description of the sensor physics in only one dimension will become less and less accurate, which complicates the physical modeling. It should, however, also not be too small. The model in Equation 3.15 shows that, for given sensor position x_s and heat source Q, the temperature difference increases with increasing L. Furthermore, if L is very small, it will become hard to actually etch the silicon underneath the channel to release the channel from the silicon. Also, the so called *underetch* will become important. In the process of etching the silicon is not etched exactly until the wall, but will slightly underetch.

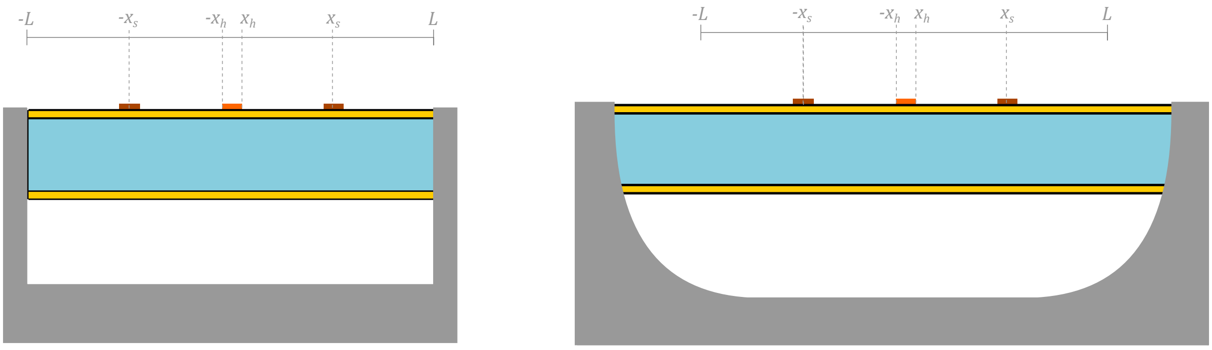

FIGURE 3.21: Left: ideal etch, right: actual etch. The channel is slightly underetched.

The size of the underetch can be significant and is hard to predict. Especially when L is small this can become of importance. So the size of L should be somewhere between 'large' and 'small'. It is therefore chosen to be 250 μm so that the released part of the channel has a total length of 500 μm. To reduce the effects of the underetch, the area that will be released is designed in a triangular shape.

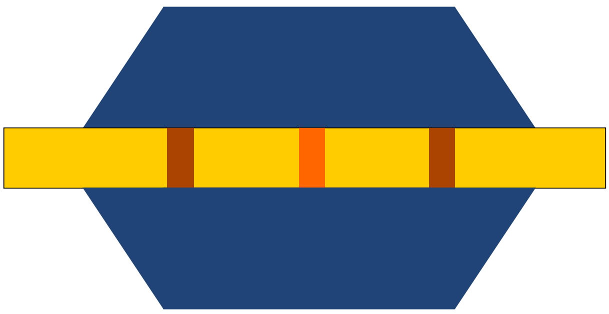

FIGURE 3.22: Topview of the channel. To reduce the underetch, a triangular shaped etch mask (indicated in blue) is used. This geometry will reduce that underetech in the direction parallel to the channel.

The width of the electrodes should be small compared to both L and to the wires connecting them to the outside world, since the resistance R scales with the width of electrode:

$$R = \rho \frac{l}{A} \tag{3.54}$$

In which ρ is the electrical resistivity of gold. If the electrodes are too small, it can no longer be fabricated. Therefore, the width is chosen to be 10 μm.

3.2.2 Number of sensing configurations

With a chip area of 7.3×7.3 mm^2 and a released channel length of 500 μm there is room for more than one sensing configuration (one heater and two sensor resistors). If we have multiple sensing configurations, we measure multiple times and increase the signal by n, the number of configurations. We also, however, increase the resistance of the total sensing configuration by n, which will result in an increase in the noise power spectral density. But the latter scales with $\sqrt{R}$ and therefore with $\sqrt{n}$. Hence the total signal scales with $\sqrt{n}$ so it is favorable to put as many sensing configurations as possible on one chip.

3.2.3 Specific readout design

The flow velocity is sensed by the change in resistance of the up- and downstream resistor. An applied angular acceleration that results in a flow velocity is, however, not the only source of temperature variations and therefore variations in resistance. Various environmental factors, such as a person entering the room, can alter the ambient temperature. To eliminate these effects a Wheatstone like bridge configuration as illustrated in Figure 3.23 is used.

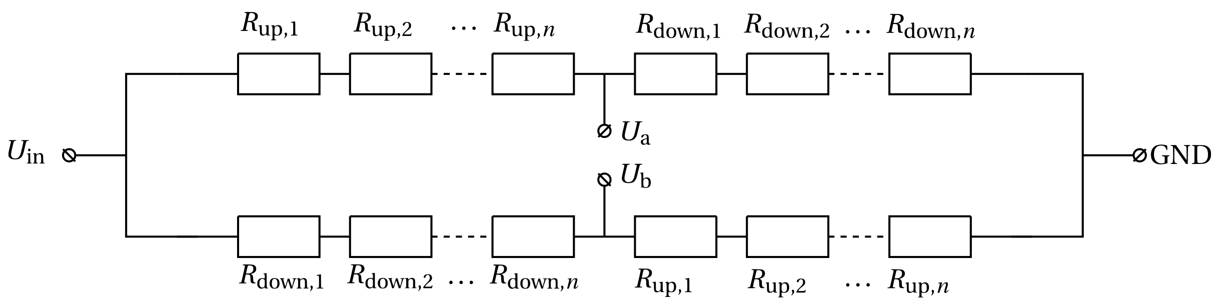

FIGURE 3.23: Wheatstone like bridge configuration to measure the change in resistance. The potential difference U_{ab} is proportional to the change in resistance ΔR.

The potential U_{a} can be expressed in terms of the input U_{in} and the up- and downstream resistance. For the sake of simplicity, we take $n = 1$ in this analysis [6]. Because of the symmetry of the system the current i in each branch can be expressed:

$$i = \frac{U}{R} = \frac{U_{\text{in}} - U_{\text{a}}}{R_{\text{up},1}} = \frac{U_{\text{in}} - U_{\text{a}}}{R_0 + \Delta R} \tag{3.55}$$

$$= \frac{U_{\text{a}}}{R_{\text{down},1}} = \frac{U_{\text{a}}}{R_0 - \Delta R} \tag{3.56}$$

[6]Since the up- and downstream resistors are in series the analysis won't change for $n > 1$: the resistances will just add up.

As $R_{\text{down},1}$ and $R_{\text{up},1}$ are in series the current through both resistors is equal. Equation both expressions gives an equation for U_a:

$$U_\text{a} = \frac{U_\text{in}}{2}\left(1 - \frac{\Delta R}{R_0}\right) \tag{3.57}$$

Analogous to this derivation we obtain for U_b, and hence U_ab:

$$U_\text{b} = \frac{U_\text{in}}{2}\left(1 + \frac{\Delta R}{R_0}\right) \tag{3.58}$$

$$U_\text{ab} = U_\text{b} - U_\text{a} = U_\text{in}\left(\frac{\Delta R}{R_0}\right) \tag{3.59}$$

So U_ab is linearly depended on ΔR, hence also on the applied acceleration. The bridge configuration amplifies the output signal and also cancels other effects that can cause a change in resistance other than the applied acceleration, such as an increase in the ambient temperature. Furthermore, since we actuate it with a known signal U_in, we can amplify U_ab at the frequency of U_in, which allows us to measure even lower voltages.

One half of the upstream resistors should be connected with one half of the downstream resistors and vice versa. The first connection can be made 'outside' the channel, the second one inside.

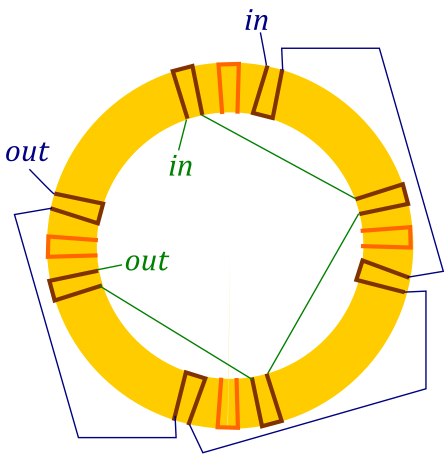

FIGURE 3.24: The resistors can be connected by a connection outside (blue) and inside the channel (green).

However, the heater resistors of each sensing configuration also have to be connected. This is not possible without wires crossing each other. Since we only have one metal layer, the heaters are connected by bondpads and wires.

3.2.4 System radius and channel diameter

It is beneficial to maximize the flow velocity for a given angular acceleration since the higher the flow velocity, the higher the change in temperature at the sensing resistor and therefore the higher the signal. Recall from Chapter 2 that the flow profile reads:

$$v(r,t) = \frac{R_c\alpha}{4\nu}\left(R^2 - r^2\right)\exp(j\omega t) \tag{3.60}$$

So the sensor benefits from a large system radius R_c and a large channel radius R. This conflicts with the design of a *micro*machined sensor. To investigate to what size we can downscale the sensor, three different values of R_c are used: 1, 2 and 2.6 mm. Because of limitations in the fabrication process we cannot increase the diameter of the channel. We can, however, make it wider.

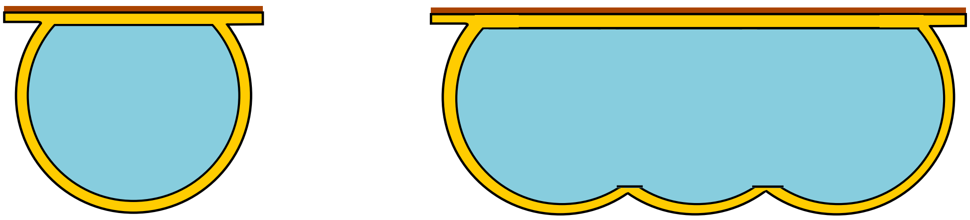

FIGURE 3.25: Left: 'normal' channel, right: wide channel.

Both the normal and the wide channel will be used in the sensors with R_c equal to 1,2 and 2.6 mm. The total number of angular acceleration sensor designs therefore comes down to 6.

3.2.5 Overview

In addition to the angular acceleration sensors, a linear flow chip has been designed. Rather than generating a fluid flow by an angular acceleration, this chip is actuated by a flow source. This design is used to verify the modeling used to develop the angular acceleration sensors. This design includes both the normal and the wide channel. It has one sensing configuration with electrodes on multiple locations to verify if the ideal sensor position is indeed $\pm L/2$. This configuration is measured by a four point measurement to provide even more reliable results [7].

The sensors have been given names to distinct them. An overview of the designs is found in the table below.

[7] The small chip area prevents this from being applicable to the angular acceleration designs.

Name	R_c (mm)	Diameter	Number of sensing configurations	notes
Longyearbyen	1	normal	3	
Kangerlussuaq	1	wide	3	
Ny-Ålesund	2	normal	6	
Sisimiut	2	wide	6	
Barentsburg	2.6	normal	7	
Ilulissat	2.6	wide	7	
Vancouver	-	both	3	Flow driven

The full mask designs can be found in Appendix C.

Chapter 4

Electromagnetic readout

This chapter deals with the development of an angular acceleration sensor that uses *electromagnetic* readout. The basic sensor geometry is the same as for the sensor discussed in the previous chapter: a torus shape fully circular channel is filled with a fluid. When an angular acceleration is applied, the fluid will start to flow.
If the fluid is conductive and we apply a magnetic field normal to the flow direction, the Lorentz force causes the positive ions to move one way whereas the negative ones will go the other. This charge separation leads to a voltage that in principle can be measured.

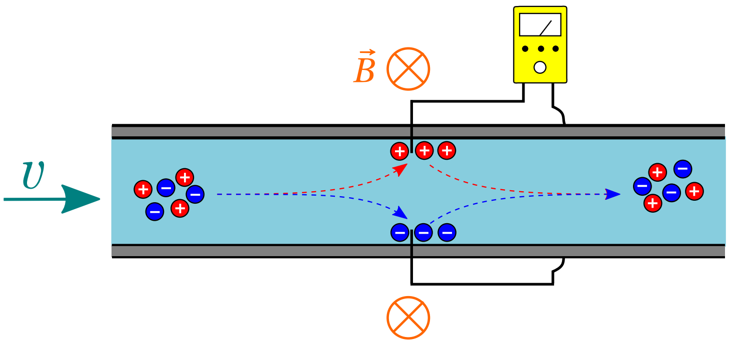

FIGURE 4.1: Illustration of the principle of electromagnetic flow measurement.

4.1 Theory and modeling

The Lorentz force $\vec{F}_L$ reads:

$$\vec{F}_L = q(\vec{E} + \vec{v} \times \vec{B}) \tag{4.1}$$

We will align the magnetic field in such a way that $\vec{v} \perp \vec{B}$. For a stationary situation we know that the Lorentz force induced by the magnetic field (the $q\vec{v} \times \vec{B}$ term) will be canceled by the one induced by electric field (the $q\vec{E}$ term) due to the separated charge carriers. Hence we find:

$$F_L = q(E + vB) = 0 \rightarrow E = -vB \tag{4.2}$$

Finding the induced voltage:

$$V = -\int_L \vec{E} \cdot \mathrm{d}\vec{l} = Ed \tag{4.3}$$

$$= -vBd \tag{4.4}$$

So the measured potential difference depends linearly on the flow velocity and therefore on the angular acceleration. This linear relation makes electromagnetic readout a potentially interesting technique.

4.1.1 Alternating magnetic field

Equation 4.4 is a very compact and insightful equation, but is it only valid for a stationary situation. Typical induced voltages are in the order of millivolts or smaller, so it is hard to perform an accurate DC measurement. Using an alternating magnetic field will allow us to amplify and filter the signal at the frequency of the magnetic field and therefore measure much smaller voltages. Since the magnetic field is not time independent anymore, the physics becomes a lot more complicated. There are two major effects that become apparent: the skin effect due to the self inductance and displacement currents.

Due to the changing magnetic field (relative to the fluid) circulating eddy currents arise, which cancel currents in the center and reinforce them close to the surface. The current density j can therefore be described as [20, 21]:

$$j = j_0 \exp(-r/R_s), \quad R_s = \frac{1}{\sqrt{\pi f \sigma \mu}} \tag{4.5}$$

In which j_s is the current density at the surface, σ the fluid's conductivity and μ its magnetic permeability. R_s is called the *skin depth.* If this quantity is large compared to the channel's diameter, the skin effect can be neglected. This gives an indication until what frequencies the analysis above is still valid.

$$\frac{1}{\sqrt{\pi f \sigma \mu}} \gg d \tag{4.6}$$

$$f \ll \frac{1}{\pi \sigma \mu d^2} \tag{4.7}$$

With sub millimeter values for d and tap water as a fluid, this threshold frequency is much higher than 1 kHz. Therefore, it should not cause any problems in real life situations.

The effect of displacement currents also has to be taken into account. For a linear medium, the displacement current $\vec{j}_D$ is described as:

$$\vec{j}_D = \frac{\partial \vec{D}}{\partial t} = \epsilon \frac{\partial \vec{E}}{\partial t} \tag{4.8}$$

As described in the beginning of this chapter, the conduction current $\vec{j}$ obeys the following expression:

$$\vec{j} = \sigma(\vec{E} + \vec{v} \times \vec{B}) \tag{4.9}$$

In order to neglect the effects of the displacement currents, $\vec{j}_D \ll \vec{j}$. If the system changes harmonically in time with angular frequency $\omega = 2\pi f$, we know:

$$\vec{j}_D \propto \epsilon\omega, \quad \vec{j} \propto \sigma \tag{4.10}$$

So for the displacement current to be negligible compared to the conduction current it should hold that:

$$\frac{\vec{j}}{\vec{j}_D} \propto \frac{\sigma}{2\pi f \epsilon} \gg 1 \tag{4.11}$$

Hence

$$f \ll \frac{\sigma}{2\pi\epsilon} \tag{4.12}$$

Even for ultra pure deionized water, which has a conductivity of approximately 10 μS cm^{-1} this frequency is higher than 1 kHz. Therefore the displacement currents are small in practical applications.

Note that a very low conductivity σ will, however, give rise to other problems: the smaller σ becomes, the higher the resistance of the channel. If it gets comparable to the input impedance of a multimeter it will be very hard to measure the voltage within the channel.

4.1.2 Non-uniform flow profile

Equation 4.4 is valid for an *uniform* flow velocity. In pipeflow, however, the flow profile is generally not uniform. A more extensive analysis is therefore required. As described by Shercliff [22] and Kolin [23], the governing equation for the currents in the fluid is Ohm's law:

$$\vec{j} = \sigma(\vec{E} + \vec{v} \times \vec{B}) \tag{4.13}$$

If the frequency is low enough to neglect the skin effect, we have a conservative field and can therefore write the electric field as the gradient of a scalar potential V:

$$\nabla \times \vec{E} = 0 \tag{4.14}$$

$$\vec{E} = -\nabla V \tag{4.15}$$

Next, if we also assume that the frequency is also sufficiently low to neglect any displacements currents ($\omega\epsilon/\sigma \ll 1$ so that $\frac{\partial D}{\partial t} = 0$) we have.

$$\nabla \times \vec{B} = \mu \vec{j} \tag{4.16}$$

So Equation 4.16 indicates how the induced currents $\vec{j}$ affect the magnetic field. Next, if we determine the divergence we find:

$$\mu\nabla \cdot \vec{j} = \nabla \cdot (\nabla \times \vec{B}) = \frac{\partial^2 B_z}{\partial y \partial x} - \frac{\partial^2 B_y}{\partial z \partial x} + \frac{\partial^2 B_x}{\partial y \partial z} - \frac{\partial^2 B_z}{\partial x \partial y} + \frac{\partial^2 B_y}{\partial x \partial z} - \frac{\partial^2 B_x}{\partial y \partial z} = 0 \tag{4.17}$$

Combining Equation 4.17 and Equation 4.13 gives:

$$\nabla \cdot \vec{j} = \nabla \cdot (\sigma(\vec{E} + \vec{v} \times \vec{B})) = 0 \tag{4.18}$$

$$= \nabla \cdot (\sigma(-\nabla V + \vec{v} \times \vec{B})) = 0 \tag{4.19}$$

$$\nabla^2 V = \nabla \cdot (\vec{v} \times \vec{B}) \tag{4.20}$$

We can rewrite this using the vector identity $\nabla \cdot (\vec{v} \times \vec{B}) = \vec{B} \cdot (\nabla \times \vec{v}) - \vec{v} \cdot (\nabla \times \vec{B})$. The induced currents described in Equation 4.16 flow in the plane perpendicular to the flow velocity ((x, y)-plane). Hence

$$\vec{v} \cdot \underbrace{(\nabla \times \vec{B})}_{=\mu\vec{j}} = v\left(\frac{\partial B_y}{\partial x} - \frac{\partial B_x}{\partial y}\right) = 0 \tag{4.21}$$

Equation 4.20 therefore simplifies to

$$\boxed{\nabla^2 V = \vec{B} \cdot (\nabla \times \vec{v})} \tag{4.22}$$

Which provides the basic equation to find the measured potential difference for a non-uniform flow profile.

Circular channel

Equation 4.22 is readily solved for a circular channel with a parabolic flow profile. If $\vec{B}\perp\vec{v}$ the equation reduces to[1]:

$$\nabla^2 V = B\frac{\partial v}{\partial y} \tag{4.23}$$

Because of the geometry it is sensible to use cylindrical coordinates. If we assume the pipe to be straight in the axial direction we obtain[2]

$$\begin{aligned}\nabla^2 V &= \frac{\partial^2 V}{\partial z^2} + \frac{1}{r^2}\frac{\partial^2 V}{\partial \phi^2} + \frac{1}{r}\frac{\partial}{\partial r}\left(r\frac{\partial V}{\partial r}\right) && (4.24)\\ &= B\frac{\partial v}{\partial r}\frac{\partial r}{\partial y} && (4.25)\end{aligned}$$

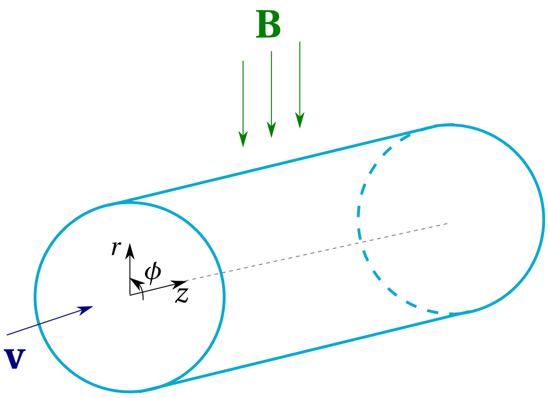

(a) Cylindrical coordinates

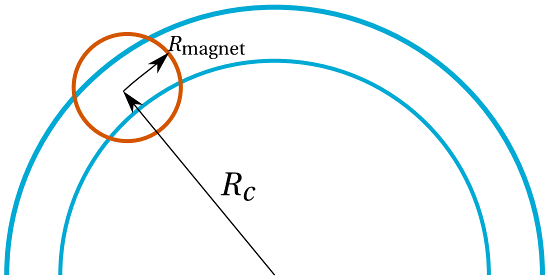

(b) The magnet radius should be small compared to the full systems circumference, $2\pi R_c$.

FIGURE 4.2: The symmetry of the geometry makes it sensible to use cylindrical coordinates.

If we assume that V is independent of z, which is a good approximation as long as the channel's radius is small compared to the magnet's radius we obtain:

$$\begin{aligned}\nabla^2 V &= \frac{1}{r^2}\frac{\partial^2 V}{\partial \phi^2} + \frac{1}{r}\frac{\partial}{\partial r}\left(r\frac{\partial V}{\partial r}\right) && (4.26)\\ &= B\frac{\partial v}{\partial r}\sin\phi && (4.27)\end{aligned}$$

Assuming a solution of the form $V = F(r)\sin\phi$ provides a solution to the above differential equation:

[1] This is valid if we assume that the magnetic field generated by the induced current does not affect the applied external magnetic field.

[2] This is a good assumption as long as the region considered is small compared to the full system circumference, i.e. $R_{\text{magnet}} \ll 2\pi R_c$.

$$\frac{1}{r^2}\frac{\partial^2 V}{\partial\phi^2}+\frac{1}{r}\frac{\partial}{\partial r}\left(r\frac{\partial V}{\partial r}\right)=B\frac{\partial v}{\partial r}\sin\phi \tag{4.28}$$

$$\left(\frac{\partial^2 F(r)}{\partial r^2}+\frac{1}{r}\frac{\partial F(r)}{\partial r}-\frac{1}{r^2}F(r)\right)\sin\phi=B\frac{\partial v}{\partial r}\sin\phi \tag{4.29}$$

Dividing the $\sin\phi$ term out and rewriting yields the following equation.

$$\frac{\partial^2 F(r)}{\partial r^2}+\frac{\partial}{\partial r}\left(\frac{F(r)}{r}\right)=B\frac{\partial v}{\partial r} \tag{4.30}$$

Integration gives

$$\frac{\partial F(r)}{\partial r}+\frac{F(r)}{r}=Bv+C_1 \tag{4.31}$$

At the wall the velocity is zero and because of continuity, at the wall the normal radial component of the potential gradient zero. Hence $C_1 = F(R)/R$. Another rewriting trick yields:

$$\frac{1}{r}\frac{\partial}{\partial r}(rF(r))=Bv(r)+\frac{F(R)}{R} \tag{4.32}$$

$$\frac{\partial}{\partial r}(rF(r))=Bv(r)r+\frac{F(R)}{R}r \tag{4.33}$$

$$rF(r)=B\int_0^r v(\rho)\rho\,\mathrm{d}\rho+\frac{F(R)r^2}{2R}+C_2 \tag{4.34}$$

For the sake of simplicity we take V to be zero in the middle, i.e. $F(0) = 0$. Hence $C_2 = 0$. We therefore obtain:

$$V=F(r)\sin\phi=\left[\frac{B}{r}\int_0^r v(\rho)\rho\,\mathrm{d}\rho+\frac{F(R)r}{2R}\right]\sin\phi \tag{4.35}$$

The potential of interest is at the electrodes, that is at $r = R$ and $\sin\phi = \pm 1$:

$$V=F(R)=\frac{B}{R}\int_0^R v(r)r\,\mathrm{d}r+\frac{F(R)}{2} \tag{4.36}$$

$$=\frac{2B}{R}\int_0^R v(r)r\,\mathrm{d}r \tag{4.37}$$

Hence we have obtained a closed relation that links the fluid velocity v, channel radius R and magnetic field B. Moreover, if we take a close look at the integral we can even obtain a simpler expression. The average velocity is defined as:

$$v_{\text{avg}} = \frac{1}{A}\iint_S \vec{v}\cdot \mathrm{d}\vec{A} = \frac{1}{\pi R^2}\int_0^R v(r)\underbrace{2\pi r \mathrm{d}r}_{=\mathrm{d}A} \tag{4.38}$$

$$= \frac{2}{R^2}\int_0^R v(r) r \mathrm{d}r \tag{4.39}$$

Hence

$$V = \frac{2B}{R}\underbrace{\int_0^R v(r) r \mathrm{d}r}_{=R^2/2 v_{\text{avg}}} = BRv_{\text{avg}} \tag{4.40}$$

Because of symmetry the total potential difference measured at the electrodes ΔV will be twice this value:

$$\boxed{\Delta V = 2BRv_{\text{avg}}} \tag{4.41}$$

So the voltage measured does not depend on the flow *profile*, but on the average velocity. The only condition is that the profile is symmetrical, so that we can introduce the latter integral. In laminar pipeflow, the flow profile is parabolic, which is symmetric. So in our further analysis we will use the very compact and simple Equation 4.41. Also note that the voltage does not depend on the conductivity of the fluid.

This analysis can also be performed for a channel with a rectangular cross section, which is done in Appendix E.

4.1.3 Magnetic field permanent magnet

Since the voltage does not only depend on the flow velocity, but also on the magnetic field it is important to determine the value of the magnetic flux density B inside the channel. If we define $z = 0$ to be at the edge of the magnet, B along the center line of an axially magnetized cylindrical permanent magnet with radius R and height D can be calculated as [24, 25]:

$$B(z) = \frac{B_r}{2}\left(\frac{D+z}{\sqrt{R^2+(D+z)^2}} - \frac{z}{\sqrt{R^2+z^2}}\right) \tag{4.42}$$

In which B_r is the remanence, which does not depend on the geometry of the magnet.

4.1.4 Responsivity

The responsivity can be defined for a flow and angular acceleration driven sensor, respectively:

$$S_{\text{flow}} = \frac{\partial U}{\partial v} = 2BR \tag{4.43}$$

$$S_{\text{angular}} = \frac{\partial U}{\partial \alpha} = \frac{\rho R_c B R^3}{3\mu} \tag{4.44}$$

Hence a strong magnetic field and a big channel is beneficial for the sensor's function.

4.1.5 Other sources of induced voltage

Ideally, the voltage induced by the magnetic field is the only voltage that is measured. It is, however, to be expected that other phenomena will also induce a voltage that can inhibit the measurement of the magnetically induced one.

Electrochemical

There can be an electrolytic reaction between the (metal) electrodes and the conducting fluid. These can also give rise to a potential.

Inductive and capacitive coupling

For the alternating magnetic field situation, energy can be transfered in the electrical circuit through capacitive and inductive coupling. This can result in voltages.

Streaming potential

In the analysis performed previously we never took potential surface charge into account. In small channels the effects of surface charge cannot be neglected anymore.

Material always has a certain nonzero surface charge. Let's take this charge to be negative in this analysis. It will attract positive ions. These ions will be distributed in two regions: an immobile (the Stern layer) and a mobile one (the Debye layer) [26, 27]. This is illustrated in Figure 4.3

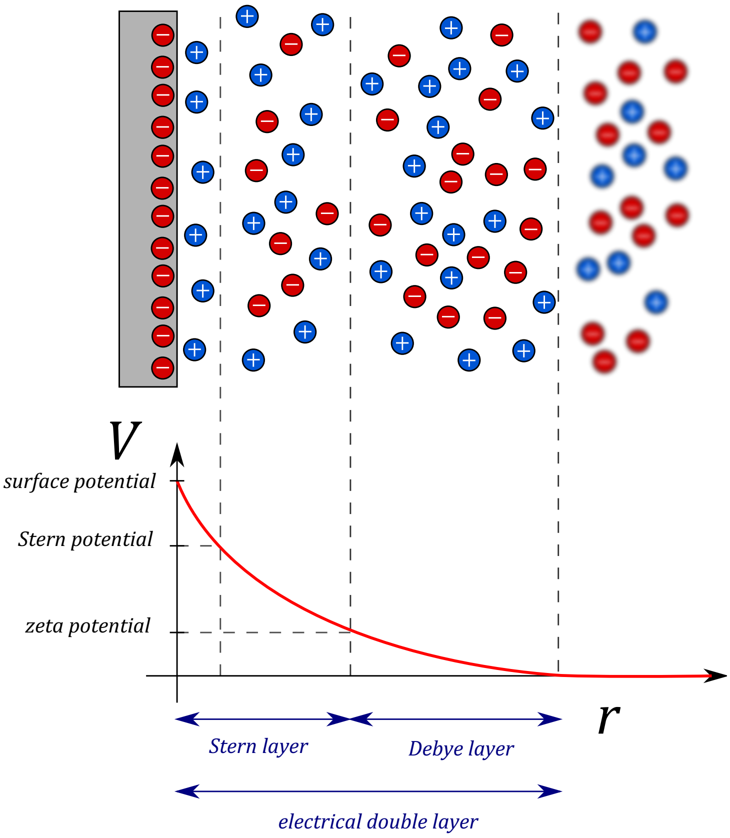

FIGURE 4.3: The potential of a fluid channel. The surface charge induces an excess positive charge near the wall, the electrical double layer (EDL). The ions in the Stern layer are immobile, whereas the counterions in the Debye layer are mobile. Outside the Debye layer the potential is zero again.

The region in which the potential is nonzero is called the *electrical double layer*, EDL. The counter ions in the Debye layer are mobile, so they can be transported when a flow is applied to the channel. The EDL is very small. The order of magnitude is the *Debye length*: $1/\kappa_d$, which is defined as [28, 29]:

$$\kappa_d = \sqrt{\frac{2c_b N_A Z^2 e^2}{\epsilon k_b T}} \tag{4.45}$$

In which c_b is the bulk ion concentration outside the EDL (mol m^{-3}), N_A Avogadro's constant, Z the valence of the ions, e the elementary charge, ϵ the fluid permititvity, k_b Boltzmann's constant and T the (absolute) temperature. For water at room temperature and a pH of 7 the Debye length is in the order of nanometers.

In the Debye layer there is a nonzero charge distribution. If a flow is applied to the channel, the ions in this mobile layer will move, resulting in a charge transport: a *streaming current*. This effect is basically the opposite of electroosmotic flow. By symmetry of the channel and the definition of current, the streaming current i_s is defined as [30]:

$$i_s = \iint_A v\rho \, \mathrm{d}A = 2\pi \int_0^R v(r)\rho(r) r \, \mathrm{d}r \tag{4.46}$$

Note that $v(r)\rho(r)$ is only nonzero in the Debye layer[3]! For a (pressure driven) flow in a cylindrical channel, we find the flow profile:

$$v(r) = \frac{-\Delta P R^2}{4\mu L}\left(1-\left(\frac{r}{R}\right)^2\right) \tag{4.47}$$

In which ΔP is the pressure difference in the direction of flow and L the length of the channel. In order for find an expression for the streaming current, we need to find $\rho(r)$, which is governed by the Poisson equation:

$$\frac{1}{r}\frac{\partial}{\partial r}\left[r\frac{\partial V(r)}{\partial r}\right] = -\frac{\rho(r)}{\epsilon} \tag{4.48}$$

Plugging this into the expression for the streaming current and performing integration by parts we obtain:

$$i_s = -\frac{\Delta P \pi \epsilon R^2}{2\mu L}\int_0^R \left(1-\left(\frac{r^2}{R^2}\right)\right)\left\{\frac{\partial}{\partial r}\left(r\frac{\partial V(r)}{\partial r}\right)\right\} \mathrm{d}r \tag{4.49}$$

Which is an integral that we cannot solve easily, because of the second order r. We can, however, approximate the velocity profile by a linear expression:

$$v(r) = \frac{-\Delta P R^2}{4\mu L}\left(1-\left(\frac{r}{R}\right)^2\right) \approx \frac{-\Delta P R^2}{2\mu L}\left(1-\frac{r}{R}\right) \quad \text{for } r/R \approx 1 \tag{4.50}$$

We are only interested in the flow profile in the Debye layer since outside this layer the potential is zero. De Debye layer is much smaller than R so the linear expression is a very good approximation. We obtain:

$$i_s = -\frac{\Delta P \pi \epsilon R^2}{\mu L}\int_0^R \left(1-\left(\frac{r}{R}\right)\right)\left\{\frac{\partial}{\partial r}\left(r\frac{\partial V(r)}{\partial r}\right)\right\} \mathrm{d}r \tag{4.51}$$

Applying integration by parts two times yields:

$$i_s = -\frac{\Delta P \pi \epsilon R^2}{\mu L}\left\{\left[\left(1-\left(\frac{r}{R}\right)\right) r\frac{\partial V(r)}{\partial r}\right] + \int_0^R \frac{r}{R}\frac{\partial V(r)}{\partial r}\,\mathrm{d}r\right\} \tag{4.52}$$

$$= -\frac{\Delta P \pi \epsilon R^2}{\mu L}\left\{\underbrace{\left[\frac{r}{R}V(r)\right]_{r=0}^{r=R}}_{=\zeta} + \underbrace{\frac{1}{R}\int_0^R V(r)\,\mathrm{d}r}_{\approx 0}\right\} \tag{4.53}$$

The first term between brackets is equal to the ζ potential because $V(R) \equiv \zeta$ (refer to Figure 4.3). The

[3] $v(r)$ is zero in the Stern layer and $\rho(r)$ is zero outside the EDL.

second term is approximately zero: since R is much larger than the EDL the potential is zero almost everywhere in the channel. Hence we find for the streaming current:

$$\boxed{i_s = -\frac{\Delta P \epsilon \zeta A}{\mu L}} \tag{4.54}$$

Where A is the cross sectional area: πR^2. An analysis similar to the one performed above has been done for a channel with a very wide, rectangular shaped, cross section in literature [31–34]. In all analyses the width of the channel is assumed to be much bigger than its height, which is not true for the sensor in this report. However, the expression found for the streaming current is exactly the same as in Equation 4.54 (the only difference is the cross sectional area). Therefore we will use Equation 4.54 in our further analysis.

The streaming current will accumulate positive charge downstream. This accumulation will induce a potential difference in the flow direction: the *streaming potential* V_{sp}. This potential will counteract the the streaming potential by producing a conduction current i_c since the channel has a conductivity σ. In an equilibrium state the two currents are equal. By Ohm's law the conduction current reads:

$$i_c = \frac{\sigma A}{L} V_{\mathrm{sp}} \tag{4.55}$$

To find an expression for the streaming potential we equal Equation 4.54 to Equation 4.55:

$$-\frac{\Delta P \epsilon \zeta A}{\mu L} = \frac{\sigma A}{L} V_{\mathrm{sp}} \tag{4.56}$$

Hence the streaming potential reads

$$V_{\mathrm{sp}} = -\frac{\Delta P \epsilon \zeta}{\mu \sigma} \tag{4.57}$$

Which is defined for a pressure driven flow. We can translate this to a flow driven situation using the Hagen-Poiseuille flow. We find for the average velocity:

$$v_{\mathrm{avg}} = \frac{1}{R} \int_0^R \frac{\Delta P R^2}{4\mu L} \left(1 - \left(\frac{r}{R}\right)^2\right) \mathrm{d}r = \frac{-\Delta P R^2}{6\mu L} \tag{4.58}$$

Hence we can calculate a corresponding ΔP for a flow driven situation:

$$\Delta P = \frac{-6\mu L v_{\mathrm{avg}}}{R^2} \tag{4.59}$$

And obtain for the streaming potential:

$$\boxed{V_{\mathrm{sp}} = \frac{6\epsilon\zeta}{\sigma}\frac{L}{R^2}v_{\mathrm{avg}}} \tag{4.60}$$

This potential does not depend on a magnetic field but is, just like the magnetic potential, linearly depended on the (average) flow velocity. It can therefore inhibit the measurement of the flow velocity by electromagnetic readout.

4.2 Sensor design

The analysis performed in the previous sections is used to obtain an optimal sensor design. The sensors are 3D printed by the commercial manufacturer Shapeways, which has some design rules that limit the design freedom [35]. For a detailed overview of the fabrication process, refer to subsection 5.2.1. An overview of the design rules is given in Table 4.1.

Feature	**Min. dimension (mm)**	**Illustration**
Supported wall thickness	0.3	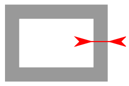
Unsupported wall thickness	0.6	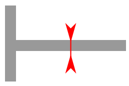
Engraved detail height and width	0.1	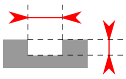
Embossed detail height and width	0.1	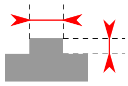
Escape hole	2	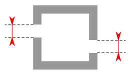

TABLE 4.1: Shapeways design rules

The most important conclusions from these design rules are that the printer can print with a resolution of 100 × 100 μm and escape holes are needed to create cavities such as channels.

Recall that the responsivity S for a flow driven sensor reads:

$$S = 2BR \tag{4.61}$$

So the sensor benefits from a great magnetic field and cross sectional area.

4.2.1 Rectangular flow sensor

To characterize the electromagnetic readout it is favorable to have a well defined flow. Therefore, in addition to the angular acceleration sensor, a linear flow sensor has been developed. This sensor will be actuated by a flow source (syringe pump).

The most important feature to design is the channel. The responsivity increases with increasing R. We aim, however, at a *small* sensor. Furthermore, this analysis is true for a circular cross section. From the design rules we can learn that we are in principle able to make a 100 × 100 μm rectangular channel, but not a circular channel with 100 μm diameter. The perimeter would make steps of 100 μm.

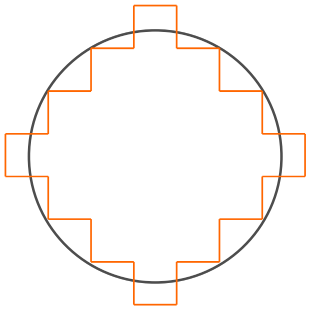

FIGURE 4.4: Gray: the aimed circular cross section, orange: the geometry the printer will make because of its finite resolution.

Therefore, a rectangular cross section is used. We will use the same channel for both the angular acceleration sensor and this linear flow sensor. In principle, the cross sectional area of the channel should be as large as possible, since for a given angular acceleration, the flow velocity scales with the cross sectional area. However, if we make the channel *too* big, we would need very strong magnets. But more importantly, the boundary layer thickness will soon become smaller than the channel dimension and therefore we can no longer use the quasi static flow profile solution.

An advantage of a rectangular geometry over a circular one is that we can choose the width and height independently. Let's call the direction over which we measure the voltage the width of the channel. This should be as large as possible since the potential scales linearly with this dimension. The height should, however, be small for two reasons. First, for a given magnet, the closer the channel is to the magnet, the strong the magnetic field. Second, the boundary layer thickness will be greater than the channel dimension.

Outweighing these demands has lead to a width of 3 mm. The minimum 'channel' the printer can make is 100 μm deep. We take a factor of safety of four and therefore take the height to be 400 μm.

Apart from the channel, we also need to decide what magnet geometry we will use. The magnetic field inside the channel should be as big as possible. We position the channel in between one magnet at $z = 0$ and another one with its field oriented in the same direction at $z = z_0$.

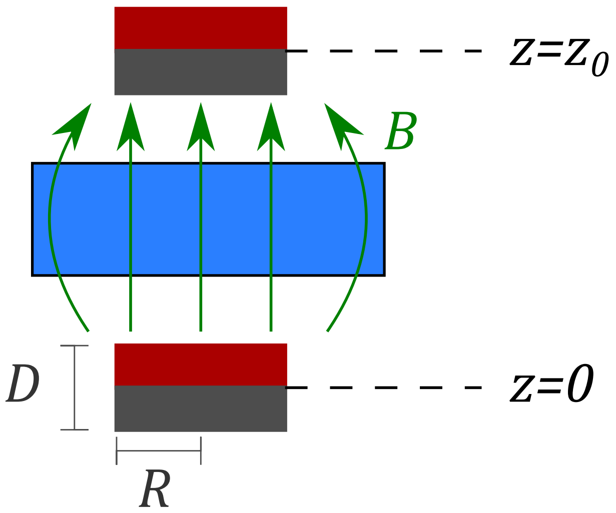

FIGURE 4.5: Illustration of the magnetic field inside the channel.

The corresponding magnetic flux density B as a function of z (where $z = z_0/2$ is the middle of the channel) reads:

$$B(z) = \frac{B_r}{2}\left[\frac{D+z}{\sqrt{R^2+(D+z)^2}} + \frac{D+z-z_0}{\sqrt{R^2+(D+z_0-z)^2}} - \frac{z}{\sqrt{R^2+(z)^2}} - \frac{z-z_0}{\sqrt{R^2+(z_0-z)^2}}\right] \tag{4.62}$$

Hence it is best to make z_0 and R as small as possible and D as large as possible. However, R should be big enough for the magnet to cover the entire width of the channel. Therefore R is taken to be 4 mm. D could be as big a possible, but the sensor should remain compact. Furthermore, the angular acceleration sensor should also be able to rotate. Very big and therefore heavy magnets inhibit this. Therefore D is taken to be 2 mm. To mount the magnets to the sensor a gap of the size of the magnets is made.

Since the channel is only 400 μm high, the electrodes used to measure the voltage are 100 μm in diameter. To minimize the influence of the electrodes on the system we use platinum, which is a very inert material. An overview of the design choices is given in Table 4.2.

Feature	Dimension (mm) / property
Channel cross section shape	rectangular
Channel cross section	3×0.4
Magnet radius	4
Magnet heigth	2
Electrode diameter	0.1
Electrode material	Platinum

TABLE 4.2: Overview of design choices.

To make sure that the channel is properly printed, the sensor is cut into a bottom part (where the channel is located) and a top part. This will also make it easier to insert the electrodes. Furthermore, since the channel is not closed in the printing process we do not need large espace holes. Afterwards, the two parts are glued to each other by UV sensitive glue. Finally, in the top part two inlets are made to connect the sensor to a flow source.

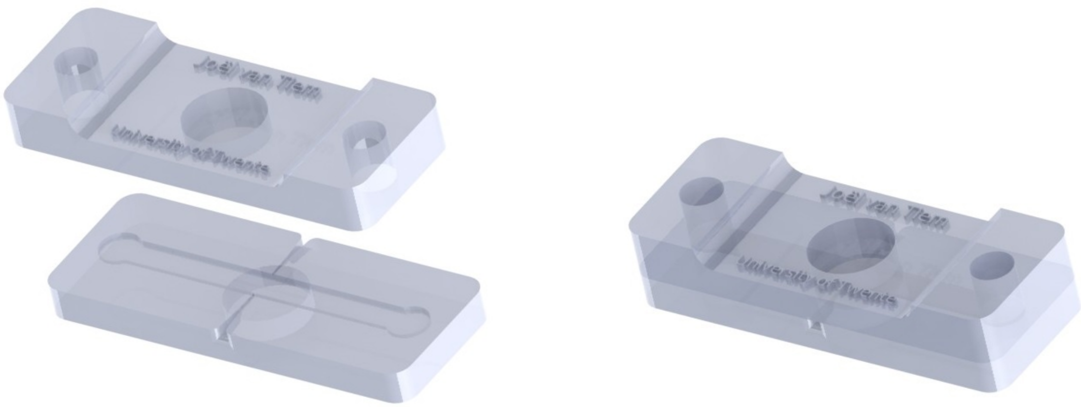

(a) The two separate parts. The channel is clearly visible in the bottom part.

(b) The assembled sensor.

FIGURE 4.6: Impression of the sensor.

4.2.2 Rectangular flow sensor V2.0

Measurements with the sensor (V1) learned that a more advanced design was required to measure the voltage properly. Therefore the sensor design has been improved so that it is also able to perform a differential measurement. Furthermore, the electrode inlets are designed to have more electrode surface in the fluid. To accommodate two pairs of magnets the sensor is also slightly longer than the V1 sensor.

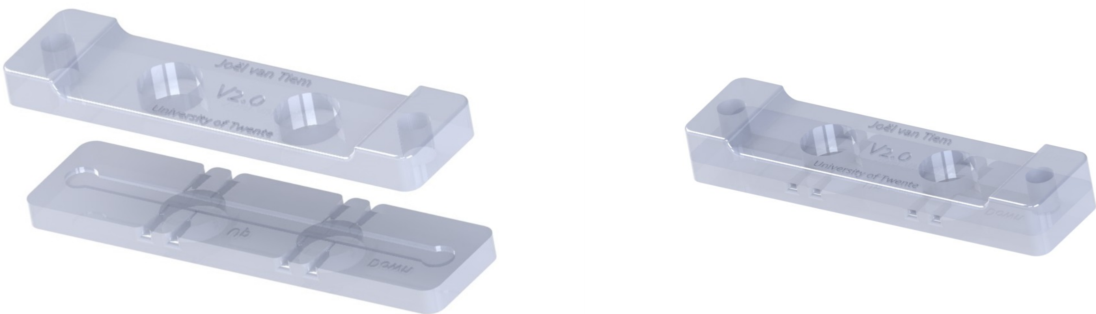

(a) The two separate parts. The channel is clearly visible in the bottom part.

(b) The assembled sensor.

FIGURE 4.7: Impression of the V2.0 sensor.

4.2.3 Angular acceleration sensor

The design choices made in the V2.0 sensor have been translated to a circular channel. The channel has the same cross sectional area of 0.4 × 3 mm. The system radius R_c (the radius of the 'torus') is 15 mm. Since this sensor is not flow but angular acceleration driven the fluid inlets are slightly different from the V2.0 one.

Furthermore, an alignment cross has been made to align the top and bottom part properly. There is space for four pairs of magnets, so that two differential measurements can be performed on one sensor. Refer to Appendix F for all specifications and a detailed technical drawing all sensors.

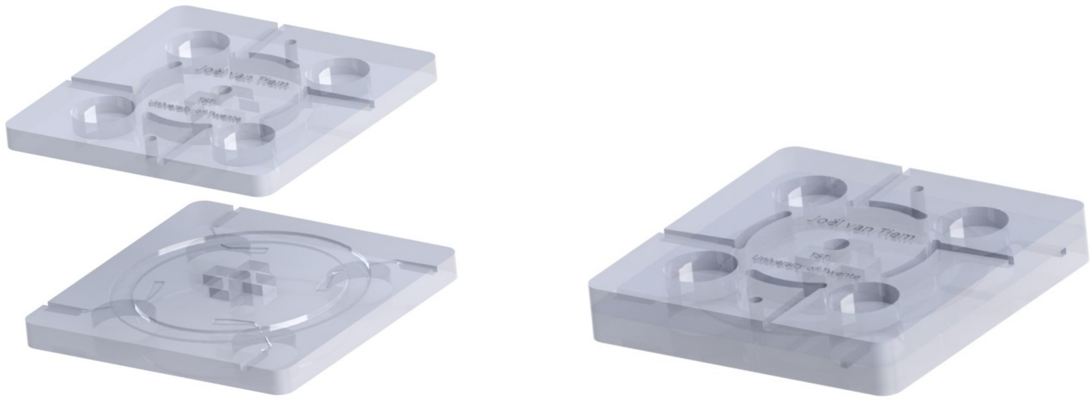

(a) The two separate parts. The channel is clearly visible in the bottom part.

(b) The assembled sensor.

FIGURE 4.8: Impression of the angular acceleration sensor.

Chapter 5

Experimental methods

5.1 Thermal readout

5.1.1 Fabrication

The chips are fabricated in the cleanroom of the MESA$^+$ Institute for Nanotechnology at the University of Twente. The fabrication process is complex and has been developed earlier in the Transducers Science and Technology group [2, 36–38]. It involves many steps and it takes a couple of months to carry out the process. A brief overview of the fabrication process is shown in the table below.

Process	Cross section and top/bottom view
	Si SiO_2 Au Cr SiRN
Silicon On Insulator (SOI) wafer. 50μm device layer, 5 μm buried silicon dioxide (BOX), 400 μm handle layer and 4.5 μm SiO_2 at the bottom	
Low pressure chemical vapor deposition (LPCVD) of silicon-rich nitride (SiRN)	

Spin resist, lithography and deep reactive ion etching (DRIE) of SiRN and SiO_2 at the backside	
DRIE of silicon at the backside to create inlets	
Chromium sputtering to be used as a hard mask during the next steps. From now on, the right sketch is the *top* view	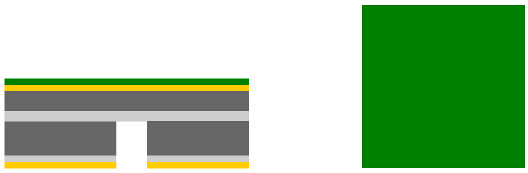
Spin photoresist, lithography and DRIE of Chromium and SiRN	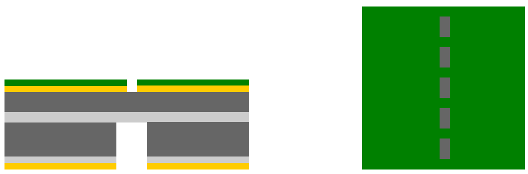
Reactive Ion Etching (RIE) of silicon to create channels	
Remove chromium and photoresist	

Etch the BOX layer using hydrogen fluoride (HF) to connect the inlets and channel

LPCVD of SiRN to close the channels

Cross section (inlet), cross section (channel) and top view

Chromium and gold sputtering for electrodes

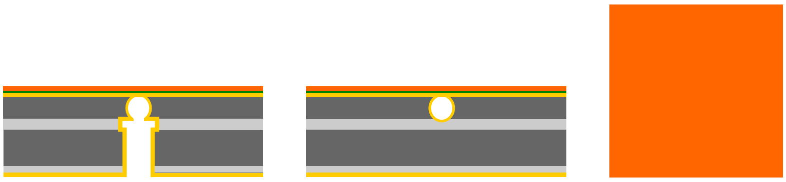

Reactive Ion Beam Etching (RIBE) of chromium and gold to create electrodes

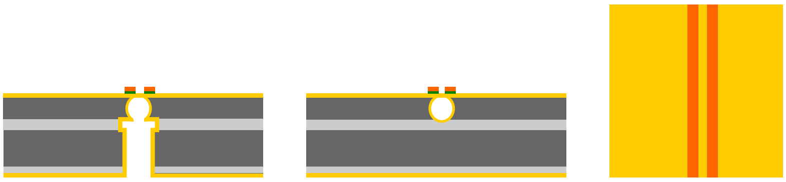

Release etch: DRIE of SiRN, RIE of silicon, vapor HF of SiO_2 and again RIE of silicon

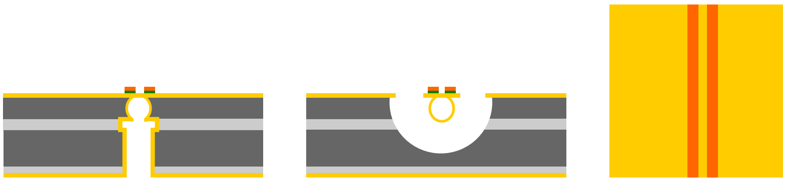

A printed circuit board has been designed to make it possible to wirebond the devices and hence connect them to the outside world.

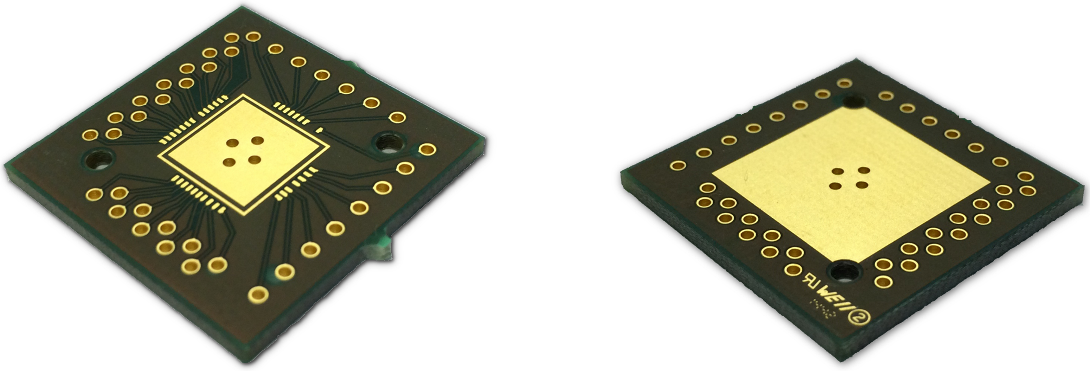

(a) Top (b) Bottom

FIGURE 5.1: The printed circuit board that the devices are mounted to. The holes in the middle allow the sensor to be filled with a liquid.

In order to fill the channels, an inlet unit has been designed. This makes it possible to connect a 'macro' sized syringe and tubing to the microchannel. The alignment with the PCB is done by two pillars on the inlet unit. These match two holes in the PCB.

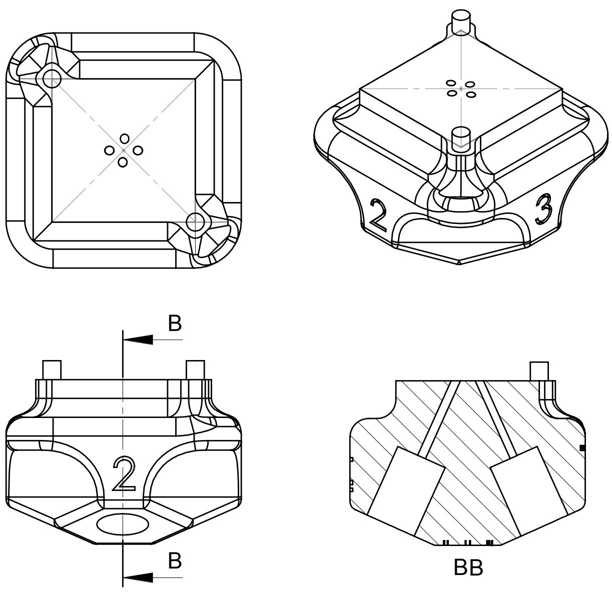

FIGURE 5.2: Impression of the inlet unit. The PCB is mounted on top of the unit. The tubing from the flow source/syringe is connected at the bottom.

A detailed illustration of the inlet is shown in Appendix F. The chip, PCB and inlet unit are connected to each other by epoxy glue.

5.1.2 Setup (flow driven)

The sensor is actuated by a syringe pump (Harvard PHD Ultra). The liquid that has left the sensor is collected in a reservoir. A basic overview of the electronic readout is giving in the figure below.

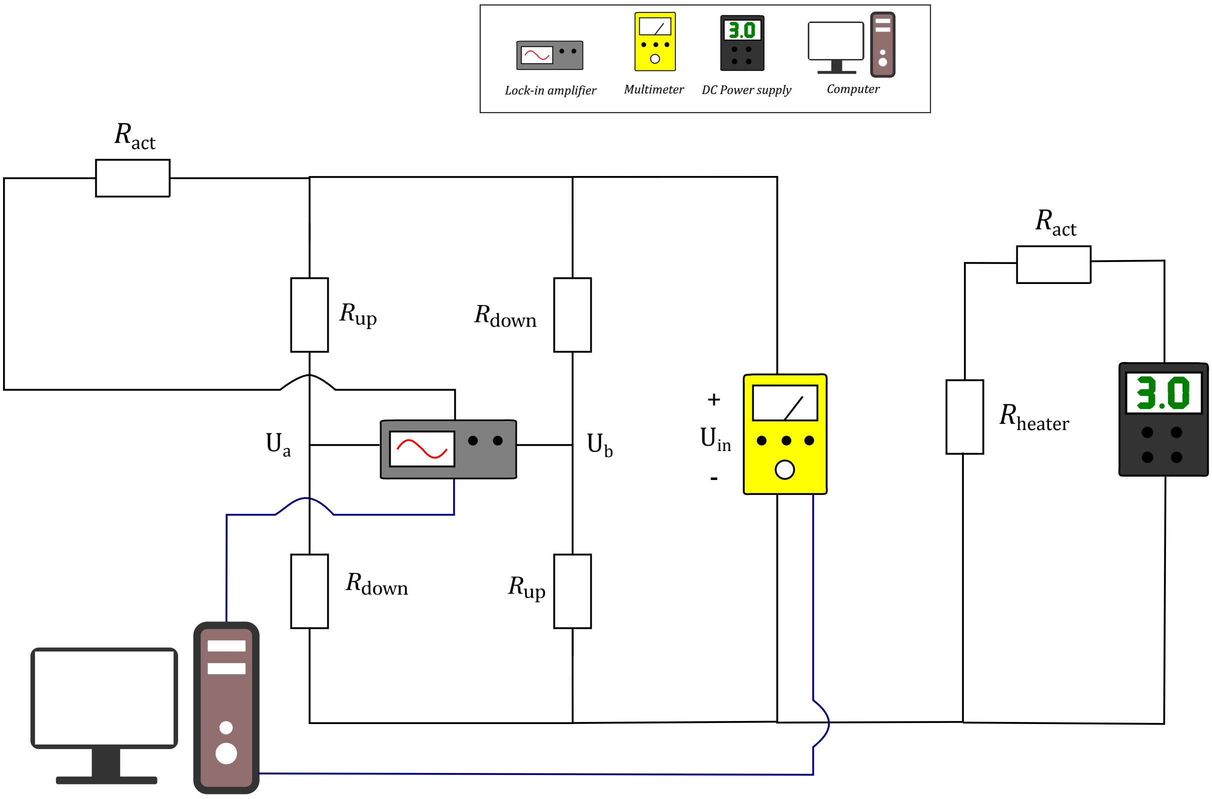

FIGURE 5.3: Basic overview of the electronics of the measurement setup.

A lock-in amplifier actuates the sensing resistors in the Wheatstone bridge configuration at a frequency of 5 kHz and an amplitude of 50 mV. To set the current trough these resistors a resistor (R_{act}) is placed in series. Recall that the change in temperature reads:

$$\frac{\Delta R}{R_0} = \frac{U_{ab}}{U_{in}} \tag{5.1}$$

U_{ab} is the voltage measured in the Wheatstone bridge. This in sensed by the same lock in amplifier and sent to a computer where the data is logged. Next, to calculate the change in temperature and therefore the flow velocity, U_{in} is measured by a multimeter which is also read by the computer.

The entire readout technique does not work without the heaters: these should also be actuated. This is done by a DC power supply unit. To control the power dissipated in the heater resistors, a resistor (R_{act}) is placed in series.

From theory we know that the sensor should act in the linear regime for flow velocities up to approximately 1 mm s^{-1}. The flow is controlled by a syringe pump. This pump has a lower limit of approximately 50 nl hr^{-1}. Therefore, the sensor is characterized for a flow ranging from 20 μm s^{-1} up to 10 mm s^{-1}. Given the channel's geometry, these flow rates translate to a volumetric flow range from 90 nl hr^{-1} to 45 μl hr^{-1}.

5.1.3 Setup (angular acceleration driven)

In order to characterize the sensor an angular acceleration has to be applied to it. To do so, the actuator of a harddisk has been used. This is actuated by a function generator so that we can set frequency. In order to determine the angular acceleration we also need to know the amplitude of the oscillation, since

$$\alpha = -\phi_0 \omega^2 = -4\pi^2 \phi_0 f^2 \tag{5.2}$$

To do so, a very flat mirror (a piece of silicon), is mounted to the moving stage. Next, we shine a laser beam on this mirror which reflects it to a screen. This makes a 'stripe' on the screen. Next, if we measure w, the width of the stripe, and we know l, the distance from the center of rotation to the screen, we can calculate ϕ_0:

$$\phi_0 = 2\arctan\left(\frac{w}{2l}\right) \tag{5.3}$$

The setup is illustrated in Figure 5.4.

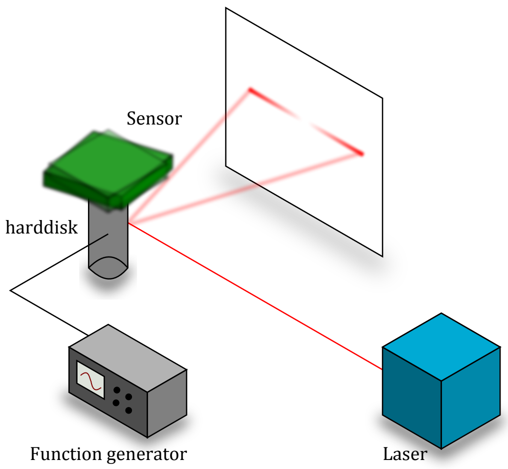

(a) Illustration of the setup.

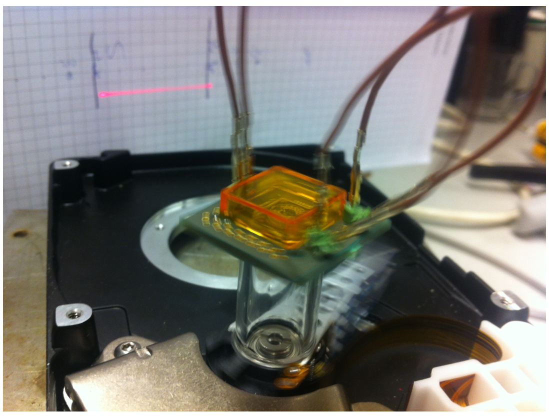

(b) The angularly accelerated sensor.

FIGURE 5.4: A harddisk actuator is used to angularly accelerate the sensor. A function generator is used to set the frequency. Using a laser beam we can determine the amplitude of oscillation, ϕ_0.

The electronic readout system is very similar to the one used in the flow driven measurement. An overview is shown in Figure 5.5.

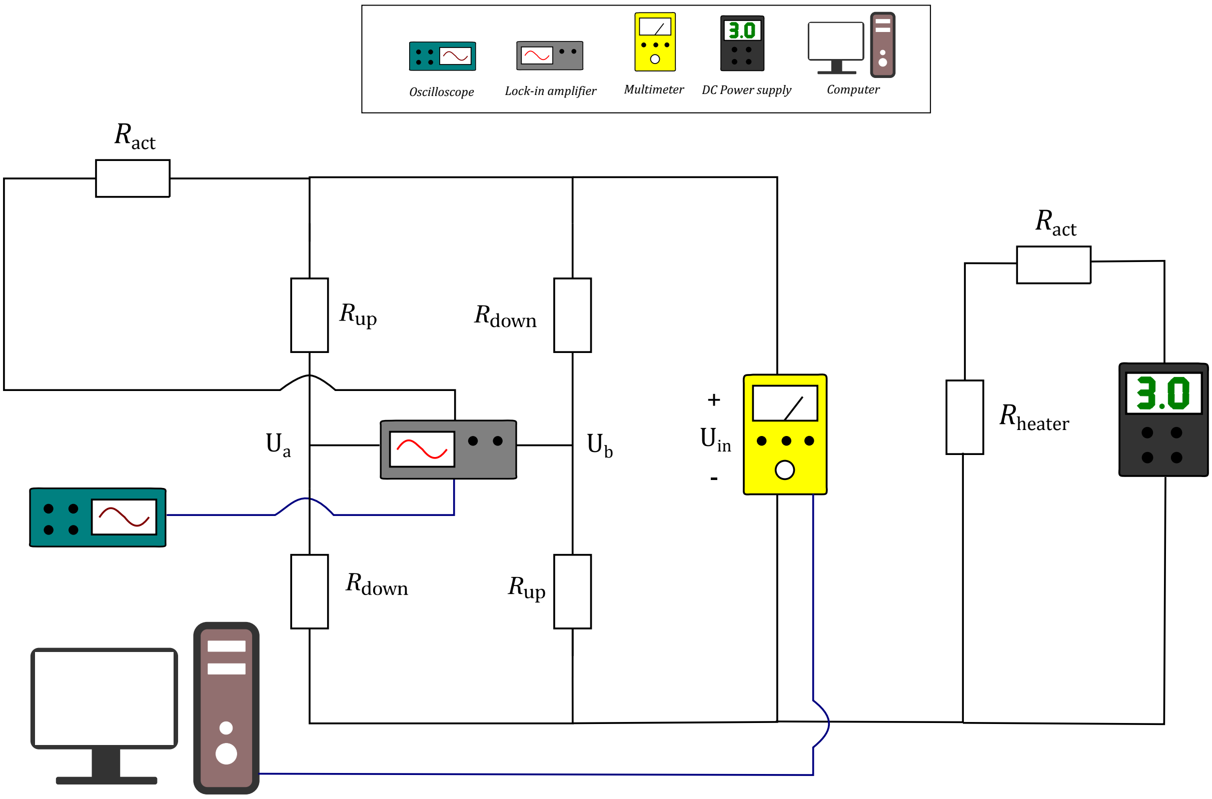

FIGURE 5.5: Basic overview of the electronics of the measurement setup.

In contrast to the flow driven measurement, the flow oscillates at the actuation frequency of the hard-disk. So the amplitude that the lock-in amplifier measures is modulated at the actuation of frequency. It is therefore read by an oscilloscope.

The same range of flow rates (20 μm s^{-1} up to 10 mm s^{-1}) are characterized in the angular acceleration sensor. Here, the flow is actuated by the angular acceleration rather than a flow source. Recall that the average flow velocity reads:

$$v_{avg} = \frac{1}{R}\int_0^R \frac{\rho R_c \alpha}{4\mu}(R^2 - r^2)\,\mathrm{d}r = -\frac{\rho R_c R^2}{6\mu}\phi_0\omega^2 \tag{5.4}$$

The density ρ and viscosity μ are the same for all sensors. ϕ_0 (the amplitude of the oscillation) and ω (corresponding angular frequency) have to be chosen to obtain v_{avg} in the desired range for given values of R and R_c.

5.2 Electromagnetic readout

5.2.1 Fabrication

The devices are 3D printed by the commercial manufacturer Shapeways. In order to realize the small feature sizes of up to 100 μm aimed at in this thesis *frosted ultra detail* is used. This plastic is a mixture of urethane acrylate polymer and triethylene glycol dimethacrylate ester.

The 3D printing process fabricates the devices by depositing layer after layer. A Multijet Modeling process is used: molten plastic is deposited on a platform after which it solidifies instantly. After one layer has been deposited it is polymerized by a UV lamp. This repeated for every layer. Next, the model is put in an oven to remove all leftover support material and is afterwards ultrasonically cleaned.

After delivery by the manufacturer the devices are again ultrasonically cleaned in isopropanol. Next, thread is tapped into the inlet holes so that tubing can be connected to the sensor. Afterwards the electrodes are mounted to the devices by UV sensitive glue. Finally, the top and bottom parts are connected to each other using the same glue.

5.2.2 Setup (flow driven)

The V1 and V2.0 sensors are characterized using a syringe pump (Harvard PHD Ultra). The syringe pump is connected to the sensor which is in turn connected to a reservoir. The magnets of 8 mm diameter and 2 mm height (Supermagnete) are mounted to the sensor. Because of their mutual attractive force there is no need to fix them. The potential difference over the channel is measured by a multimeter (HP 34401A), illustrated in the figure below.

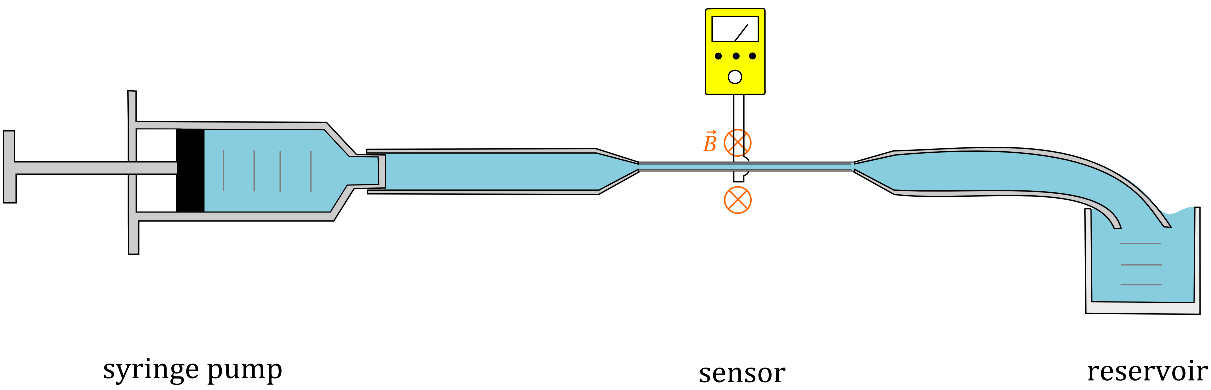

FIGURE 5.6: Basic overview of the measurement setup: the channel in the sensor is connected to a syringe pump and a reservoir.

To characterize the sensor, we have to determine the measured voltage over the channel as a function of the applied velocity. Since the syringe has a finite volume the flows cannot be chosen *too* high as the syringe will drain in a very short period of time. Therefore, unless stated otherwise, two flow programs have been used: a long and a short one.

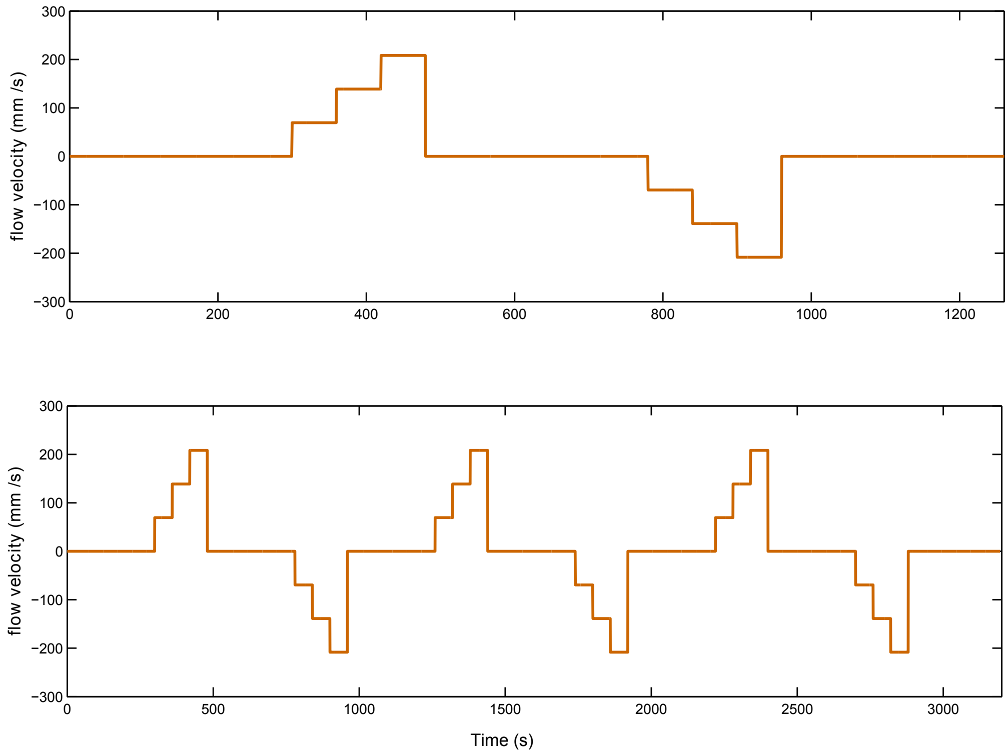

FIGURE 5.7: The basic cycle: the flow is zero for 5 minutes, it then infuses to 900 ml/hr in three steps during 3 minutes, is zero for another 5 minutes and finally withdraws in three steps from 0 to 900 ml/hr during 3 minutes. Depending on the measurement, either the long program (3 cycles, top figure) or the short program (1 cycle, bottom figure) has been used.

The flow is zero for 5 minutes to make sure the system is at a stable stable. Next, in steps of 300 ml/hr the flow increases every 60s to a value of 300 ml/hr infuse. The flow is then zero again for 5 minutes. Then, the steps repeat, but now it withdraws from 0 to 900 ml/hr. This is the basic cycle. In the long program this cycle is repeated three times, in the short one only one cycle is performed. The volumetric flowrate Q translates to the following flow velocities in the channel [1]:

Q (ml/hr)	v (mm/s)
300	69
600	139
900	208

The duration of 60s is chosen so that the syringe won't drain during a cycle. The 5 minutes in between infusing and withdrawing is chosen so that the system has time to relax and go back to a stable value. This relaxation time can be present in both the fluidical and electrical domain.

[1]Since $Q = Av$

Flow control measurement

Since a lot of measurements are performed by the syringe pump it is important to characterize it. The flow program described in the previous section is measured by a commercial Coriolis-based mass flow meter (Bronkhorst mini CORI-FLOW M14). This flow sensor is placed in between the syringe pump and the sensor.

Direct

The first measurement performed is the simplest one, the so called *direct* measurement. This comes down to to directly measuring the potential in the channel.

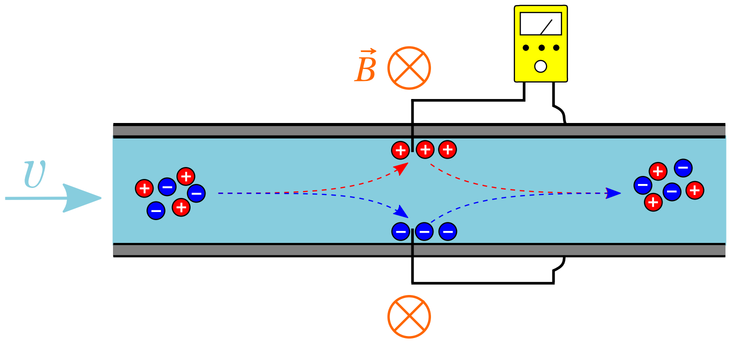

FIGURE 5.8: Illustration of the direct measurement.

Differential

It turned out that the direct measurement did not provide accurate data, so a variety of other measurements has been performed. Measuring differentially can reduce the effects of voltages induced by other sources than the magnetic field. We take two pairs of magnets and orient the magnetic field of one pair opposite to that of the other pair. Next, we connected the two electrode pairs.

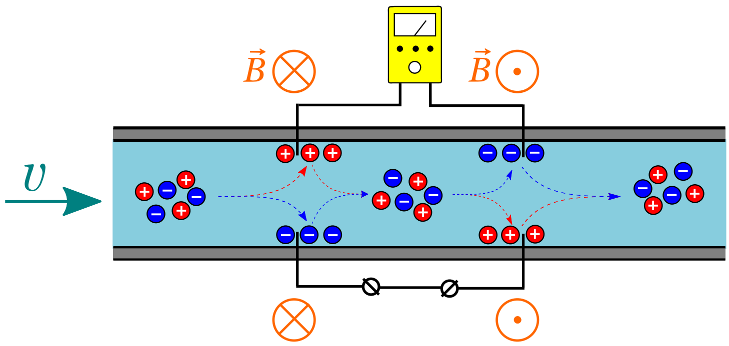

FIGURE 5.9: Illustration of the differential measurement.

The voltage we measure by the multimeter V_{sense} then reads:

$$V_{\text{sense}} = V_1 + V_2 = (V_{\text{magn}} + V_{\text{other}}) + (V_{\text{magn}} - V_{\text{other}}) = 2V_{\text{magn}} \tag{5.5}$$

Hence, in theory this measurement method should cancel voltages induced by other sources than the magnetic field an amplify the magnetically induced voltage by a factor of two.

Series resistor

To further investigate the influence of a differential measurement, a series resistor is placed in between the magnets up and magnets down region. In order to have a resistance comparable to the channel, measurements have been performed with a 1 and 10 MΩ resistor.

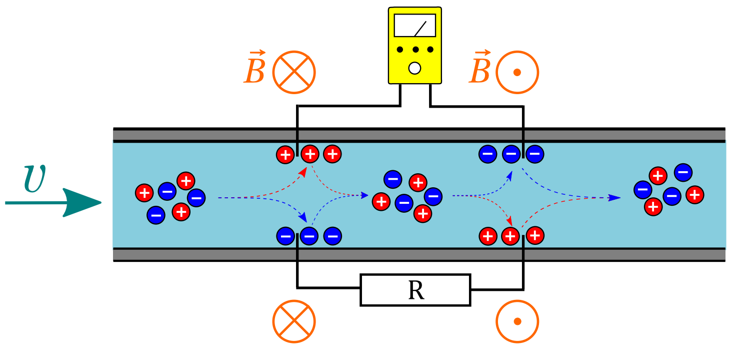

FIGURE 5.10: Illustration of the differential measurement with a resistor in series.

Diagonal and same side

To fully characterize the sensor's (DC) behavior, two more measurements have been performed: the *same side* and *diagonal* measurement. Here, the electrode geometry has been changed with respect to the direct and differential measurement.

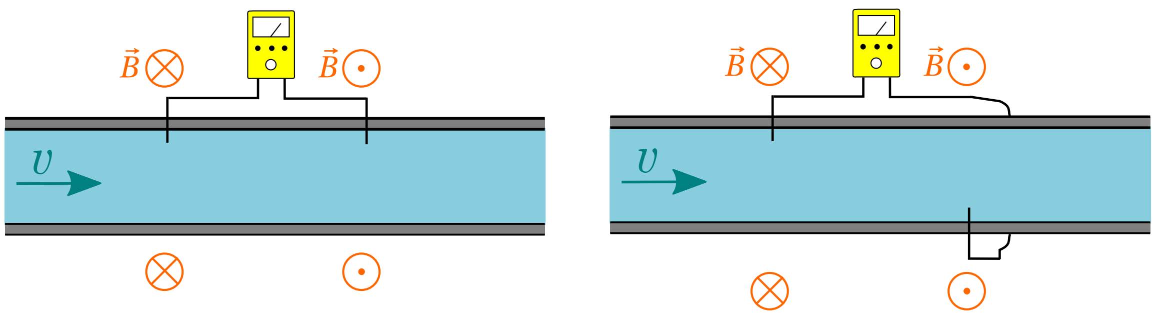

(a) Same side measurement

(b) Diagonal measurement

Alternating magnetic field

In addition to the measurement with a constant magnetic field, a measurements is performed with an alternating B. Copper wire is wrapped around a torus shaped ferrite core. This core has a small gap where the sensor is placed in. In this manner the magnetic field is focused at the channel.

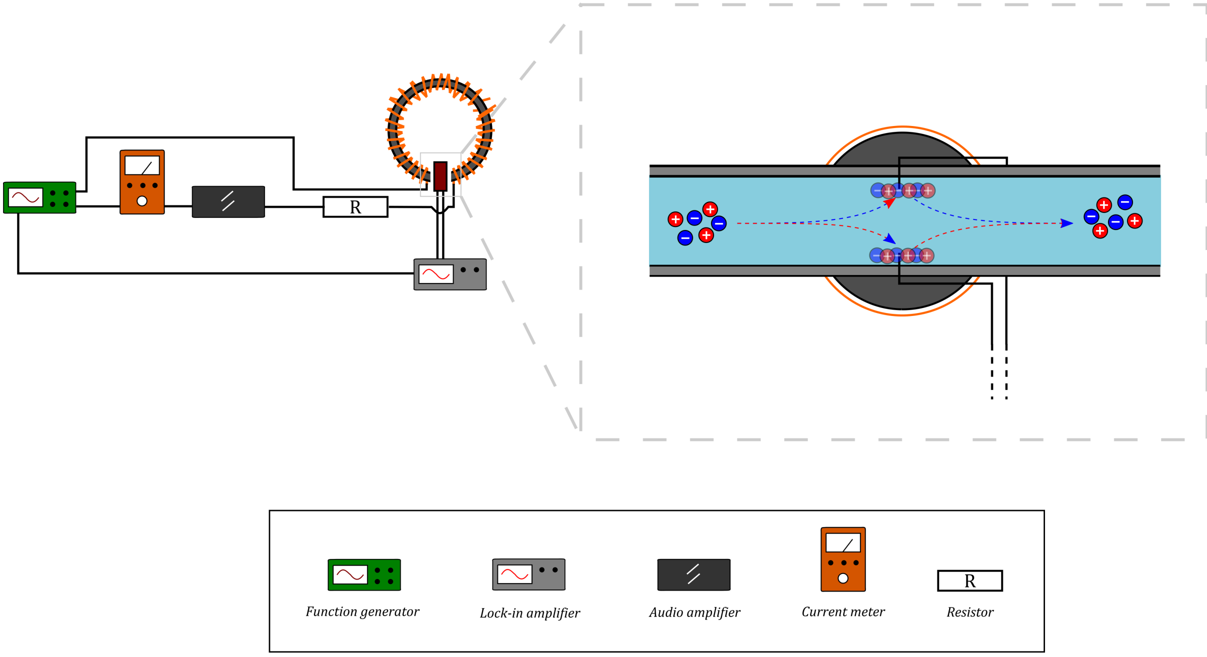

FIGURE 5.11: Overview of the setup with alternating magnetic field.

We actuate the coil with a voltage $V = V_0\Re(\exp(j\omega t))$ and put a resistor R in series. The amplitude of the magnetic flux density B_0 reads:

$$B_0 = \mu\frac{N}{L}|i| \tag{5.6}$$

$$= \mu\frac{N}{L}\left|\frac{V_0}{j\omega L + R}\right| \tag{5.7}$$

The actuation signal V is generated by a function generator (Agilent 33120A Arbitrary Waveform Generator). The higher the frequency, the higher impedance. Therefore, for a given value of V_0, the current and therefore magnetic flux density will decrease for increasing ω. An audio amplifier is used to provide enough current.

Since we now have a reference frequency (the frequency at which the magnetic field is oscillating) we can use a lock-in amplifier to measure the potential in the channel. The lock-in amplifier is able to filter and amplify with a very narrow bandwidth around the actuation frequency.

5.2.3 Setup (angular acceleration driven)

To characterize the angular acceleration sensor, the same setup as for the thermal readout sensor is used. The only difference is that the maximum angular acceleration we can obtain is somewhat lower for the 3D printed sensor, since it is a lot heavier than the micromachined sensor. The harddisk has a mechanical transfer function and a resonance frequency. Since the latter decreases with increasing mass, the amplitude of oscillation starts to drop at a lower frequency. Therefore, the maximum value of the angular acceleration we can generate is limited.

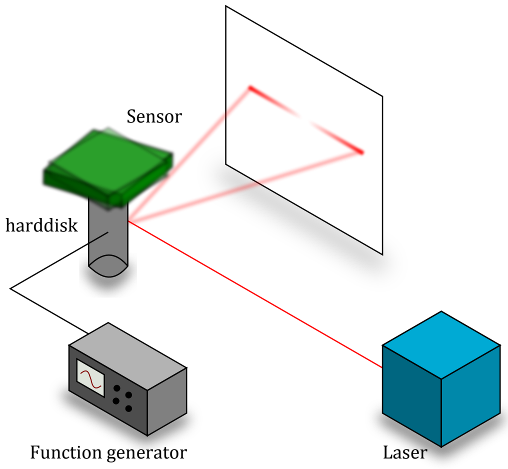

(a) Illustration of the setup.

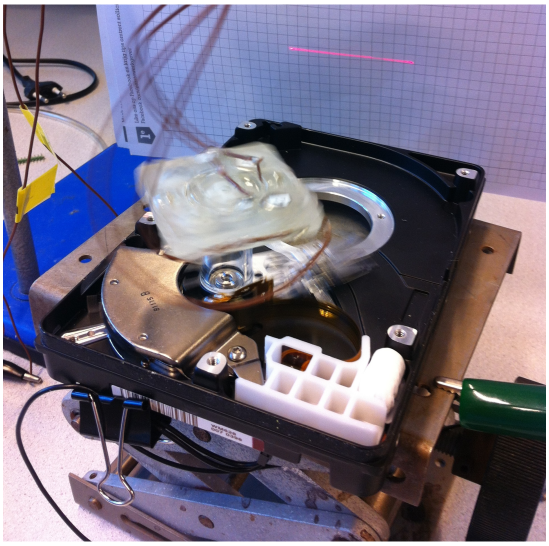

(b) The angularly accelerated sensor.

FIGURE 5.12: The same setup as for the thermal readout sensors is used.

Chapter 6

Results and discussion

6.1 Thermal readout

6.1.1 Fabrication

The devices have been fabricated. Every sample has been inspected and photographed by a light sensitive camera. For reference, the mask is shown at the right of each photograph.

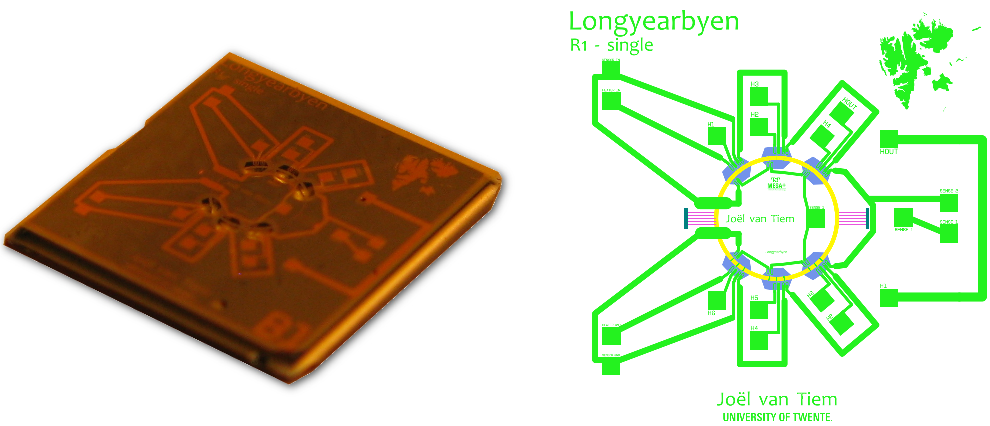

Longearbyen. $R_c = 1$mm, single slits.

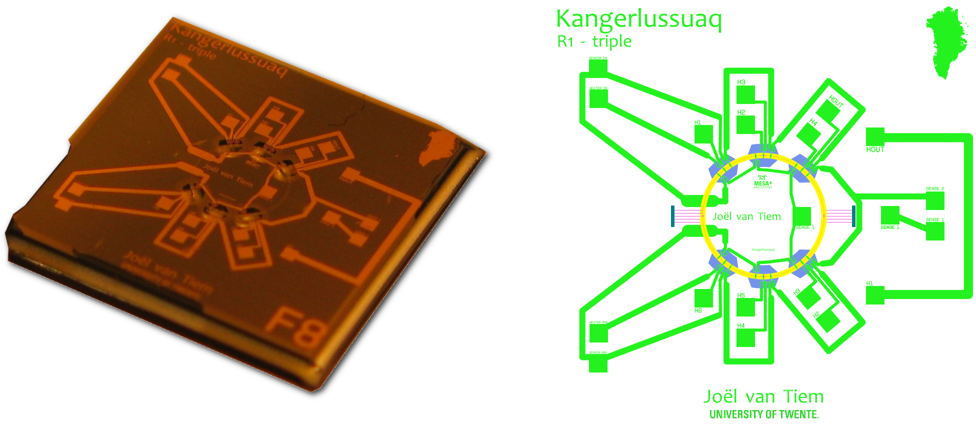

Kangerlussuaq. $R_c = 1$mm, triple slits.

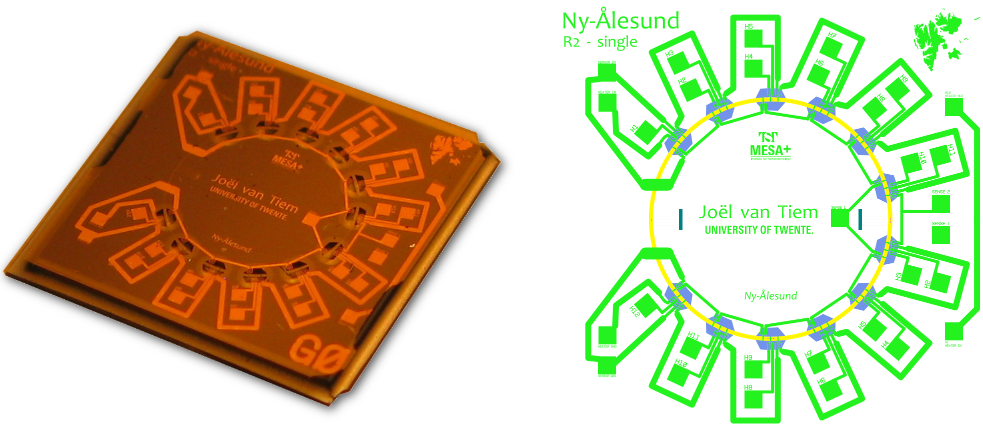

Ny-Ålesund. $R_c = 2$mm, single slits.

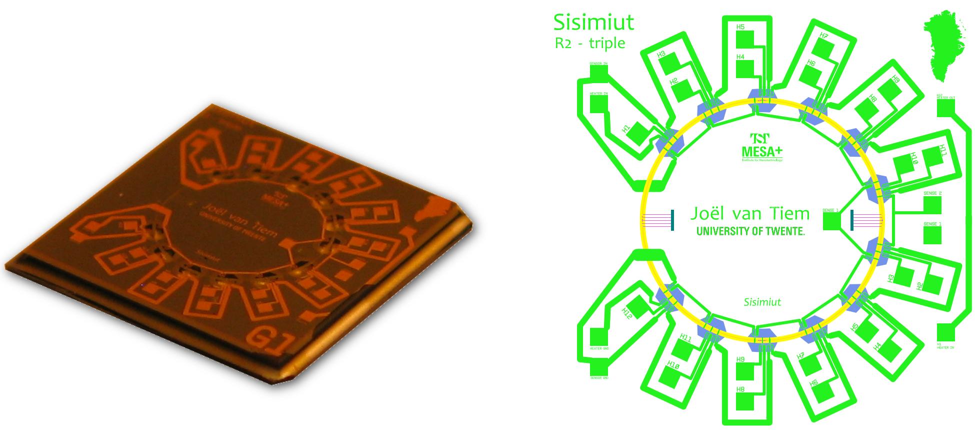

Sisimiut. $R_c = 2$mm, triple slits.

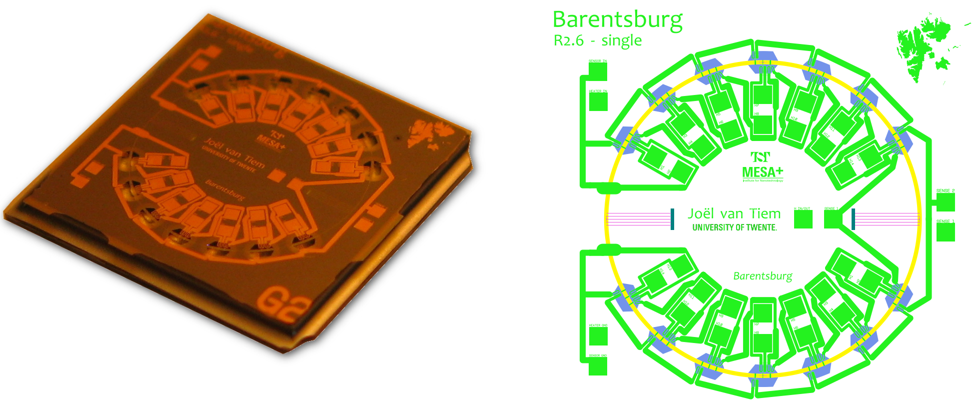

Barentsburg. $R_c = 2.6$mm, single slits.

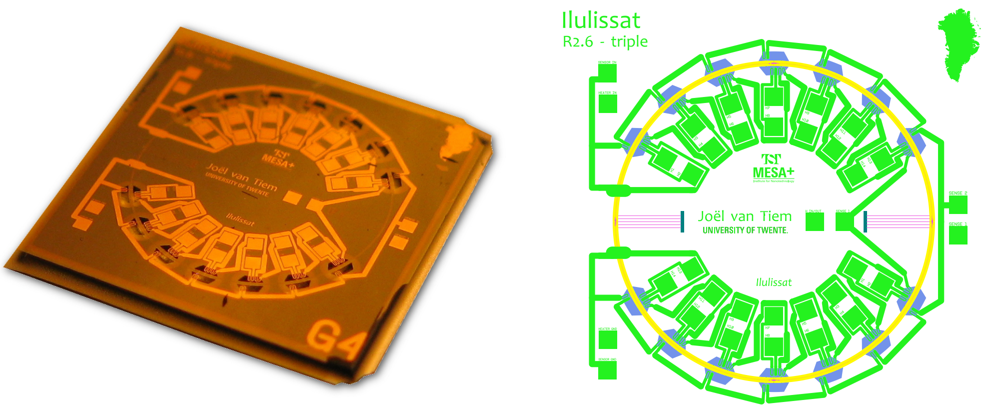

Illulisat. $R_c = 2.6$mm, triple slits.

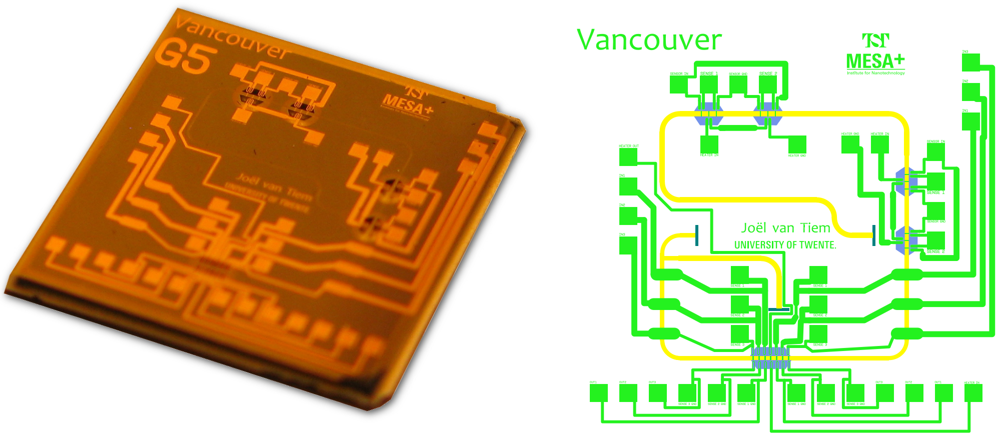

Vancouver, both single and triple slits

FIGURE 6.1: Overview of the fabricated chip. The yellow glow is caused by the light used to make the photos.

The heater geometry and channel are inspected by optical microscopy (Polytec MSA-400). The release was successful for the chips with R_c equal to 2 or 2.6 mm (Sisimiut, Illulisat, Ny-Ålesund and Barentsburg). For the chips with smaller R_c (Kangerlussuaq and Longyearbyen) the sensing configurations are closer to each other and the under etch has been two big: there is no region in between two heating configurations where the channel is buried in the silicon.

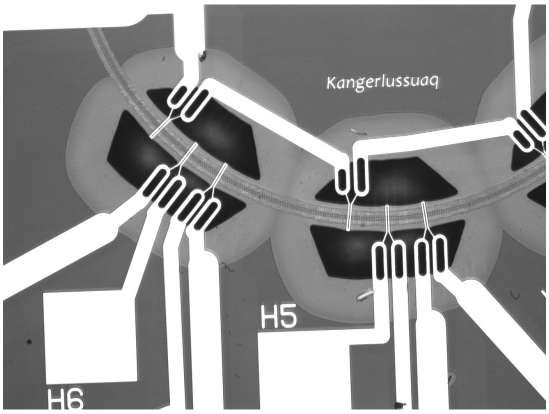

(a) Kangerlussuaq (R_c = 1mm)

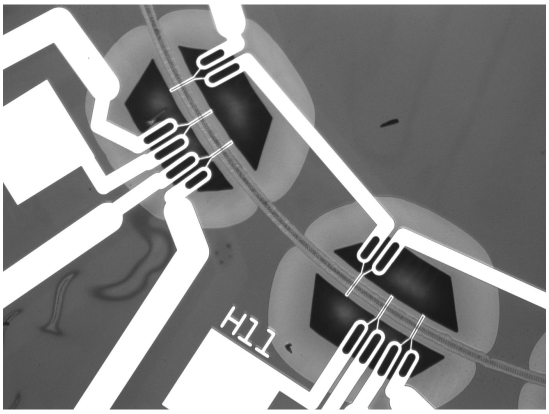

(b) Sisimiut (R_c = 2mm)

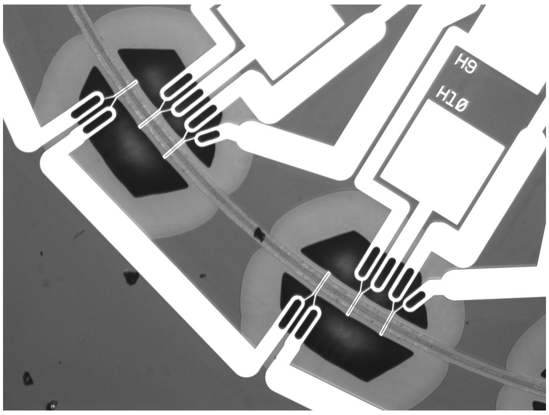

(c) Illulisat (R_c = 2.6mm)

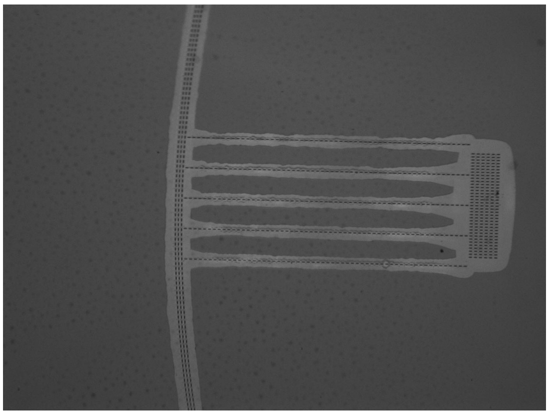

(d) Inlets of Kangerlussuaq

FIGURE 6.2: Overview of the heater geometry for the three-slit type sensors. For the smallest value of R_c (Kangerlussuaq), the underetch is too big so that the channel is not buried in silicon in between two sensing configurations. The bottom right figure shows a channel inlet.

To obtain even more detail, a scanning electron microscope (FEI Quanta 450) has been used to make images of the sensor.

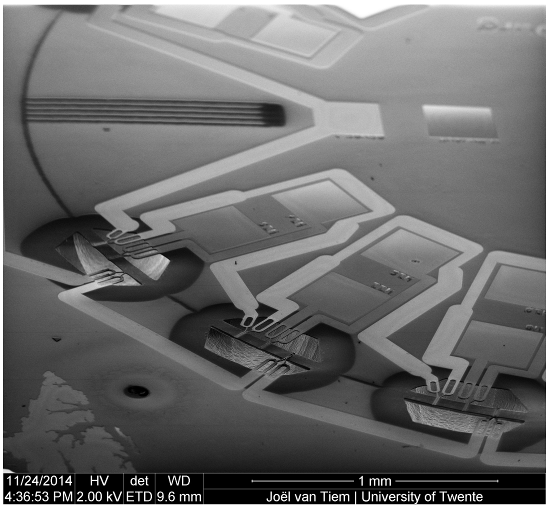

(a) Three thermal readout configurations. At the top of the inlet is visible.

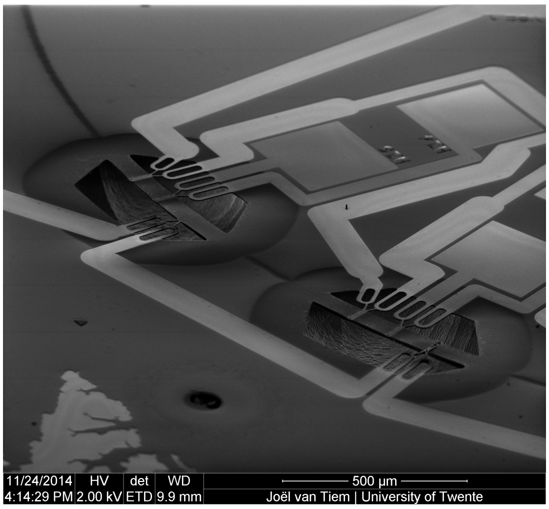

(b) Two thermal readout configurations. The underetch (the dark ring around the sensors) is clearly visibly.

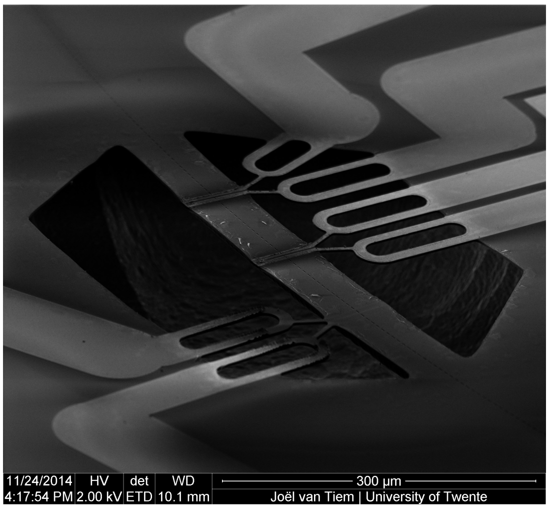

(c) Closeup of one thermal readout configuration. The released silicon is clearly visible.

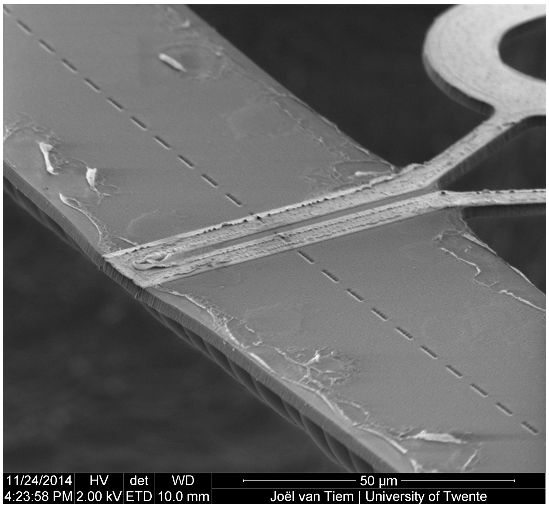

(d) Closeup of the channel and the heater electrode.

FIGURE 6.3: Overview of the *Barentsburg* chip and closeups of the thermal readout geometry and heater element.

After inspection the sensor has been packaged and mounted to the PCB and inlet unit, as shown in Figure 6.4.

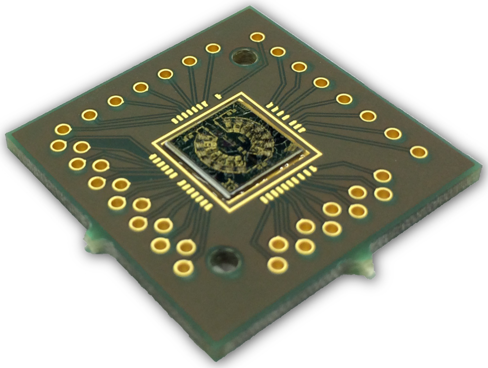

(a) The sensor mounted to the PCB.

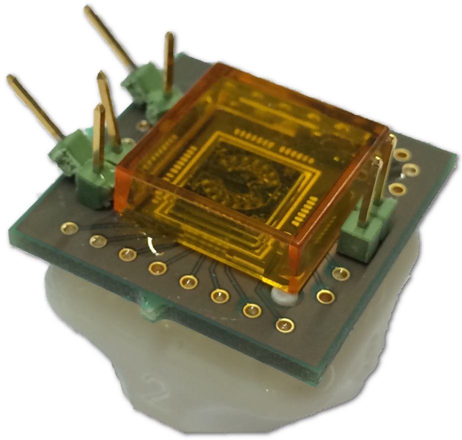

(b) The PCB mounted to the inlet unit. A cover is put over the sensor to protect it against dust.

FIGURE 6.4: The packaged sensor.

6.1.2 Measurement results

In view of the time available for the characterization, only two sensors have been characterized: Vancouver and Barentsburg. These two sensors are chosen because they are a flow - and angular acceleration driven device. Furthermore, Barentsburg has the highest system radius R_c. This means that for a given angular acceleration, it has a higher flow velocity and therefore signal than the chips with a smaller R_c.

Flow driven

The resistance of the sensor configuration was measured to be 23.1 Ω whereas the heaters have a resistance of 72.6 Ω. The latter resistance is higher because the heater configurations are connected to each other by bondwires, whereas the sensor configurations are connected through the gold layer.. The heater resistors were connected to a power supply of 5.7 V (EA-PS 2016-050) with a 1504.2 Ω resistor in series. The power supplied to the heater P reads:

$$P = i_{\text{heater}}^2 R_{\text{heater}} \tag{6.1}$$

$$= U_{\text{total}}^2 \frac{R_{\text{heater}}}{R_{\text{total}}^2} \tag{6.2}$$

$$= 5.8^2 \frac{72.6}{1576.8^2} = 0.98 \text{ mW} \tag{6.3}$$

No difference in signal was observed between the flow turned on and off. In addition, the signal also remained the same for a flow of water and and a flow of air. Hence the measured signal was observed not to depend on the applied flow velocity.

Angular acceleration driven

The resistance of the sensor configuration was measured to be 148.6 Ω whereas the heaters have a resistance of 282 Ω. The resistances are much higher than in the Vancouver chip, since here 7 heater and sensor configurations are connected to each other whereas Vancouver only comprises one. The heater resistors were connected to a power supply of 3.5 V (EA-PS 2016-050) with a 1502.2 Ω resistor in series. The power supplied to the heater P reads:

$$\begin{aligned} P &= i_{\text{heater}}^2 R_{\text{heater}} && (6.4)\\ &= U_{\text{total}}^2 \frac{R_{\text{heater}}}{R_{\text{total}}^2} && (6.5)\\ &= 3.5^2 \frac{282}{1784.2^2} = 1.09 \text{ mW} && (6.6) \end{aligned}$$

The sensor was actuated from 0 to 30 Hz in steps of 2 Hz, which corresponds to an angular acceleration of 0 to $9.9 \cdot 10^4$ s^{-2} with steps of 331 s^{-2}. In this regime, the boundary layer is sufficiently large to use the quasistatic solution for the flow profile.

Similar to the flow driven measurement, no difference in signal was observed between the angular acceleration turned on and off. Hence the measured signal was observed not to depend on the applied angular acceleration.

6.1.3 Discussion

A variety of issues can cause the sensors to malfunction. Of course it is possible that something has gone wrong during fabrication. However, visual inspections of the sensors used in the characterization show no anomalies. Furthermore, devices from the same fabrication run have proven to function. So this is unlikely to be the cause.

Then, something might have gone wrong during the initial assembly. A bondwire can be loose or a connection could have been broken. A quick resistor check shows that this is not the case since everything that should be connected electronically is also connected.

Then the most plausible explanation remains: there is no fluid in the channel. This could be caused by something that has gone wrong during the final assembly, i.e. gluing the chip to the PCB and the PCB to the inlet unit. This step is very susceptible to (human) errors. There are basically two processes that can go wrong: the alignment and the gluing itself.

The alignment of the PCB to the inlet unit is not very critical, since it has got alignment marks. The margin of these marks is 100 μm and the diameter of the holes in the inlet unit and PCB are 900 μm. The alignment of the chip to the PCB is more critical, since this has to be done by visual inspection. If the inlets from the chip do not align with holes in the PCB there will be no fluidic connection. The chip can be pushed around a bit afterwards, but then there will be glue in the chip inlet. It is easy to see whether the inlets are aligned to the PCB holes since the channel is translucent. However, the glue is also translucent which inhibits a simple check whether the inlets are clogged or not.

The gluing process itself is also critical. The chip and PCB are very flat and the glue does not spread out a lot so they are relatively easy to glue together. This is not the case for the PCB and the inlet unit since the latter has a very high roughness. Three situations can be distinguished.

1. Both the PCB and chip and PCB and inlet unit have been glued properly. The fluid can flow only from the inlet to the outlet through the channel.

2. Either the in- or outlet from the inlet unit or the channel has been clogged by glue which inhibits the flow from entering the channel.

3. There is an other fluidic connection from the inlet to the outlet apart from the channel, because the glue did not cover the entire cross section. This acts as a parallel (hydraulic) resistance that reduces the flow rate in the channel itself. The greater the gap, the more fluid will will flow through it than through the channel. Because of the small channel diameter a 'small' gap in macroscopic terms can quickly lead to a significant drop in the flow velocity in the channel. Applying more flow will only increase the pressure over this gap which might expand it.

These situations are illustrated in the figure below.

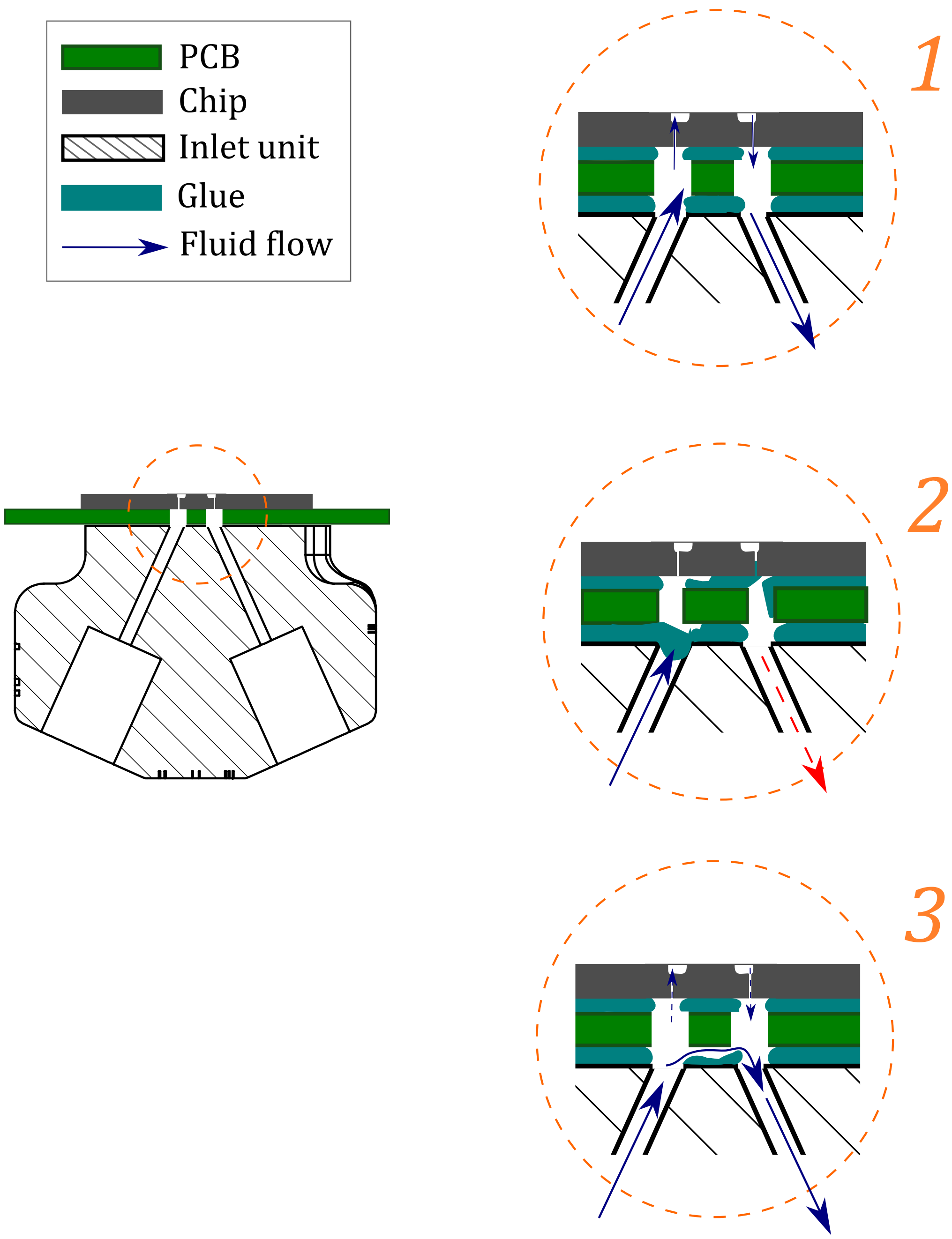

FIGURE 6.5: Overview of the three possible gluing situations. The gluing process has been performed correctly and the flow will go from the inlet, through the channel, to the outlet (1). One of the holes has been clogged so that no flow can reach the channel (2). There is, apart from the channel itself, an other fluidic connection from the inlet to the outlet (3).

The inlets have been inspected by a microscope (Polytec MSA-400). Figure 6.6 shows three different outcomes of the gluing process. The rectangularly shaped inlet is located on the chip, whereas the circle around it is the hole in the PCB.

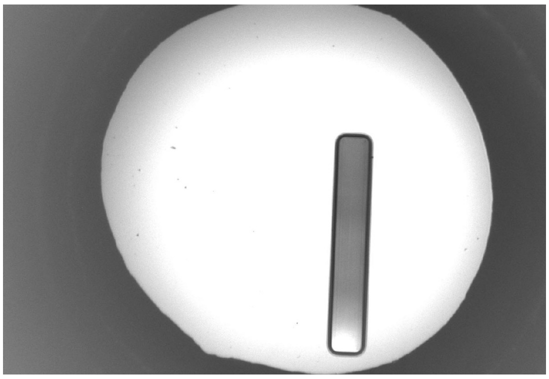

(a) Correct gluing process: there is no glue near the inlet. However, we do not know if there is a gap in the glue to the outlet.

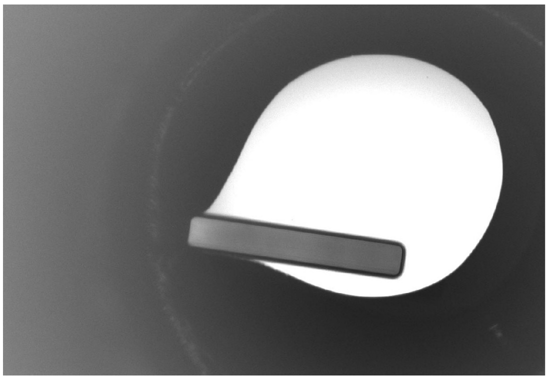

(b) This figure makes it plausible that there is no glue in the inlet and it is surrounded by glue. We still, however, do not know for sure if there is a gap to the outlet.

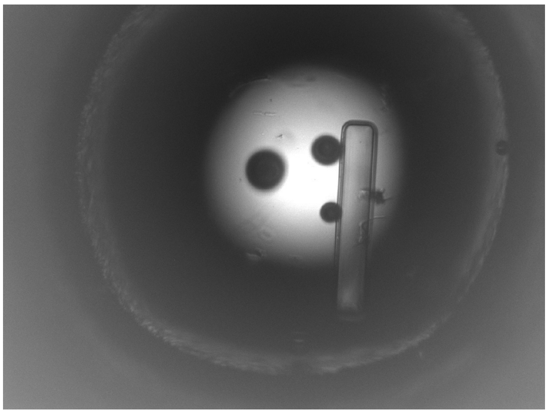

(c) Failed gluing process: the glue covers the entire inlet.

FIGURE 6.6: Multiple outcomes of the gluing process of the chip to the PCB. The rectangularly shaped inlet of the chip is 350 × 50 μm.

To prevent situation 2 from happening, apart from epoxy glue, also double sided tape has been used to connect the PCB to the inlet unit. Since now the glue cannot flow it cannot clog the inlets. So the problem in situation 2 has been solved, but situation 3 can still occur. It is even more likely to occurs, since the tape has a uniform thickness and the glue does not flow. Therefore, it cannot overcome the roughness of the inlet unit and it is likely that gaps arise. Since the inlet unit is not translucent it is hard to see if the process has been performed correctly. If it has not gone correctly, the tape has to stripped. This stripping process can also cause the inlets to clog, as shown in Figure 6.7.

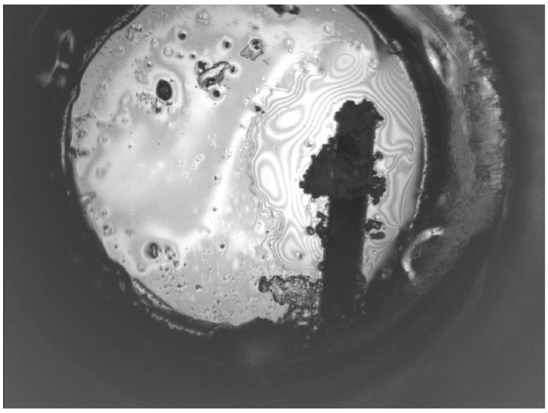

FIGURE 6.7: Inlet after removal of the tape.

A possible technique to also resolve situation 3 is applying a thin film of glue to the inlet unit using a roller. This will create a uniform thin layer of glue. Because it is so thin it will not go into the inlets. The most suitable glue to do this is UV glue. However, since the inlet unit is not very translucent it has to be exposed to UV light for a relatively long period of time. Since the inlet unit itself is also UV sensitive, this solution is not very suitable. The glue used before, epoxy, is too thick to obtain a thin film of glue and will therefore probably go into the inlets and hence clog them.

The best solution lies in a new inlet design. First of all, the inlets could be spaced further away so that there is more surface in between them. This allows for better gluing and easier handling. Furthermore, the inlet unit could expanded by extensions at the holes.

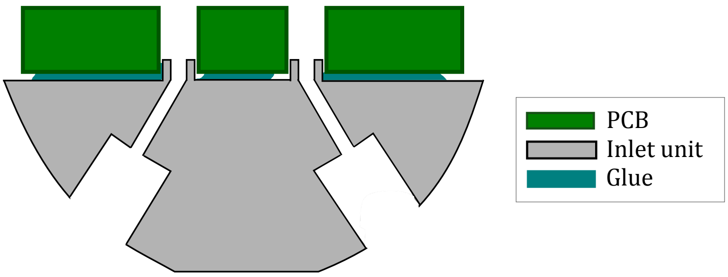

FIGURE 6.8: Proposed inlet unit design.

These extensions prevent glue from going into the channel and automatically serve as an alignment mark. These extensions are not possible to integrate in the current inlet unit design as the chip inlets are too close together; the 3D printer resolution is not high enough.

Because of time restrictions this design improvement has not been used in this report.

6.2 Electromagnetic readout

This section solely describes the measurement results and observations. A thorough discussion of the results is performed in subsection 6.2.4.

6.2.1 Fabrication

The devices have been fabricated and assembled.

(a) The V1 sensor.

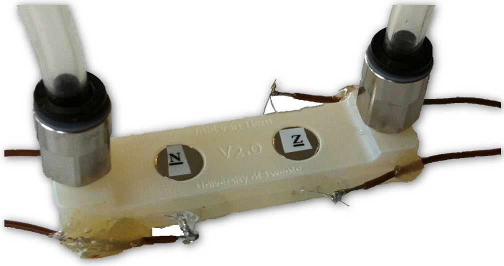

(b) The V2.0 sensor.

(c) The sensor used for AC magnetic field measurements

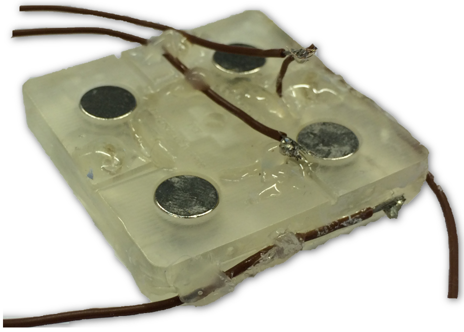

(d) The angular acceleration sensor with two sets of electrodes connected.

FIGURE 6.9: The fabricated and assembled sensors.

6.2.2 Measurement results (flow driven)

In all measurements performed in this section either tapwater, de-ionized water or salt water has been used. The table below gives an overview of the corresponding conductivities.

	conductivity (μS cm^{-1})
DI water	11
tap water	450
salt water	2900

Flow control measurement

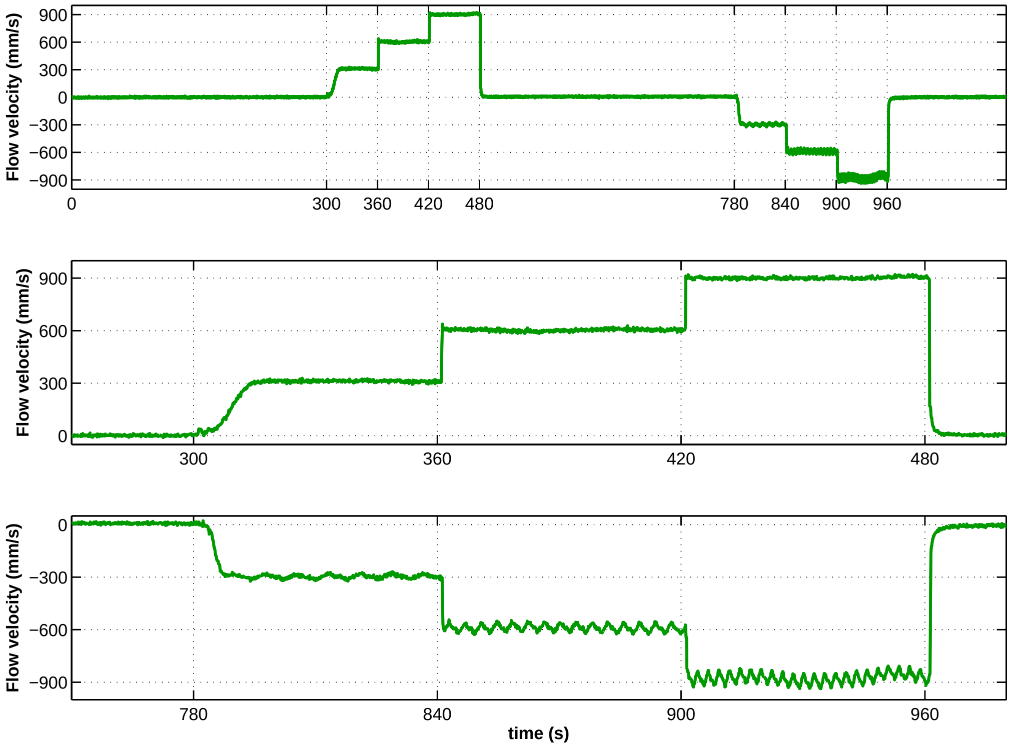

FIGURE 6.10: The results of the flow control measurement. Top: the total cycle. Middle: close up for infusing. Bottom: closeup for withdrawing.

The flow velocity is more or less symmetrical for withdrawing and infusing. The step in the flow program translates to a step in the actual flow: no strong relaxation effects are visible. The fluidic RC-time is smaller than a few seconds. There is, however, a setting effect when the flow goes from zero to ± 300 mm s^{-1}. This is most probably not caused by the fluidic RC network, but by the slips-stick effect of the plunger in the syringe. This effect is not present when the flow goes from e.g. 300 to 600 ± 300 mm s^{-1} since then the plunger is already moving.

Oscillations in the flow velocity are visible when the pump in withdrawing. Both the amplitude and frequency of these oscillations increase with decreasing (more negative) flow rate. They are caused by the worm drive in the syringe pump.

So in analyzing the results the other measurements we should keep in mind that, for some values of time, the actual flow is different from the set flow program.

Direct

The results of the direct measurement are plotted below. The top figure indicates the measured voltage for the sensor with magnets up, down and without magnets. The bottom figure shows the difference between the voltage measured with magnets up and the one with magnets down.

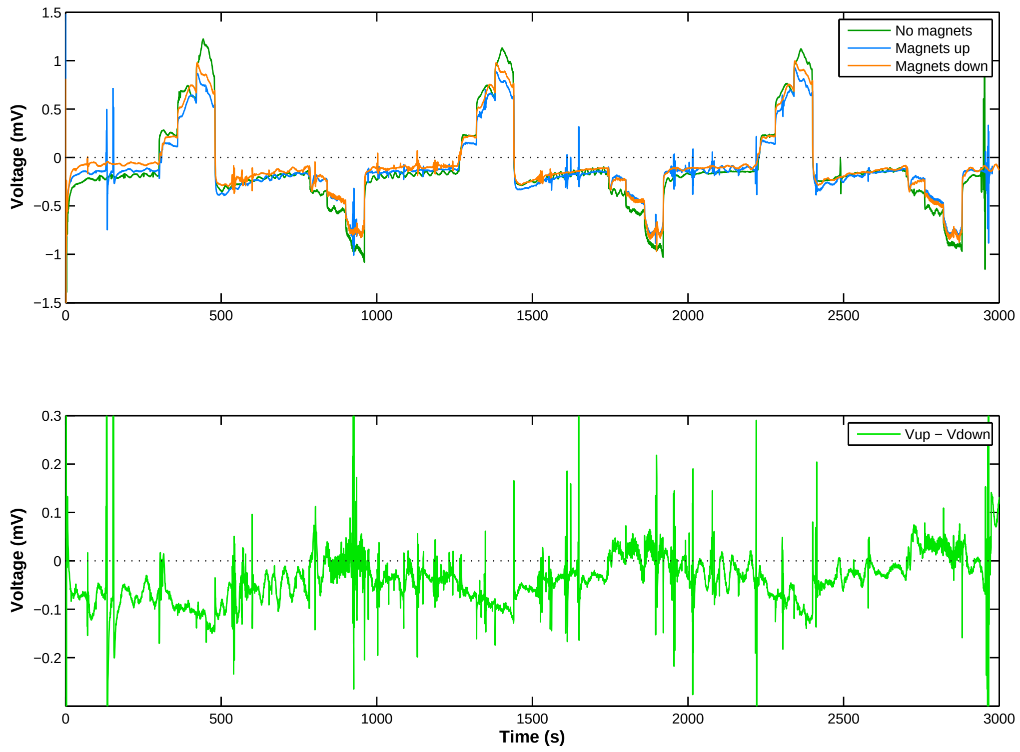

FIGURE 6.11: The results of the measurement of the V1 sensor with tap water. Top: measured voltage for no magnets, magnets up and magnets down. Bottom: the difference between the voltage measured with magnets up, and the one with magnets down.

It can be observed that the signal is flow and direction depended: there is a clear correlation between the measured voltage and the applied flow. We also see a (small) difference between magnets up, down and no magnets. Furthermore, an offset voltage for zero flow can be seen. The step in flow is not directly translated into a step in voltage, but a gradually increasing voltage when the flow drops to zero is observed. The peaks in voltage are not constant over time and there is a difference in magnitude for a positive (infusing) flow and a negative (withdrawing) one.

Differential

Analogous to the direct measurement, the figure below shows the results for the differential measurement.

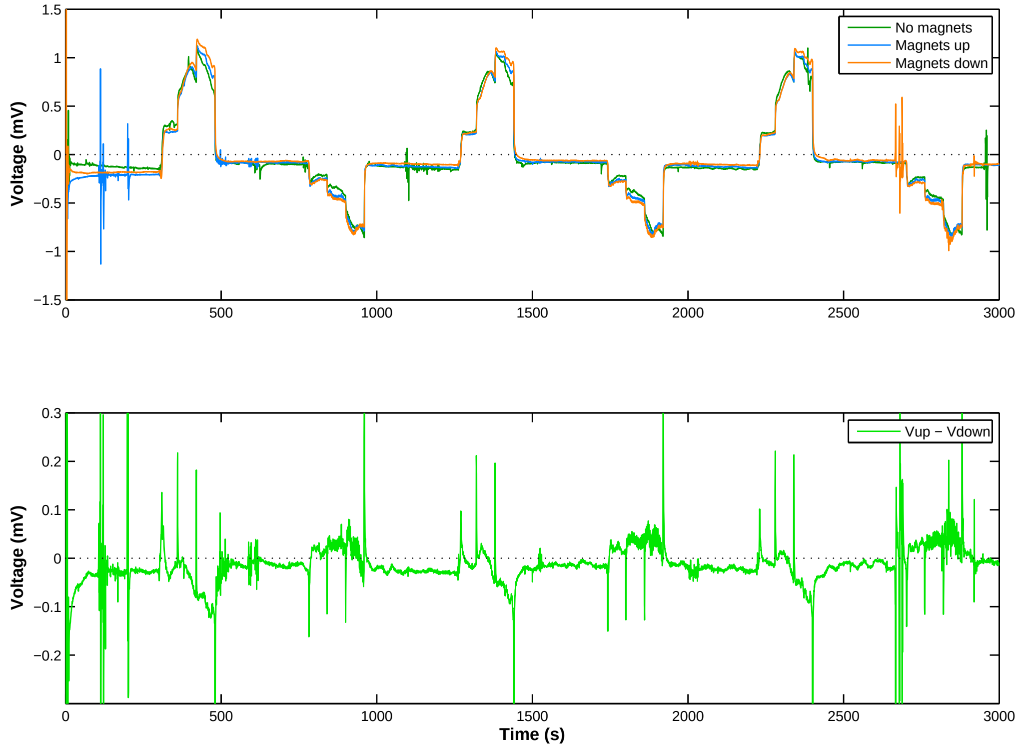

FIGURE 6.12: The results of the differential measurement of the V2.0 sensor with tap water. Top: measured voltage for no magnets, magnets up and magnets down. Bottom: the difference between the voltage measured with magnets up, and the one with magnets down.

Similar to the direct measurement, the offset is present in this data. The difference between magnets up and down and no magnets is smaller than for the direct measurement, as well as the noise. The relaxation effect is hardly visible: when the flow drops to zero the voltage follows almost instantaneously. The peaks are not constant over time and there is still a difference between the magnitude of the signal for infusing and withdrawing.

Resistors in series

Figure 6.13 shows the results for the differential measurement with a 1 MΩ and a 10 MΩ resistor in series. This measurement has been performed without magnets. The top plot shows the measured data. In order to compare the results properly, the bottom plot shows a normalized signal, i.e. the offset has been set to zero.

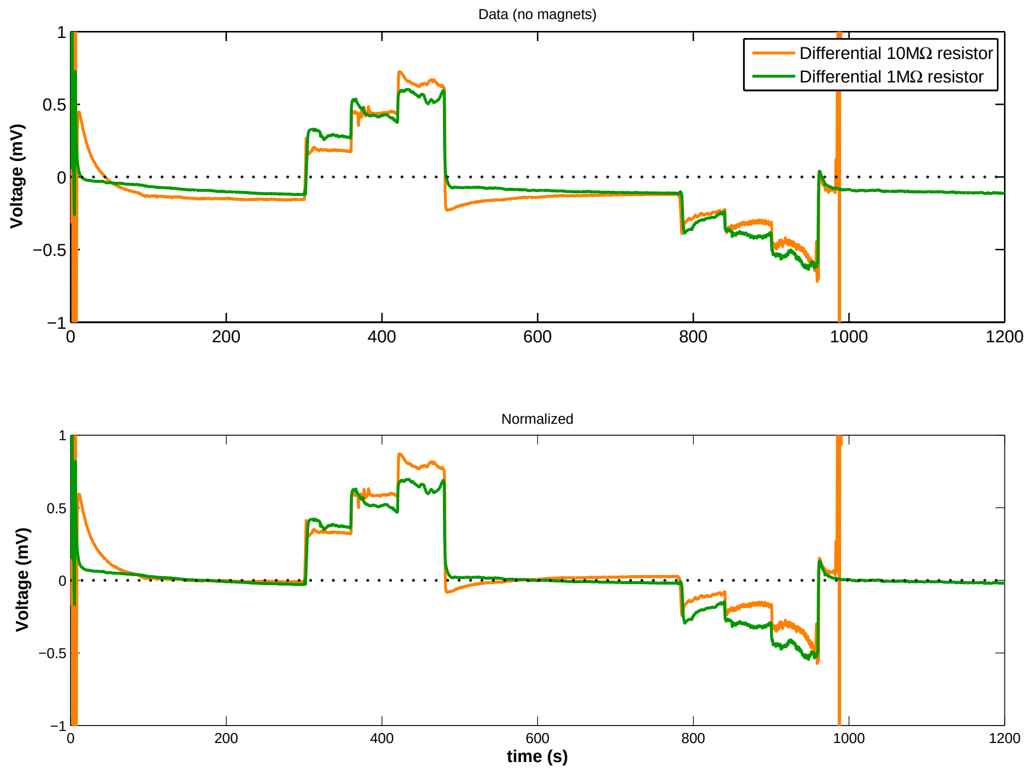

FIGURE 6.13: Measured voltage for a 1 MΩ and 10 MΩ resistor differential measurement. Top: data, bottom: normalized data.

A difference between the 1 and 10 MΩ can ;be observed. The difference is, however, not consistent: for some values of time the signal for 1 MΩ is greater than the 10 MΩ one, whereas for other times the opposite is true.

Diagonal and same side

Figure 6.14 shows the measurement data for the same side measurement (top) and diagonal (middle). These two measurements have been performed with magnets up, down and without magnets. The bottom graph shows the diagonal measurement *without* magnets for three different fluid conductivities. Note that in these measurements the 'short' flow profile is used, i.e. one cycle of infusing and withdrawing.

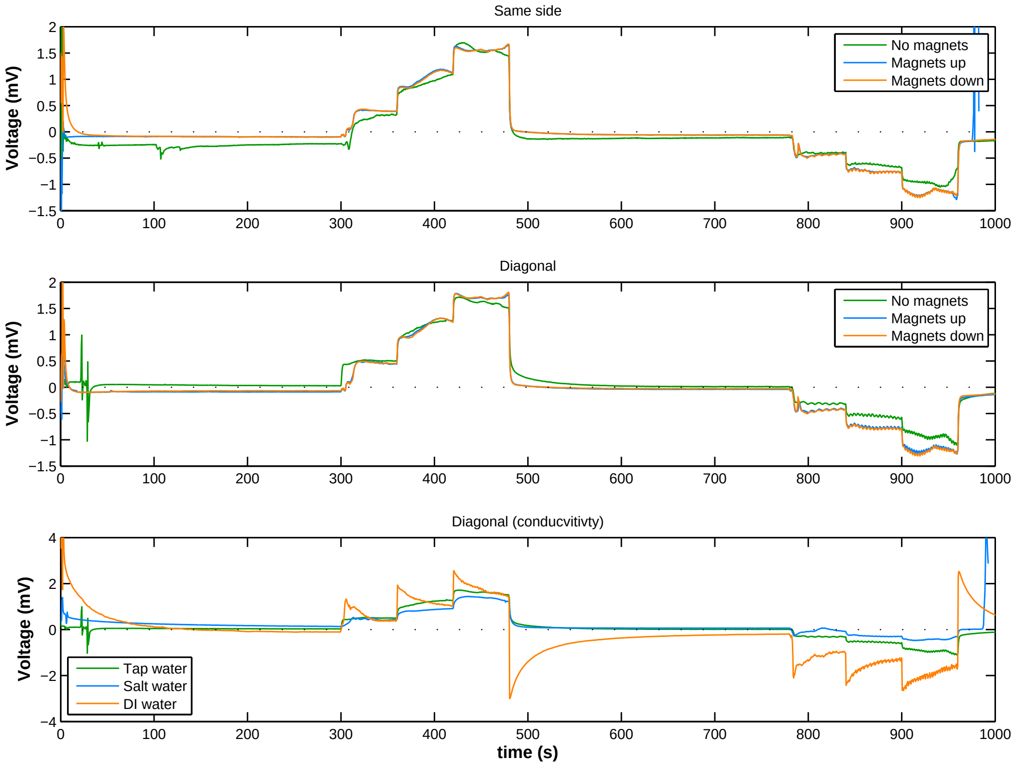

FIGURE 6.14: Diagonal and same side measurements for different various conductivities.

The results for the same side and diagonal measurements are very similar to the direct and differential measurement in shape. However, their mutual similarity is even stronger. In both measurements a difference between magnets and no magnets is visible, but there is hardly any difference between magnets up and down. Furthermore, the peaks are still not constant over time and there is also a difference in magnitude of the signal for infusing and withdrawing.

The diagonal measurement for various conductivities shows a different response. The signal clearly decreases for increasing salt concentration. The response for salt and tap water is similar to the response we have seen before in the direct, differential and same side measurement, but the de-ionzed water is clearly different. A very strong relaxation/charging-like peak can be observed. It takes a long time for the signal to go to a stable value after the flow is zero (just before 500s).

The ripples from the syringe pump, which are also visible in the flow controller measurement, are visible for withdrawing (after approximately 800s).

Comparison

This section provides an overview of the measurements performed with (permanent) magnets. The offset is set to zero. The top plot indicates no magnets, the middle one magnets up and the bottom one magnets down.

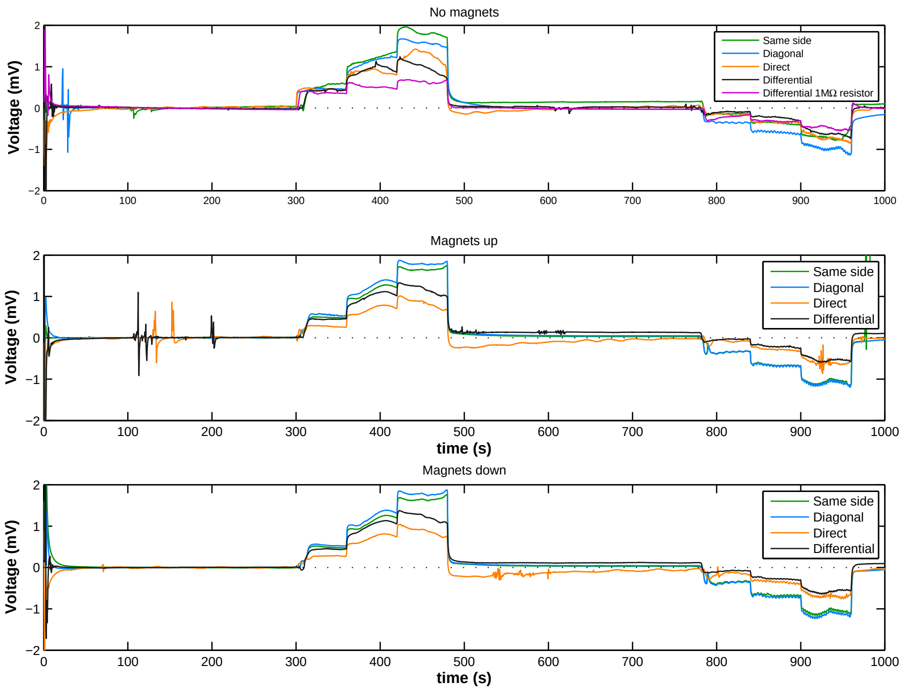

FIGURE 6.15: Comparison of all measurements with the offset is set to zero.

The same side and diagonal measurement have the largest (absolute) signal, whereas the differential with resistor in series has the smallest. The shape of the curves are very similar for the magnets up and down configuration. The no magnets measurement does not precisely follow this shape. Furthermore, for the magnets down and up configuration the same side and diagonal, and the direct and differential are very much alike in shape.

Duration measurement

The results of the duration measurement are plotted in Figure 6.16. The figure shows the response to a flow velocity of 69 (top), 139 (middle) and 208 (bottom) mm/s. These measurements have been performed with tapwater, without magnets and the diagonal measurement configuration. Note that the horizontal and vertical axis scale are differently for the three plots.

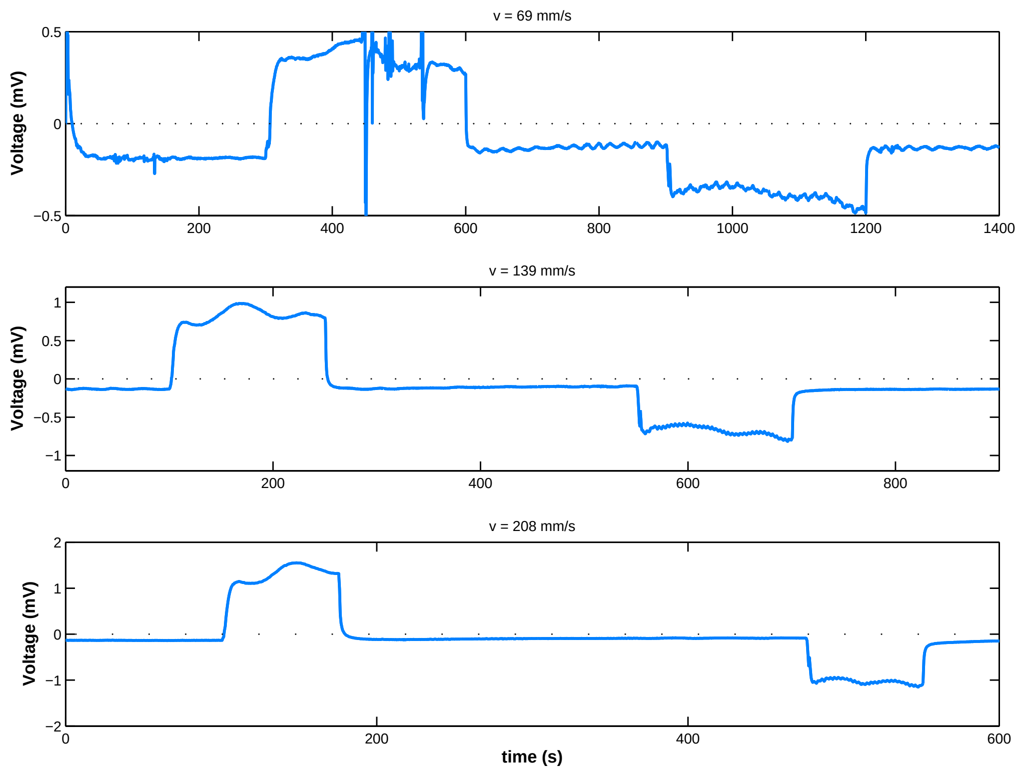

FIGURE 6.16: Duration measurement for flow velocities of 69, 139 and 208 mm/s.

An offset is present in the signal. The signal does not converge to a fixed value for both infusing and withdrawing. A difference between the signal magnitude for infusing and withdrawing is present.

Sanity check

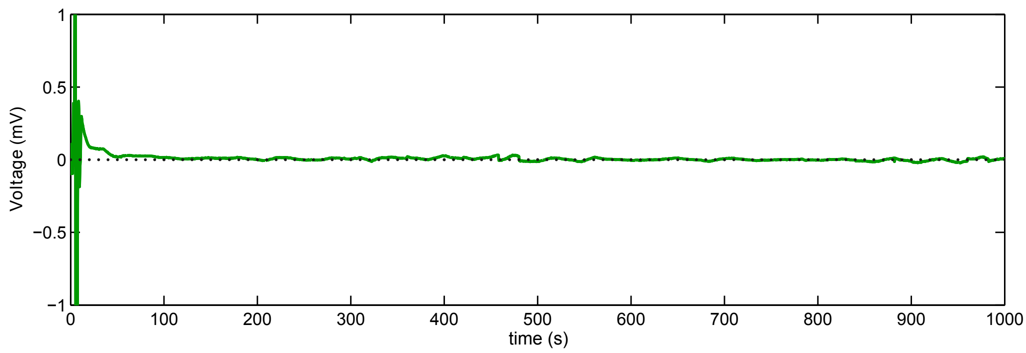

FIGURE 6.17: Sanity check: pumping fluid through one sensor, measuring an other. The output is not flow dependent.

It can be observed that the signal is not flow dependent. Hence the signal measured in other measurements is caused by a phenomenon that occurs *within* the sensor itself.

Alternating magnetic field

Before any flow measurements were performed with an alternating magnetic field, the coil was characterized by a magnetometer probe (Bell 615 Gauss meter) and an inductance analyzer (Peak ATLAS LCR40 automatic passive component analyzer). The inductance was measured to be 33.8 μH. The results of the magnetic field characterization are plotted in Figure 6.18.

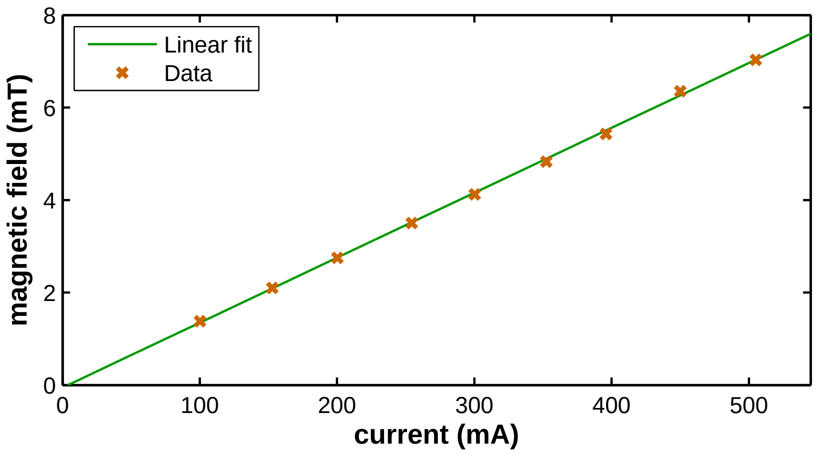

FIGURE 6.18: The measured magnetic field as a function of the current. The linear fit has a R-square value of 0.9994.

For a current of 500 mA the AC magnetic field is approximately 7 mT. This is about two orders of magnitude lower than the DC magnet field when permanent magnets are used, but we can also measure (more than) two orders of magnitude lower voltages since we can now use the lock-in amplifier.

Three different configurations have been measured in this section: the magnets are turned on, but the flow is zero (1), the magnets and the flow are turned on (2) and the magnets are turned off while there is a flow applied (3). Figure 6.19 shows the results of measurement (1) and (2). The top figure shows the measured data and the bottom one the normalized values, i.e. the offset is set to zero. Figure 6.20 shows the results of measurement (3): the magnets are turned of but the flow is turned on.

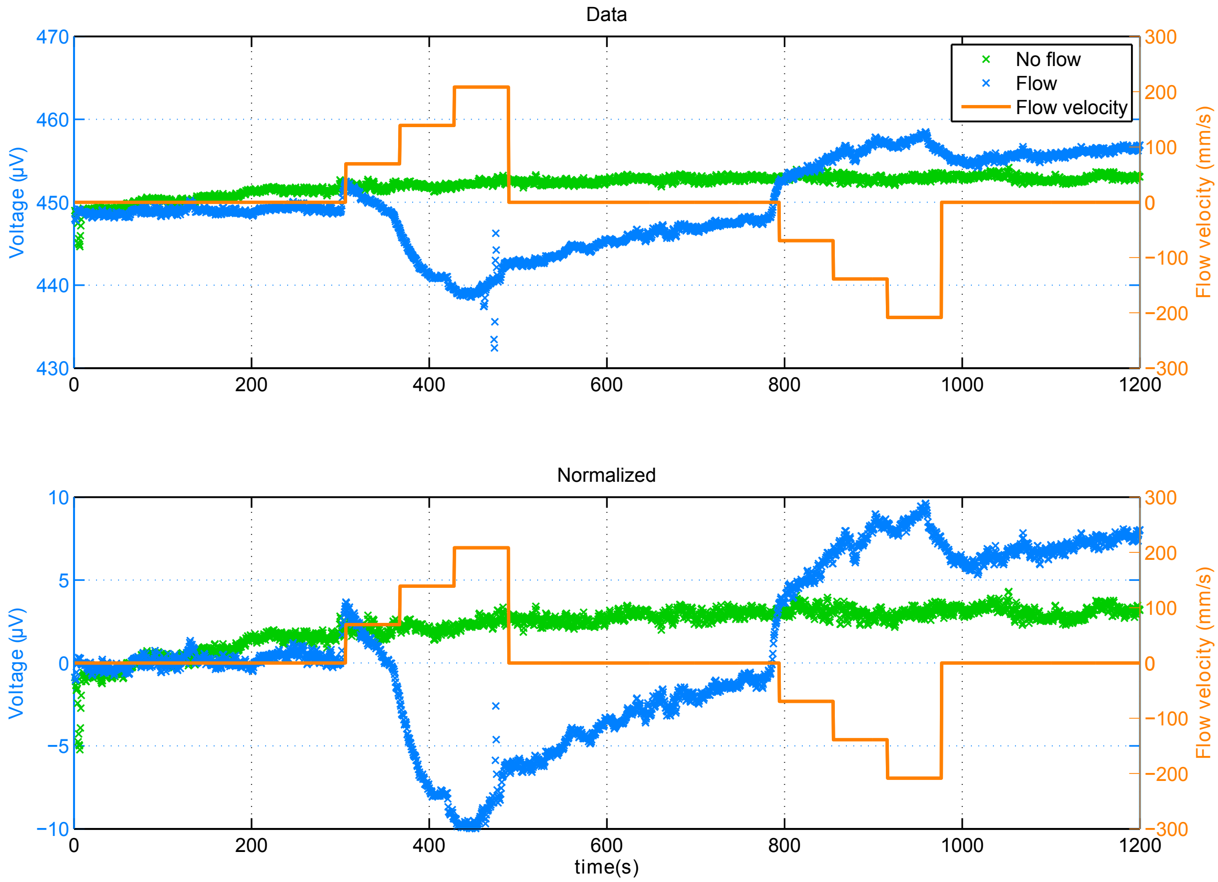

FIGURE 6.19: Top: measured data for no flow (green) and a flow applied (blue). The flow profile applied is indicated in orange. Note that the signal has an offset. Bottom: the same data as the top figure, but now the offset has been subtracted in order to see the variations in the signal better.

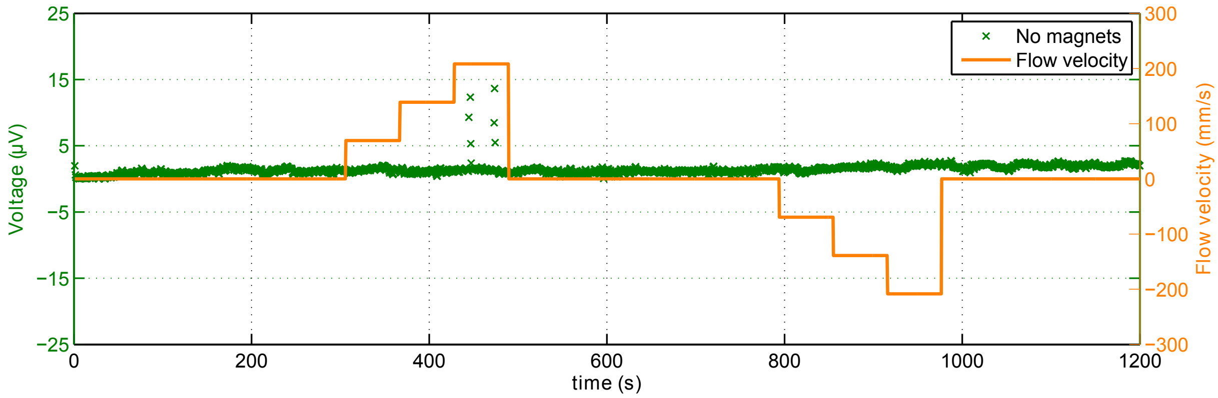

FIGURE 6.20: Noise measurement: the same measurement as in Figure 6.19 has been performed, but now no magnets were applied to the sensor.

The most important observation to make is that the signal is both flow and magnet dependent: for zero flow and magnets turned on we see no clear flow dependence, which we do see when the flow is applied. The signal follows the flow profile both in time and direction: when the flow makes the step, the signal also changes. In addition, when the flow direction is reversed, the signal also reverses. When the flow is applied, but the magnets are turned off, the signal is zero (within the noise).

An offset is present in the data. Also, all three measurements tend to increase over time.

6.2.3 Measurement results (angular acceleration driven)

The amplitude of the rotation is 50 mm for all frequencies. The distance between the mirror and the projection sheet was measured to be 175 mm. Therefore, the angle of rotation ϕ_0 can be calculated:

$$\phi_0 = 2\arctan\left(\frac{50/2}{175}\right) = 0.28 \tag{6.7}$$

Which is approximately 16.3 degrees. The angular acceleration is then calculated:

$$|\alpha| = 4\pi^2 f^2 \phi_0 \tag{6.8}$$

A lowpass filter (Stanford Research System Model SR650) has been set to 30 Hz and an output gain of 20dB. The voltage is then measured by a multimeter (HP34401A). The results are illustrated in Figure 6.21.

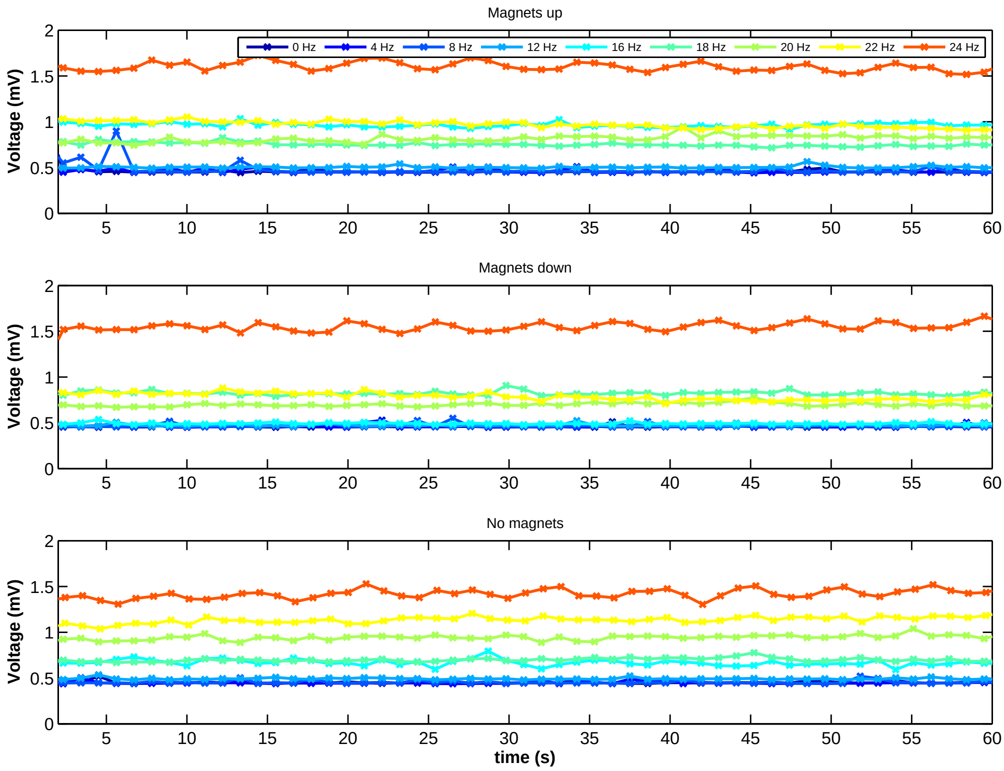

FIGURE 6.21: Measured voltages as a function of time for magnets up, down and without magnets for a variety of frequencies (and therefore angular acceleration).

In order to determine the measured voltage as a function of *angular acceleration* rather than time, the (time) average of the measured voltage from Figure 6.21 is calculated and displayed in Figure 6.22.

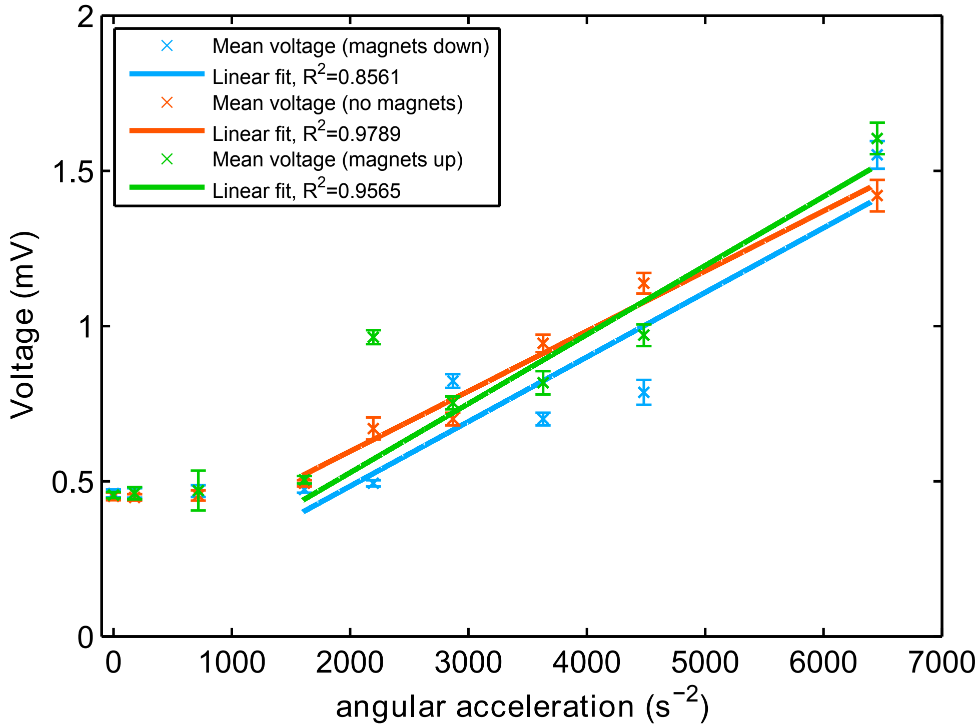

FIGURE 6.22: Measured voltages as a function of angular acceleration for magnets up, down and without magnets. A linear fit through the data points has been made. In this fit the anomaly at 16Hz for magnets up (approximately 2200 s^{-2}) has no been taken into account in this fit.

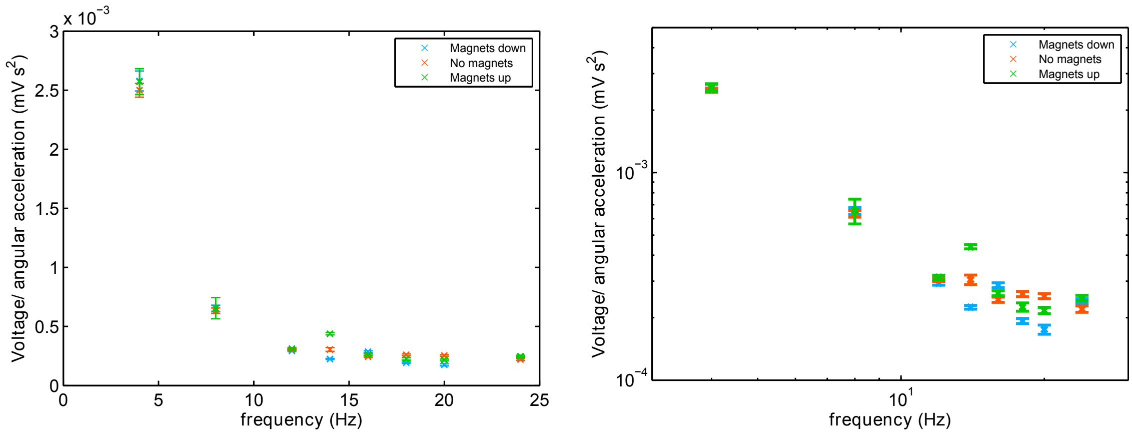

(a) Linear plot.

(b) Log-log plot.

FIGURE 6.23: Measured voltages as a function of frequency for magnets up, down and without magnets. Note that the angular acceleration is not constant here.

6.2.4 Discussion

The results do not fully correspond to the theory. The voltage V induced by the flow and magnetic field was predicted to be:

$$V = 2BRv_{\text{avg}} \tag{6.9}$$

From the expression for the magnetic field of a permanent magnet (Equation 4.42) we can calculate that the magnetic field in the channel is approximately 500 mT. The channel does not have a circular cross section, but a rectangular one. It is 3 mm wide so $R = 1.5$ mm is a good approximation. Hence the difference between magnets up and down at a flow velocity of 208 mm/s (the highest flow velocity used in this work) reads:

$$V_{\text{up}} - V_{\text{down}} = 2 \cdot 0.208 \cdot 1.5 \cdot 10^{-3}(0.5 - (-0.5)) = 0.6 \text{ mV} \tag{6.10}$$

This difference is an order of magnitude lower in the direct measurement. Furthermore, this difference should be consistent over the entire measurement, so if the flow becomes twice as small, the signal should also become two times smaller. This is not the case in the direct measurement.

To resolve this issue, a new sensor (the V2.0) had been designed and the differential measurement has been performed. In theory, measuring differentially should cancel the voltages induced by sources other than the magnetic field and double the voltage from the magnetic field:

$$V_{\text{sense}} = V_1 + V_2 = (V_{\text{magn}} + V_{\text{other}}) + (V_{\text{magn}} - V_{\text{other}}) = 2V_{\text{magn}} \tag{6.11}$$

So we should see no flow dependent signal if no magnets are applied to the sensor and see a difference of two times 0.6 mV, that is 1.2 mV, between magnets up and down. A very brief analysis of the differential measurement results (Figure 6.12) shows that this is absolutely not the case. The difference between the signal for magnets up and down is even smaller than in the direct measurement. The noise, however, seems to be lower than for the direct measurements.

Ideally, the resistance of the connection between the two measurements should not matter, since no current should be running through the system (assuming we have very high input impedance of the multimeter). To validate this statement, the differential measurement has been performed with a 1 and 10 MΩ resistor in series. The most important observation to make is that the signal decreases with respect to the original differential measurement (at least for the highest flow velocities). The difference between the signal for the 1 and 10 MΩ resistor is, however, not very clear. So apparently, contrary to our hypothesis, there is a current through the connecting wire. To understand this effect we should realize that the two measurement sites in the differential measurement are not isolated from each other: they have an (electrical) connection through the fluid.

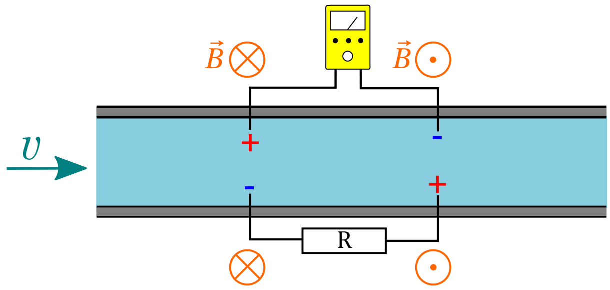

FIGURE 6.24: In the differential measurement the voltage is measured at two sites. These sites are, however, not isolated from each other, but are electrically connected through the fluid in the channel.

So we do not only have a potential difference in direction perpendicular to the flow, but also one parallel to it. This potential difference will lead to a current. This effect will not be present in the direct measurement.

The series resistor dependence is an important notion to make. But it does not explain why there is an other effect that is causing a voltage, that is in the same order of magnitude as we expect the voltage induced by the magnetic field to be. This effect does not only shows a strong correlation with the flow magnitude, but also with its *direction*: if the flow is positive, the voltage is positive, whereas if the flow is negative, the voltage is also negative [1]. This suggests that there has to be an asymmetry in the geometry. To further investigate this asymmetry, the diagonal and same side measurement have been performed.

No asymmetry has been designed in the sensor. However, an asymmetry could have been introduced in packaging the sensor and electrodes. It is nevertheless small (since it cannot be seen by eye it is at least smaller than 1 mm). So if the signal arises from the asymmetry of the geometry, it should increase (or at least change) if me make a very big asymmetry. This is done in the same side and diagonal measurement. These measurements indeed show a higher signal than the direct and differential ones. It is approximately 1.5 to 2 times higher in absolute value. But the asymmetry is at least one order of magnitudes higher (< 1mm in the direct measurement and 25 mm in the diagonal and same side measurement). So the asymmetry does have an influence, but it cannot fully explain the measurement data.

An other possible explanation of the voltage is the streaming potential. This potential depends (linearly) on the flow. The voltage reverses if the flow direction is reversed and it also works if no magnets are applied to the channel. For a given average flow velocity v_{avg} the streaming potential reads:

$$V_{\text{sp}} = \frac{6\epsilon\zeta}{\sigma}\frac{L}{R^2}v_{\text{avg}} \tag{6.12}$$

The ζ potential is in the order of 25 mV. Here, the cross sectional area is of importance, so now we take $R = \sqrt{\frac{0.4\cdot10^{-3}\cdot3\cdot10^{-3}}{\pi}} = 618\ \mu\text{m}$ [2]. For DI water and a velocity of 69 mm/s this potential reads:

[1] However, infusing and withdrawing do not give the opposite effect: the peak magnitude for infusing is generally higher than for withdrawing

[2] This radius corresponds to a circle with the same cross sectional area as the rectangularly shaped cross section of the sensor.

$$V_{\text{sp}} = \frac{6 \cdot 80 \cdot 8.85 \cdot 10^{-12} \cdot 25 \cdot 10^{-3}}{1.1 \cdot 10^{-4}} \frac{25 \cdot 10^{-3}}{(618 \cdot 10^{-6})^2} \cdot 0.069 \approx 4 \text{ mV} \tag{6.13}$$

Which is in the order of magnitude of the voltage we have measured. The streaming potential is inversely proportional to the conductivity. So the potential should go to zero for high conductivities. The diagonal measurement with tap, salt and DI water, does show a decrease in signal for increasing conductivity. However, the conductivity of DI water is two orders of magnitude lower than salt water, but the measured voltage is in the same order of magnitude. So the streaming potential can explain parts of the measured voltage, but it is not the only effect present in the sensor.

Another possible explanation is a reaction between the platinum electrodes and the liquid that leads to an electrochemical potential. If we take a close look at the results of the diagonal and same side measurement we see that applying magnets does change the shape of the signal. However, it does not matter if the magnets are up or down. This could mean that not so much the *magnetic field* has an influence, but the magnet's opacity: the channel is somewhat translucent whereas the magnets are not. If we a put the magnets on the sensor it gets darker in the sensor. If the process that gives rise to the potential is indeed an electrochemical one, it could very well be light sensitive. This would also explain why there is a conductivity dependence, since most electrochemical reactions depend on the salt concentration.

So an electrochemical reaction seems plausible, but it does not explain why there is a flow *direction* dependence. In addition, it is still strange that the voltage-flow velocity characteristics have a very similar shape for all measurements. So an electrochemical potential cannot fully explain the results either.

An other important issue to address is the fact that the voltage is not constant nor converges to a stable value when a flow is applied. This is further investigated in the duration measurement. This measurement does not show either that the signal reaches a stable value. The time scale makes in implausible that this is caused by the fluidic capacitance (the expansion of the channels) or inductance (the inertia of the water). Furthermore, the syringe pump and sensor have been characterized by a commercial flow meter. This measurement does not indicate a significant fluidic RC-time either. Therefore it is not likely that the non ideal behavior of the syringe pump prevents the signal from going to a constant value.

To be absolutely sure that we haven't missed an obvious issue in the measurement setup a sanity check has been performed: the fluid was pumped through one sensor, whereas the voltage was measured in an other one. This measurement shows no flow dependence.

The measurements performed so far do not provide any reason to believe that the electromagnetic readout principle works at all: applying magnets to the sensor does not have a clear effect on the data. Therefore the measurement with a time varying magnetic field has been performed. The advantage of this measurement is that we can use the frequency at which the magnetic field oscillates to amplify and filter the voltage by a lock-in amplifier. The results of this measurements show a clear flow velocity *and* direction dependence. But more importantly, when the magnets are turned off but there is a flow, we do not measure a signal. This measurement proves that electromagnetic readout can in principle be used to measure the flow velocity in the sensor.

Unfortunately, the design of the angular acceleration sensor does not allow the use of an alternating magnetic field. Therefore this sensor has been characterized with permanent magnets. Similar to the linear flow sensor, the angular acceleration shows no clear difference between magnets up, down and without magnets.

The majority of measurements was performed by a flow driven source. The effect of pressure is therefore not studied directly. We know from the Hagen-Poiseuille flow:

$$v_{\text{avg}} = \frac{1}{R}\int_0^R \frac{-\Delta P R^2}{4\mu L}\left(1-\left(\frac{r}{R}\right)^2\right)\,\mathrm{d}r = \frac{-\Delta P R^2}{6\mu L} \tag{6.14}$$

$$\Delta P = \frac{-6\mu L v_{\text{avg}}}{R^2} \tag{6.15}$$

$$= \frac{-6\cdot 8.9\cdot 10^{-4}\cdot 2.5\cdot 10^{-2}\cdot 0.2}{(0.6\cdot 10^{-3})^2} \approx -74\text{Pa} \tag{6.16}$$

Which is not a very high pressure. But that does not mean that it cannot have any effect. The deformation of the sensor due to this pressure difference could lead to a piezoelectric voltage for instance.

Furthermore, a combination of a flow- and pressure driven effect could explain parts of the signal behavior. Let us consider the electrodes to be in the middle of the sensor. If the flow is reversed, the electrodes also 'see' a reversing flow. The same is true for the pressure gradient. However, because of the symmetry, the *absolute* pressure at the electrodes does not change sign. Furthermore, a relaxation effect after a step in the driving force can be expected, but the time constants for the pressure and flow driven effect are not necessarily the same. The net effect of the two processes is depicted in the figure below

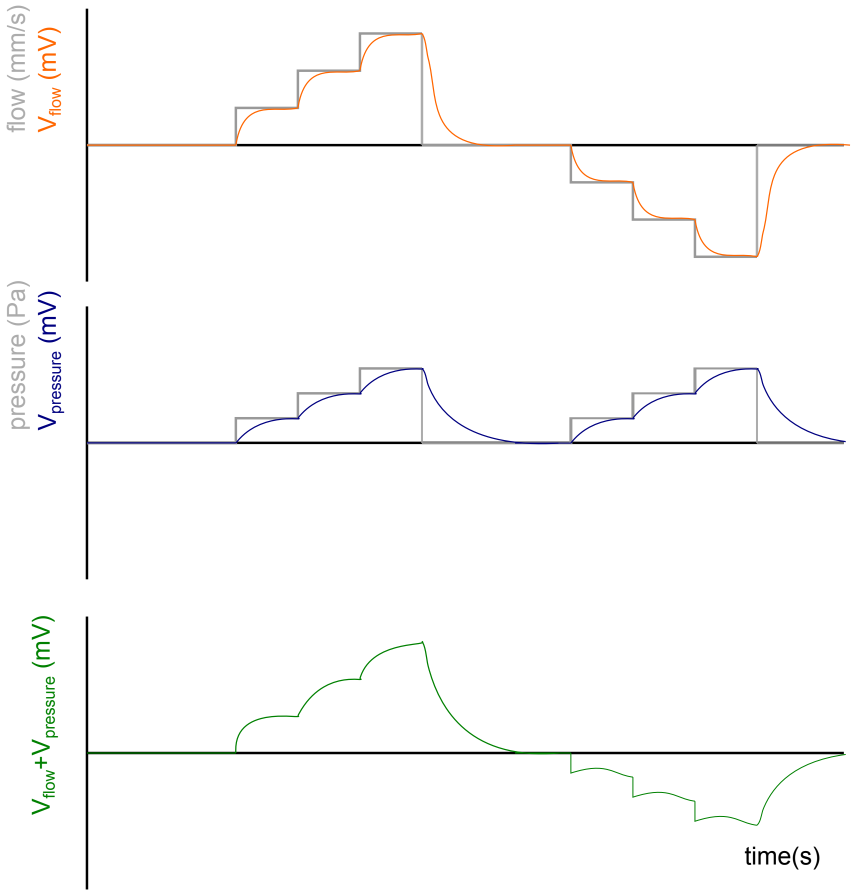

FIGURE 6.25: Top: applied step in flow (gray) and the electrical response to it (orange). Middle: electrical response (blue) to a step in pressure (gray). Bottom: the sum of the two induced potentials.

Even though this does not explain *what* pressure effect plays a role, it does explain the difference in the magnitude of the signal for withdrawing and infusing. However, from the duration measurement we see that even after more than 200 seconds the signal has not yet reached a stable value. Electrical relaxation times are not expected to be in that order. Furthermore, it is unlikely that a pressure of only 74 Pa causes such a strong effect [3]. In addition, in the angular acceleration sensor the pressure difference has to be zero because of the symmetry and we also see a voltage there. So it is unlikely that the voltage is solely induced by a pressure driven phenomenon.

Finally, it should be noted that all measurements were performed floating: no connection was grounded. Grounding the center of the channel should in theory not influence the magnetically induced voltage but it might suppress the other voltage inducing phenomena.

There is not one phenomenon that is able to explain all measurements. It is very likely that a variety of phenomena play a role at the same time. An overview of the phenomena discussed in this section is given in Table 6.1

[3]This pressure is more than a thousand times smaller than atmospheric pressure.

Phenomenon	Pros	Cons
Electromagnetic readout with constant magnetic field	-	• Theory predicts order of magnitude higher voltage • Voltage is also present without magnets
Electromagnetic readout causes potential diference parallel to the flow direction	• The signal drops when a resistor is placed in series	• Effect should not be present in direct measurement
Asymmetry	• Explains why the signal is depended on flow magnitude and direction	• Effect should increase when the asymmetry is bigger, which it does not
Electrochemical reaction	• Light dependent reaction explains difference between signal in no magnets and magnets, but no difference between magnets up and down. • Explains conductivity dependence.	• Should not be sensitive for the flow *direction*, which it is.
Streaming potential	• Theoretical and experimental potential in the same order of magnitude • Depends (linearly) on flow velocity and direction	• Potential should drop to zero for high conductivities, which it does not. • Because of the symmetry the streaming potential cannot be nonzero in the angular acceleration sensor

Non ideal behavior fluidic network / syringe pump	• Could explain why the signal does not reach a stable value.	• Duration measurement does not show a stable value either • Commercial flow measurement indicates the associated time constant is smaller than a few seconds.
Pressure-flow driven phenomenon/ piezoelectric	• Partly explains the shape of the signal and the difference between infusing and withdrawing	• Duration measurement does not show a stable value • Pressure difference is small • Pressure gradient is zero in the angular acceleration sensor

TABLE 6.1: Overview of the most important phenomena discussed in this section.

Chapter 7

Conclusions and recommendations

Two types of angular acceleration sensors based on the same biomimetic geometry have been modeled, designed and fabricated. A setup has been made to characterize the sensors.

The fabrication of the micromachined sensor has been successful. However, the final assembly and in particular the filling process has hindered the final characterization. In future designs there could be more space between the inlets on the chip. Furthermore, the inlet unit used to fill the chips could be extended to prevent glue from clogging the inlets.

Flow measurements for a linear flow sensor with electromagnetic readout with a constant magnetic field have been performed. No clear and consistent difference in signal was observed between a sensor with and without magnetic field applied. Therefore, there has to be a phenomenon that induces a voltage that depends on the flow direction and magnitude, without a magnetic field applied. The most plausible explanation for the observations is a combination of effects, including the streaming potential, a pressure driven effect and an electrochemical reaction. Further research has to be performed on the precise underlying phenomena. The principle of electromagnetic flow sensing has been demonstrated for a linear flow sensor with an alternating magnetic field. The design of the angular acceleration sensor could be expanded so that the use of an alternating magnetic field is also possible on this sensor.

The two types of fabrication, microtechnology and 3D printing, both have their benefits and drawbacks. The main advantage of microtechnology is its very small feature size ($< 1\mu$m) and the ability to fabricate integrated systems. Currently, the smallest features 3D printing can fabricate are approximately 100 μm. However, it is a full three dimensional fabrication technique and allows rapid prototyping. Furthermore, it does not require a complex infrastructure and is therefore far less expensive than micromachining. So 3D printing has a lot of potential as a fabrication technique in transducer science and other fields.

Acknowledgements

Many people have contributed to this work. I would like to thank a couple of them in particular.

Jarno, you helped me a lot during this project and since I walked into your office almost every day, you really were my *daily* supervisor. I could ask any question I had, such as if you liked illustrations of Arctic islands on a chip or whether my 3D printed devices should be rounded or not. Gijs, I remember you being my first teacher from my first university course. I was extremely relieved that I passed that course, who would have thought that I would be writing the acknowledgments of my master thesis five years later? I truly appreciated your way of supervising during this project. In our discussions I always had the feeling that we were looking for a solution together. Jan, I enjoyed our discussions on the strange behavior of the sensors. You were not only an external member to keep an eye on the report: our discussions were very helpful and you gave me many useful suggestions. Remco, a couple of times I was stuck in the physical modeling of the sensors. A five minute talk with you gave me enough ideas to get going again. Thanks for the enlightening suggestions.

In addition, I would also like to express my gratitude to Dennis Alveringh, Remco/Pino Sanders and Robin Buijs. Dennis, you helped me a lot during this thesis. Sometimes you improved my Inkscape or Comsol skills, then you helped me to become a true electrical engineer by burning some components and always you were a very pleasant fellow student and colleague. Pino, your practical help was extremely valuable: mechanically hacking a hard disk, gluing my sensor with a dentists lamp and supplying me with enough *pepernoten* to get through the day. Robin, I have enjoyed having you as a fellow student in the student room. We have had a lot of fruitful (late night) discussions and I enjoyed being cleanroom rookies together.

Last, but not least, I would like to thank my parents Frans and Elly and my girlfriend Inge. Your support has been of paramount importance in successfully completing my education.

Appendix A

Off-center rotation

This section describes the fluid dynamics for the situation in which the axis of rotation is not exactly equal to the middle of the sensor. Consider a center of rotation *inside* the sensor.

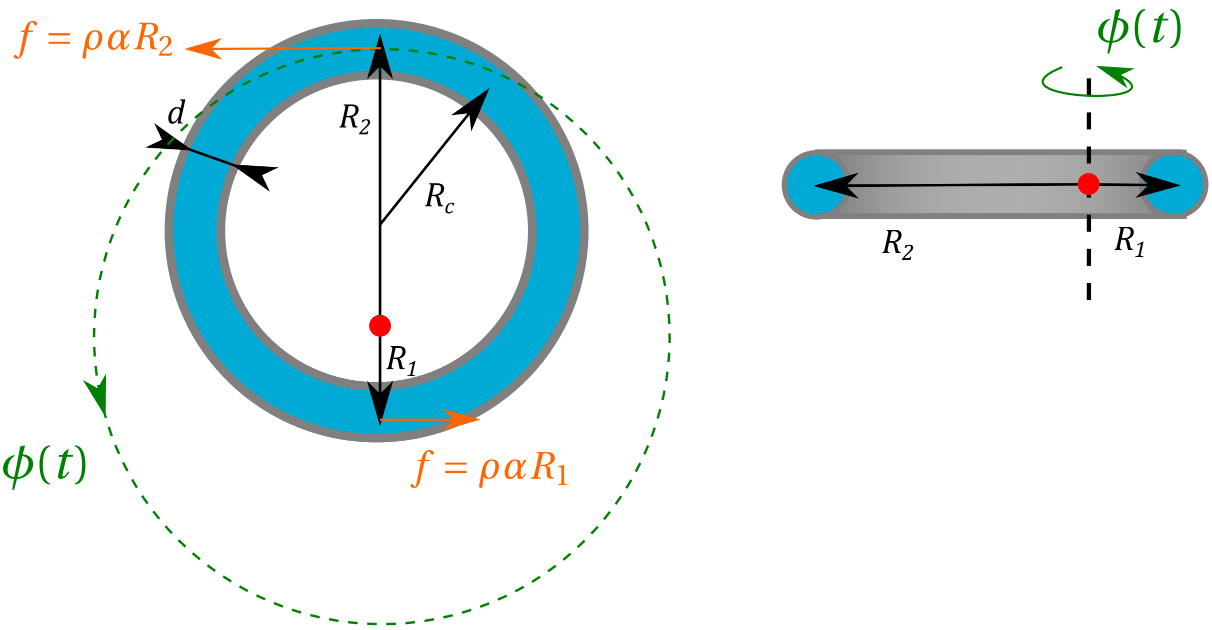

FIGURE A.1: Left: top view, right: cross sectional view. Instead of rotating around its own center axis with radius R_c, the sensor rotates around the center indicated by the red dot.

A couple of assumptions made in Equation 2.13 are not valid anymore: because of the broken symmetry the body force is not uniform over the axial direction of the channel anymore: at the 'top' of the channel ($z = 0$) in Figure A.1 the body force is equal to $\rho\gamma_2 R_2$ whereas at the bottom ($z = \pi R_c$) it equals $\rho\gamma_2 R_1$. Since the fluid velocity has to be the same everywhere in the channel (water is incompressible and the channel is fully circular) there has to be a pressure gradient counteracting this difference in body forces. Therefore, we can also no longer assume that there are no pressure gradients over the channel. In addition, we can also have a body force in the radial direction. We will, however, still assume that the diameter of the channel is small compared to the radius of rotation.

The Navier-Stokes equations become:

$$-\rho\left(v_r(r,z)\frac{\partial v_r(r,z)}{\partial r}+v_z(r,z)\frac{\partial v_r(r,z)}{\partial z}\right)-\frac{\partial p(r,z)}{\partial r}+ \mu\left[\frac{\partial^2 v_r(r,z)}{\partial r^2}+\frac{1}{r}\frac{\partial v_r(r,z)}{\partial r}+\frac{\partial^2 v_r(r,z)}{\partial z^2}-\frac{v_r(r,z)}{r^2}\right]+f_r=0 \quad \text{(A.1)}$$

$$-\rho\left(v_r(r,z)\frac{\partial v_z(r,z)}{\partial r}+v_z(r,z)\frac{\partial v_z(r,z)}{\partial z}\right)-\frac{\partial p(r,z)}{\partial z}+ \mu\left[\frac{\partial^2 v_z(r,z)}{\partial r^2}+\frac{1}{r}\frac{\partial v_z(r,z)}{\partial r}+\frac{\partial^2 v_z(r,z)}{\partial z^2}\right]+f_z=0 \quad \text{(A.2)}$$

Note that r is still taken with respect to the channel: so $r=0$ in the middle of the channel, $r=R$ at the wall. Before we can solve these equations to find the flow profile, we need to find expressions for f_r and f_z. Because the symmetry is broken, the body force will vary over the channel and we will have to introduce an angle dependence. Let us consider the geometry in Figure A.2.

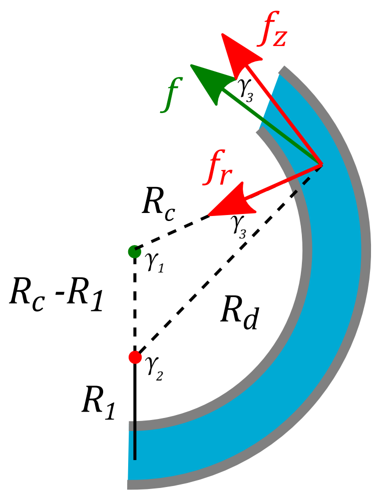

FIGURE A.2: Because of the broken symmetry the body force (green) has both a component in the radial and axial direction (red). We will still assume that the diameter of the channel is small compared to R_1.

Let us first try to find f_r and f_z as a function of γ_2. Performing the sine rule on the dashed triangle and noting that $\gamma_1=\gamma_2-\gamma_3$ yields:

$$\frac{R_c}{\sin(\pi-\gamma_2)}=\frac{R_c-R_1}{\sin(\gamma_3)}=\frac{R_d}{\sin(\gamma_2-\gamma_3)} \quad \text{(A.3)}$$

Which are two equations with two unknowns (R_d and γ_3). Solving yields

$$\gamma_3 = \arcsin\left(\frac{R_c - R_1}{R_c}\sin(\gamma_2)\right) \tag{A.4}$$

$$R_d = R_c\frac{\sin(\gamma_2 - \gamma_3)}{\sin(\gamma_2)} \tag{A.5}$$

Applying trigonometry yields a closed expression for R_d:

$$R_d = R_c\sqrt{1 - \frac{(R_c - R_1)^2}{R_c^2}\sin^2(\gamma_2)} - (R_c - R1)\cos(\gamma_2) \tag{A.6}$$

Which is a closed form, but also a rather complex expression. A quick check shows that $R_d(\gamma_2 = 0) = R_1$ and $R_d(\gamma_2 = \pi) = 2R_c - R_1$, as is expected from the geometry. The *total* body force f is normal to R_d and reads:

$$f = \rho\gamma_2 R_d \tag{A.7}$$

The component in the axial direction f_z (z-direction, normal to R_c) and the radial direction f_r (r-direction, parallel to R_c) depend on the angle:

$$f_r = \rho\alpha R_d\sin(\gamma_3) \tag{A.8}$$

$$f_z = \rho\alpha R_d\cos(\gamma_3) \tag{A.9}$$

Substituting in the expressions for R_d and γ_3 we find:

$$f_r(\gamma_2, \alpha = \rho\alpha\frac{R_c - R_1}{R_c}\left[R_c\sqrt{1 - \frac{(R_c - R_1)^2}{R_c^2}\sin^2(\gamma_2)} - (R_c - R1)\cos(\gamma_2)\right]\sin(\gamma_2) \tag{A.10}$$

$$f_z(\gamma_2, \alpha) = \rho\alpha\left[R_c\left(1 - \frac{(R_c - R_1)^2}{R_c^2}\sin^2(\gamma_2)\right) - (R_c - R_1)\cos(\gamma_2)\sqrt{1 - \frac{(R_c - R_1)^2}{R_c^2}\sin^2(\gamma_2)}\right] \tag{A.11}$$

So we have found closed expressions for f_r and f_z, but they are still a function of γ_2. In order to be useful in the Navier stokes equation, they should be a function of z. From Figure A.2 we can observe that

$$\gamma_1 = \gamma_2 - \gamma_3 = \frac{z}{R_c} \tag{A.12}$$

Since we have an expression for γ_3 we can solve Equation A.12 for γ_2:

$$\gamma_1 = \frac{z}{R_c} = \gamma_2 - \arcsin\left(\frac{R_c - R_1}{R_c}\sin(\gamma_2)\right) \tag{A.13}$$

$$\gamma_2 = -\arctan\left[\frac{\sin\left(\frac{z}{R_c}\right)}{-\cos\left(\frac{z}{R_c}\right) + \frac{R_c - R_c}{R_c}}\right] \tag{A.14}$$

Combining Equation A.14 with Equation A.10 and Equation A results in an expression for f_r and f_z as a function of z. These expressions can be used in the Navier-Stokes equations to find the flow profile. The resulting differential equation, is however, extremely complicated and not readily solvable. If we neglect the the flow in the radial direction Equation A.1 becomes:

$$\frac{\partial p}{\partial r} = f_r \tag{A.15}$$

Because of the incompressibility of water we know that $\nabla \cdot \vec{v} = 0$. In addition, we know that the channel is fully circular. Hence, we find two conditions that the pressure profile should satisfy:

$$\frac{\partial^2 p}{\partial z^2} = \frac{\partial f_z}{\partial z} \tag{A.16}$$

$$p(r,z) = p(r, z + 2\pi R_c) \tag{A.17}$$

Because of the complexity of the expression of f_r, Equation A.15 is still, however, a very complicated expression to solve.

Appendix B

List of constants

This appendix provides the analytical values of several (long) expressions.

B.1 Equation 3.14

The solution for $T(x)$, as described in section 3.1.1, reads:

$$T(x) = \begin{cases} A_1 e^{\beta x} + B_1, & \text{if } -L \leq x \leq -x_h \\ \frac{1}{\beta}\left[A_c e^{\beta x} + \frac{Q}{k}x\right] + B_c, & \text{if } |x| \leq x_h \\ A_2 e^{\beta x} + B_2, & \text{if } x_h \leq x \leq L \end{cases} \tag{B.1}$$

We take $\beta = \rho c_p v / k$. The constants have the following values:

$$A_1 = Qe^{-\beta L}\left(\frac{2\beta x_h + e^{\beta(L-x_h)} - e^{\beta(L+x_h)}}{k\beta^2\left(e^{\beta L} - e^{-\beta L}\right)}\right) \tag{B.2}$$

$$A_2 = Qe^{\beta L}\left(\frac{2\beta x_h + e^{-\beta(L+x_h)} - e^{-\beta(L-x_h)}}{k\beta^2\left(e^{\beta L} - e^{-\beta L}\right)}\right) \tag{B.3}$$

$$B_1 = -Q\left(\frac{2\beta x_h + e^{\beta(L-x_h)} - e^{\beta(L+x_h)}}{k\beta^2\left(e^{\beta L} - e^{-\beta L}\right)}\right) \tag{B.4}$$

$$B_2 = -Q\left(\frac{2\beta x_h + e^{-\beta(L+x_h)} - e^{-\beta(L-x_h)}}{k\beta^2\left(e^{\beta L} - e^{-\beta L}\right)}\right) \tag{B.5}$$

$$A_c = Q\left(\frac{-2\beta x_h + e^{-\beta(L-x_h)} - e^{-\beta(L-x_h)}}{k\beta\left(e^{\beta L} - e^{-\beta L}\right)}\right) \tag{B.6}$$

$$B_c = Q\left(\frac{(\beta x_h + 1)e^{\beta L} + (\beta x_h - 1)e^{-\beta L} + e^{-\beta x_h} - e^{\beta x_h}}{k\beta^2\left(e^{\beta L} - e^{-\beta L}\right)}\right) \tag{B.7}$$

Note that by definition of the constants in the solution they do not all have the same unit!

B.2 Equation 3.44

The expression for $\delta T_0(x)$, as described in section 3.1.1, reads:

$$\delta T_0(x) = A_i \cos\left[\zeta(\omega)(1-j)x\right] - B_i \sin\left[\zeta(\omega)(1-j)x\right] + j\frac{v_0 Q x_h}{\omega k}\begin{cases} 1, & \text{if } -L \le x \le -x_h \\ -x/x_h, & \text{if } |x| \le x_h \\ -1, & \text{if } x_h \le x \le L \end{cases} \tag{B.8}$$

The constants correspond to different regions:

	region
A_1, B_1	$x \in [-L, x_h]$
A_2, B_2	$x \in [-x_h, x_h]$
A_3, B_3	$x \in [x_h, L]$

Note that $\zeta = \zeta(\omega) = \sqrt{\frac{\rho c_p \omega}{2k}}$. All constants are linear in v_0 and Q.

$$A_1 = \frac{(1-j)}{\zeta(\omega)}\frac{Q v_0}{\omega}\sin\left[\zeta(1-j)x_h\right] \tag{B.9}$$

$$A_2 = 0 \tag{B.10}$$

$$A_3 = -A_1 = -\frac{(1-j)}{\zeta(\omega)}\frac{Q v_0}{\omega}\sin\left[\zeta(1-j)x_h\right] \tag{B.11}$$

$$B_1 = \frac{Q v_0}{\sin\left[\zeta(1-j)L\right]}\left(\frac{-1}{2k\omega\zeta(\omega)}\cos\left[\zeta(1-j)L\right]\sin\left[\zeta(1-j)x_h\right](1-j) - j\frac{x_h}{\sqrt{2}k\omega}\right) \tag{B.12}$$

$$B_2 = \frac{Q v_0}{\sin\left[\zeta(1-j)L\right]}\left(\frac{1}{2k\omega\zeta(\omega)}\left\{\sin\left[\zeta(1-j)L\right]\cos\left[\zeta(1-j)x_h\right] + \cos\left[\zeta(1-j)L\right]\sin\left[\zeta(1-j)x_h\right]\right\}(1-j) - j\frac{x_h}{\sqrt{2}k\omega}\right) \tag{B.13}$$

$$B_3 = B_1 \tag{B.14}$$

Appendix C

Mask designs

Four masks in total have been fabricated: release, metal, back and channel mask. Yellow indicates the (fabricated) channel. This is not part of the final mask, since it is fabricated by the slits in the channel mask (purple).

The chips have been named after towns in countries I lived in the last two years. Chips with a name of a town on Svalbard, Norway have a single slit channel, whereas a name of a town on Greenland denotes a triple slit channel. The figure in the upper right corner is an illustration of Greenland or Svalbard. Since the rectangular chip will not be used as an angular acceleration sensor it is not named after towns on Svalbard or Greenland, but after Vancouver, Canada.

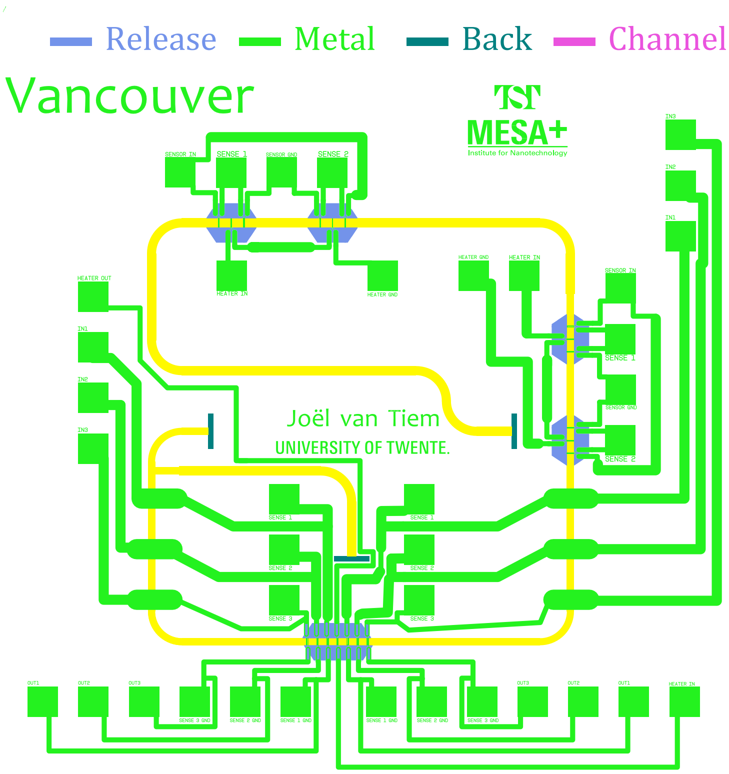

(a) Vancouver, both single and triple slits.

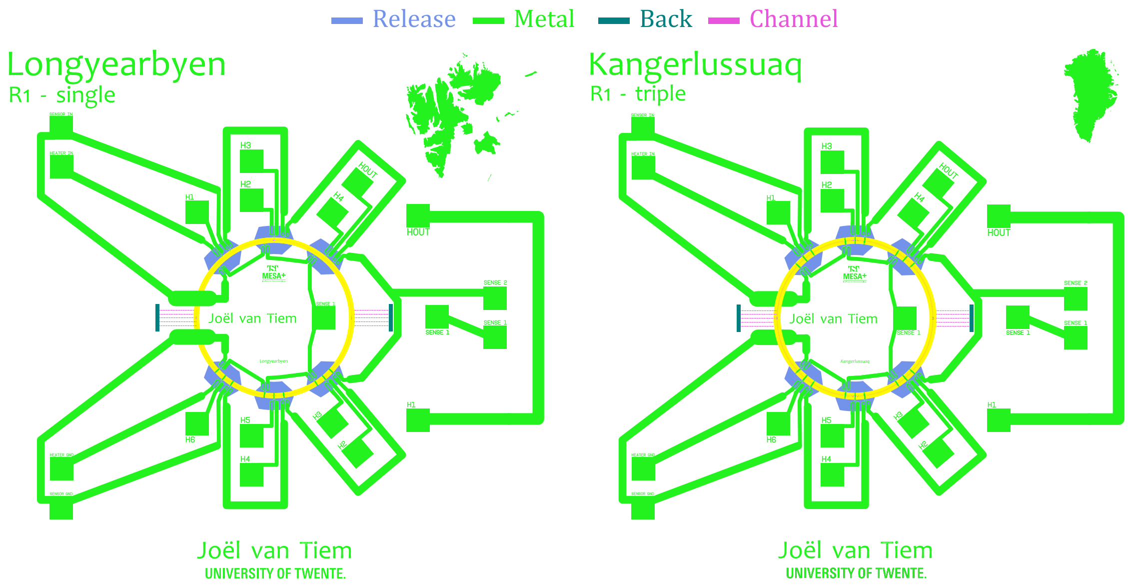

(b) Longearbyen. $R_c = 1$mm, single slits.

(c) Kangerlussuaq. $R_c = 1$mm, triple slits.

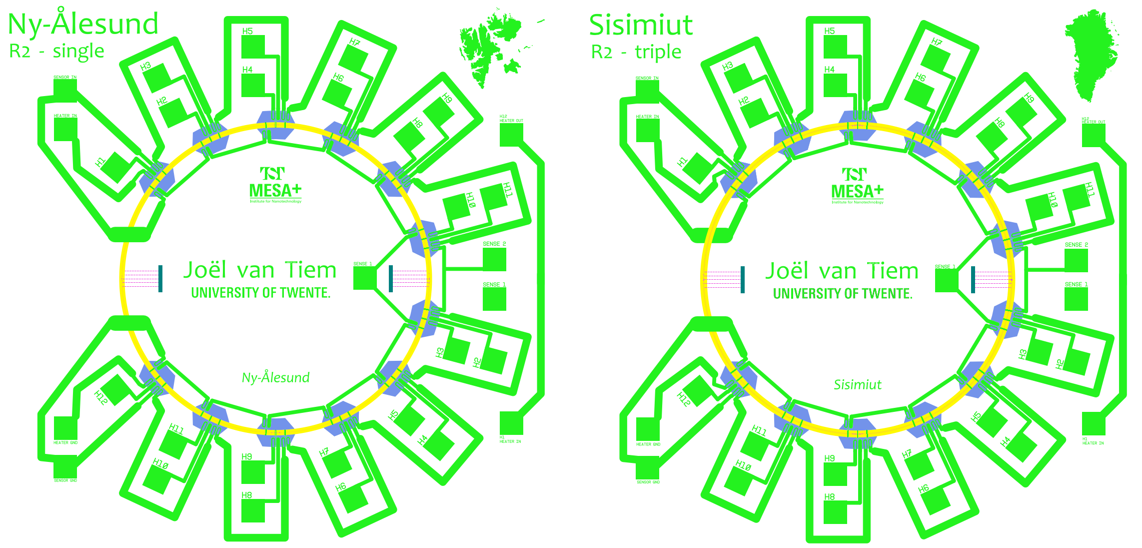

(d) Ny-Ålesund. $R_c = 2$mm, single slits.

(e) Sisimiut. $R_c = 2$mm, triple slits.

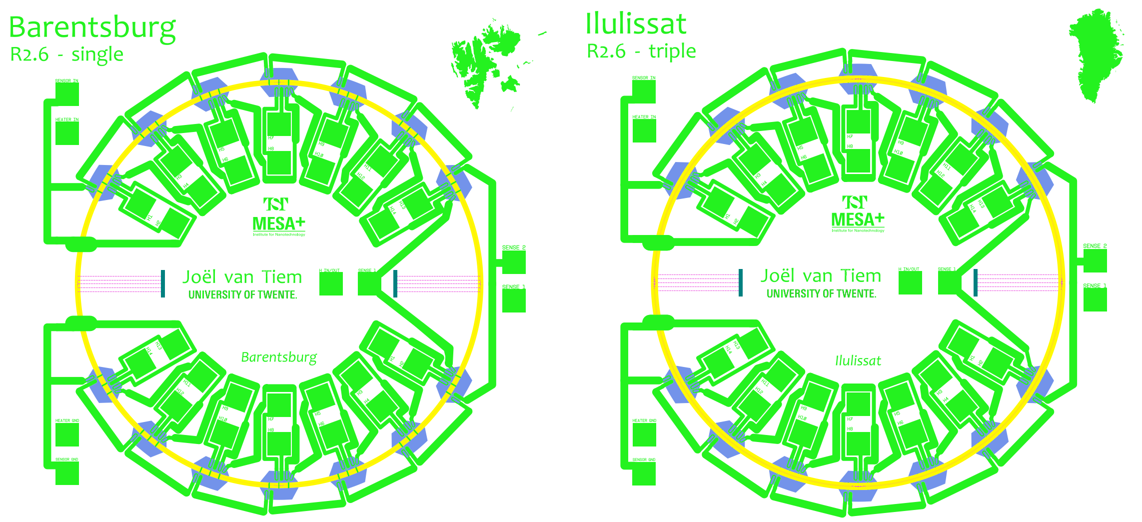

(f) Barentsburg. $R_c = 2.6$mm, single slits.

(g) Ilulissat. $R_c = 2.6$mm, triple slits.

Appendix D

Micromachined sensors

An overview of the fabricated sensors can be found here.

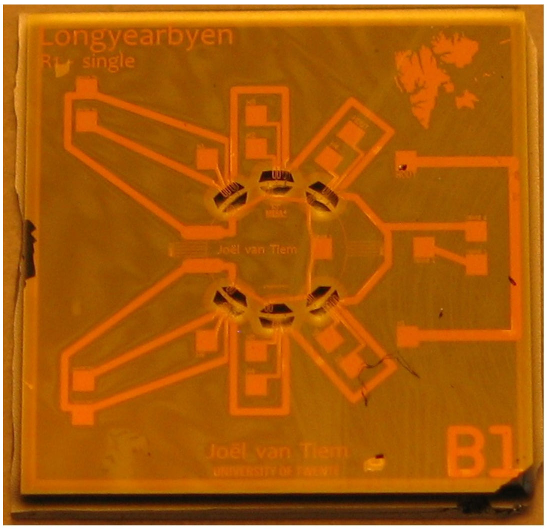

(h) Longearbyen. R_c = 1mm, single slits.

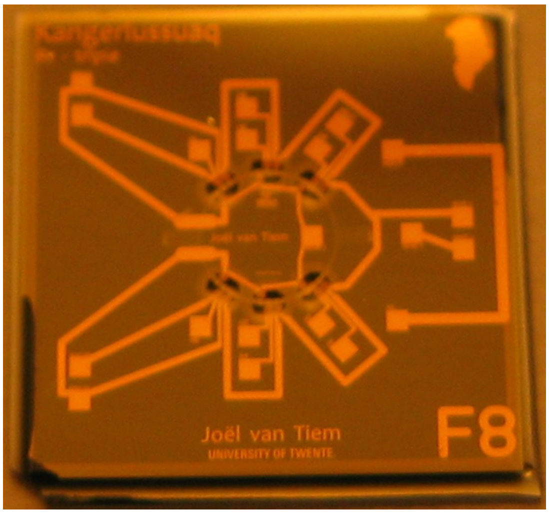

(i) Kangerlussuaq. R_c = 1mm, triple slits.

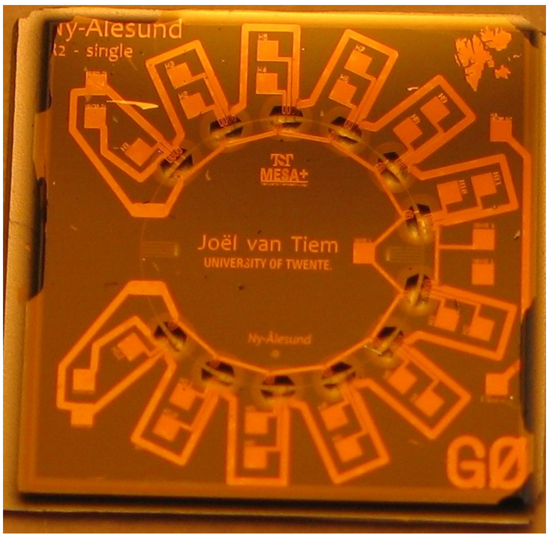

(j) Ny-Ålesund. R_c = 2mm, single slits.

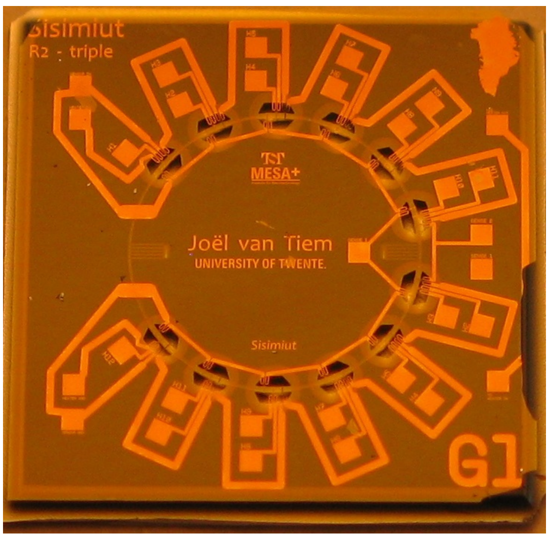

(k) Sisimiut. R_c = 2mm, triple slits.

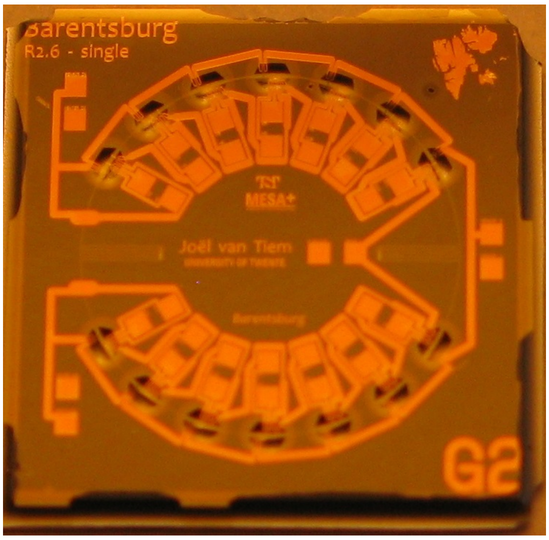

(l) Barentsburg. $R_c = 2.6$mm, single slits.

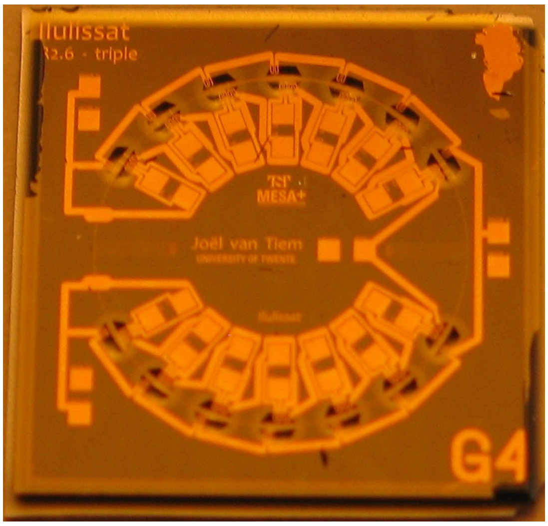

(m) Illulisat. $R_c = 2.6$mm, triple slits.

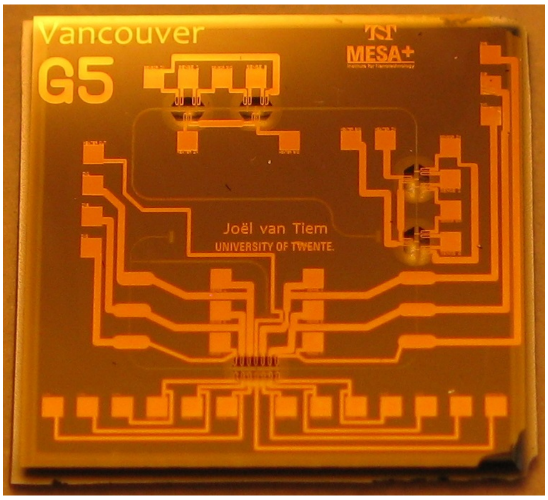

(n) Vancouver, both single and triple slits.

Appendix E

Electromagnetic readout for a rectangular cross section

The analysis performed previously is only valid for a cylindrical channel. Let us consider a channel with a rectangular cross section: $S = [0, a] \times [0, b]$. Therefore, $v = v(x, y)$ and Equation 4.23 becomes:

$$\left(\frac{\partial^2}{\partial x^2} + \frac{\partial^2}{\partial y^2}\right) U(x, y) = B\frac{\partial v(x, y)}{\partial y}, \quad \text{for } (x, y) \in S \tag{E.1}$$

With the corresponding set of boundary conditions.

$$\frac{\partial U(x, y)}{\partial \hat{n}} = 0, \quad \text{for } (x, y) \in \delta S \tag{E.2}$$

$$U(0, 0) = 0 \tag{E.3}$$

In which δS is the edge of S. The velocity profile will also be different because for a rectangular channel. The Navier-Stokes equation and the no-slip boundary condition now become:

$$\mu\left(\frac{\partial^2}{\partial x^2} + \frac{\partial^2}{\partial y^2}\right) v(x, y) = \rho R_c \alpha \tag{E.4}$$

$$v(x, y) = 0 \quad \text{for } (x, y) \in \partial S \tag{E.5}$$

In order to solve Equation E.1 we have to know the flow profile, i.e. the solution to Equation E.4. Taking a close look at both equations learns that the differential equations are *mathematically* identical [1]. So if we are able to solve one equation, we should in principle be able to solve the other.

For simplicity, let us denote Equation E.1 as:

$$\nabla^2 U(\vec{x}) = f(\vec{x}) \tag{E.6}$$

[1] The boundary conditions are different

Where $\nabla^2 = \left(\frac{\partial^2}{\partial x^2} + \frac{\partial^2}{\partial y^2}\right)$, $\vec{x} = (x, y)$ and $f(\vec{x}) = B\frac{\partial v(x,y)}{\partial y}$. This partial differential equation can be solved by means of a Green's function. Let $G(\vec{x}, \vec{s})$ be a function that obeys the following equation:

$$\nabla^2 G(\vec{x}, \vec{s}) = \delta^2(\vec{x} - \vec{s}) \tag{E.7}$$

In which δ^2 is the two-dimensional Dirac delta function and $\vec{s} \in S$. The solution of Equation E.6 then reads [39]:

$$U(\vec{x}) = \psi(\vec{x}) + \iint_S G(\vec{s}')f(\vec{s}')\mathrm{d}\vec{s}' \tag{E.8}$$

In which $\psi(\vec{x})$ is the solution to the homogeneous part of Equation E.6 (including the boundary conditions). Equation E.7 has the property that $G(\vec{x}, \vec{s}) = G(\vec{x} - \vec{s}) = G(\vec{s}')$ [40]. Hence we obtain [2].

$$\nabla^2 G(\vec{s}') = \delta^2(\vec{s}') \tag{E.9}$$

$$G(\vec{s}') = \frac{\ln|\vec{s}'|}{2\pi} \tag{E.10}$$

Let $\vec{s}' = (\chi, \xi)$. Hence we obtain for $U(\vec{x})$:

$$\boxed{U(\vec{x}) = \psi(\vec{x}) + \int_0^a \int_0^b \frac{\ln\left(\sqrt{\chi^2 + \xi^2}\right)}{2\pi} f(\chi, \xi)\mathrm{d}\chi\mathrm{d}\xi} \tag{E.11}$$

Which is an equation in closed form that we could solve in principle.

[2]This differential equation can be solved using a Fourier transform: $\mathscr{F}\left(\nabla^2 G(\vec{s}')\right) = 1$

Appendix F

3D printed designs

F.1 Angular acceleration sensor

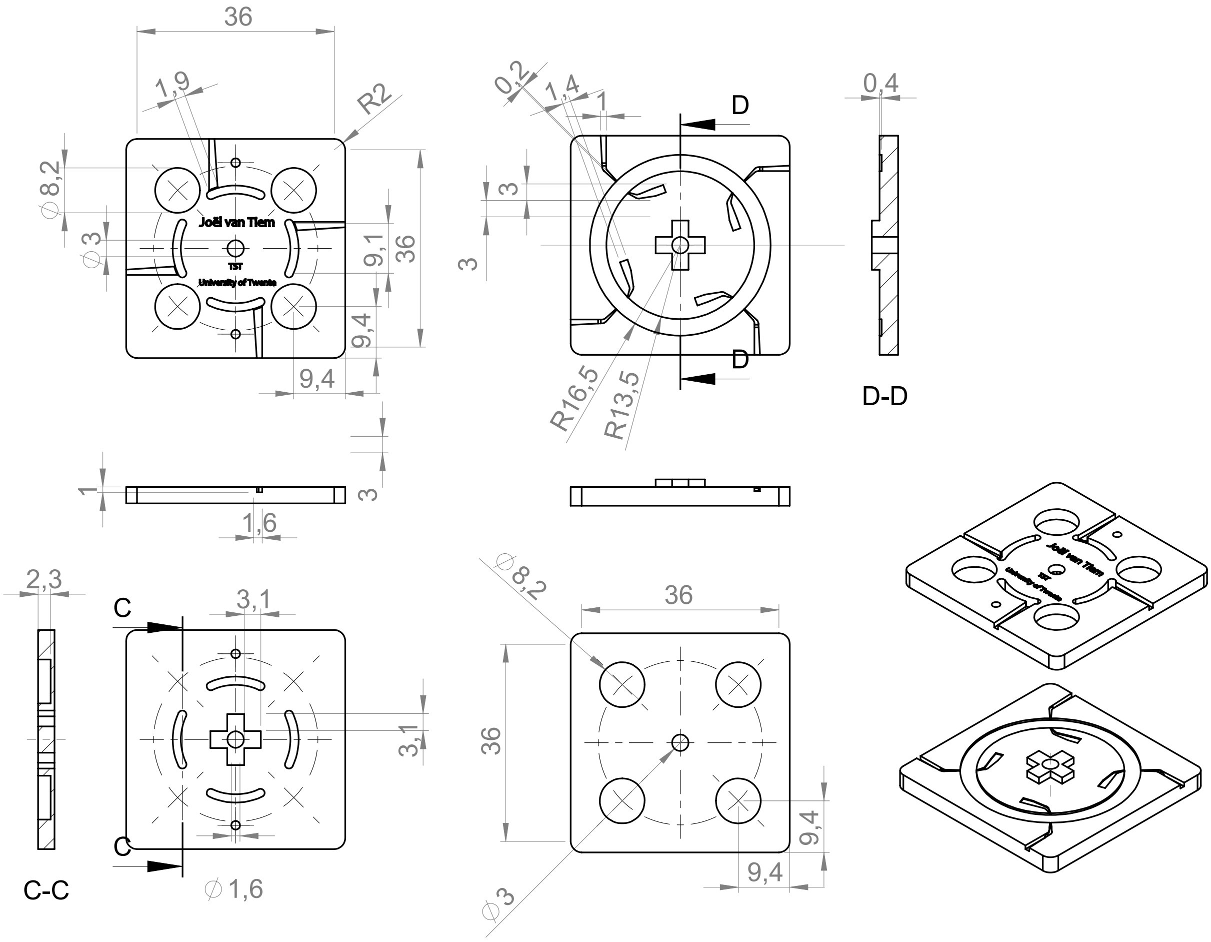

FIGURE F.1: The angular acceleration sensor. Left: top, right: bottom. The fluid channel cross section can be seen in cut D-D.

F.2 Rectangular flow sensor V1

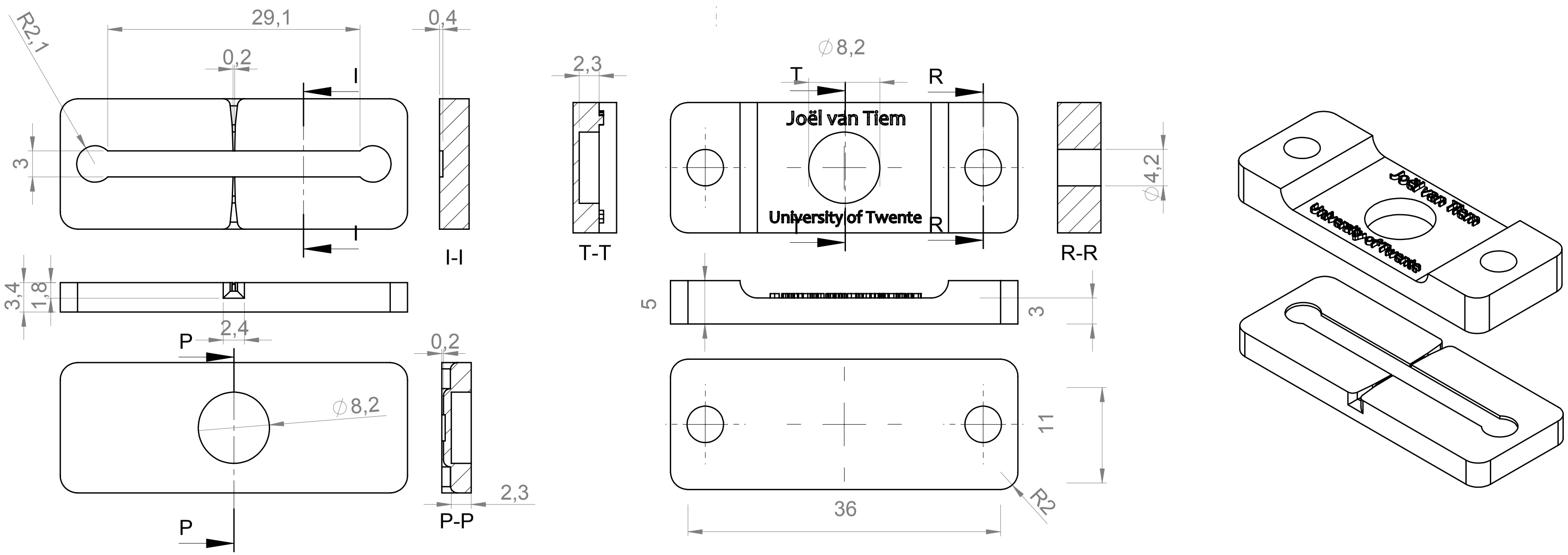

FIGURE F.2: The first version of the rectangular flow sensor. Left: bottom, right: top. The fluid channel cross section can be seen in cut I-I.

F.3 Rectangular flow sensor V2

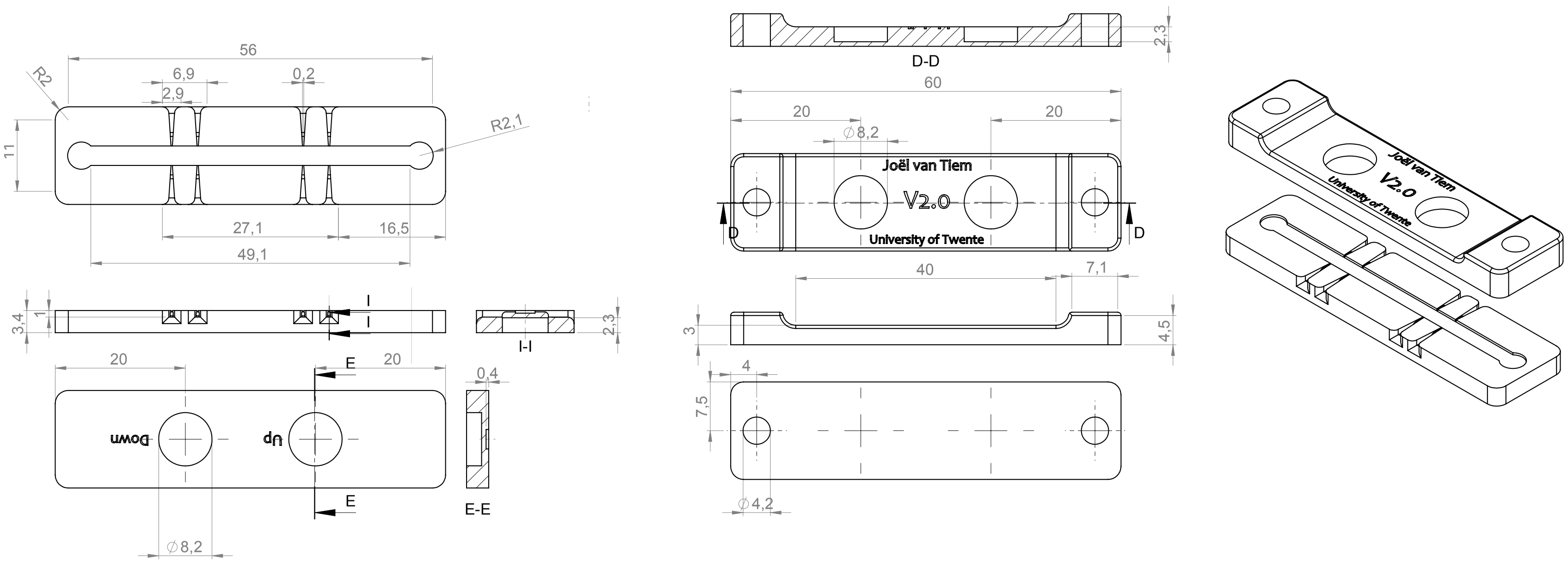

FIGURE F.3: The second version of the rectangular flow sensor. Left: bottom, right: top. The fluid channel cross section can be seen in cuts I-I and E-E.

F.4 Chip inlet unit

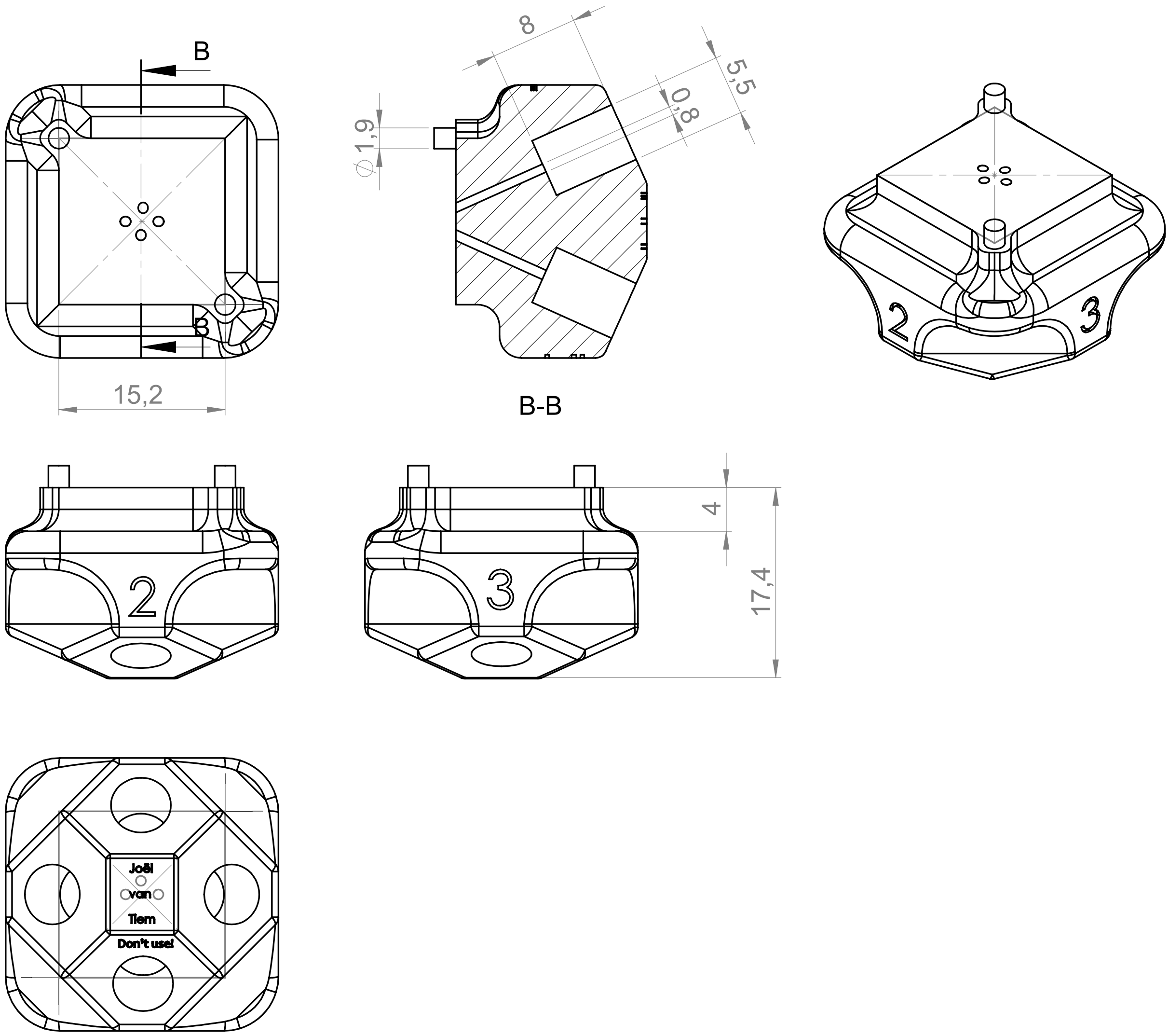

FIGURE F.4

Bibliography

[1] Harmen Droogendijk. Bio-inspired mems flow and inertial sensors. 2014.

[2] M Dijkstra, MJ de Boer, JW Berenschot, TSJ Lammerink, RJ Wiegerink, and M Elwenspoek. Miniaturized thermal flow sensor with planar-integrated sensor structures on semicircular surface channels. *Sensors and Actuators A: Physical*, 143(1):1–6, 2008.

[3] J Groenesteijn, H Droogendijk, MJ de Boer, RGP Sanders, RJ Wiegerink, and GJM Krijnen. An angular acceleration sensor inspired by the vestibular system with a fully circular fluid-channel and thermal read-out. 2014.

[4] M Ashauer, H Glosch, F Hedrich, N Hey, H Sandmaier, and W Lang. Thermal flow sensor for liquids and gases based on combinations of two principles. *Sensors and Actuators A: Physical*, 73(1):7–13, 1999.

[5] BW Van Oudheusden. Silicon thermal flow sensor with a two-dimensional direction sensitivity. *Measurement Science and Technology*, 1(7):565, 1990.

[6] Edwin H Hall. On a new action of the magnet on electric currents. *American Journal of Mathematics*, 2(3):287–292, 1879.

[7] C.R. Westgate Chia Ling Chien. The hall effect and its applications. 1980.

[8] HyeunJoong Yoon, SoonYoung Kim, SangWoo Lee, and Sang S Yang. Fabrication of a microelectromagnetic flow sensor for microflow rate measurement. In *SPIE's 7th Annual International Symposium on Smart Structures and Materials*, pages 264–271. International Society for Optics and Photonics, 2000.

[9] Bruce Roy Munson, Donald F Young, and Theodore Hisao Okiishi. *Fundamentals of fluid mechanics.* New York, 1990.

[10] John Robert Taylor. *Classical mechanics.* University Science Books, 2005.

[11] Hermann Schlichting. Boundary-layer theory. 1968.

[12] R.M.E.J. Spiering H. Tijdeman. *Solid Mechanics, part 2.* University of Twente lecture notes, 2005.

[13] Tarik Bourouina and Jean-Paul Grandchamp. Modeling micropumps with electrical equivalent networks. *Journal of Micromechanics and Microengineering*, 6(4):398, 1996.

[14] Kazuyuki Ohe and Yoshihide Naito. A new resistor having an anomalously large positive temperature coefficient. *Japanese Journal of Applied Physics*, 10(1):99, 1971.

[15] AG Aleniëtěsyn and EI Butikov. *Concise handbook of mathematics and physics.* CRC Press (Boca Raton, Fla. and Moscow), 1997.

[16] JW van Honschoten, GJM Krijnen, VB Svetovoy, HE de Bree, and MC Elwenspoek. Analytic model of a two-wire thermal sensor for flow and sound measurements. *Journal of Micromechanics and Microengineering*, 14(11):1468, 2004.

[17] JW van Honschoten, GJM Krijnen, VB Svetovoy, H-E de Bree, and MC Elwenspoek. Optimisation of a two-wire thermal sensor for flow and sound measurements. In *Micro Electro Mechanical Systems, 2001. MEMS 2001. The 14th IEEE International Conference on*, pages 523–526. IEEE, 2001.

[18] Joost W van Honschoten, Vitaly B Svetovoy, Gijs JM Krijnen, and Miko C Elwenspoek. Optimization of a thermal flow sensor for acoustic particle velocity measurements. *Microelectromechanical Systems, Journal of*, 14(3):436–443, 2005.

[19] Theo SJ Lammerink, Niels R Tas, Miko Elwenspoek, and Jan HJ Fluitman. Micro-liquid flow sensor. *Sensors and Actuators A: Physical*, 37:45–50, 1993.

[20] DC Mattis and John Bardeen. Theory of the anomalous skin effect in normal and superconducting metals. *Physical Review*, 111(2):412, 1958.

[21] Harold A Wheeler. Formulas for the skin effect. *Proceedings of the IRE*, 30(9):412–424, 1942.

[22] John Arthur Shercliff. *The theory of electromagnetic flow-measurement.* CUP Archive, 1962.

[23] Alexander Kolin. An alternating field induction flow meter of high sensitivity. *Review of Scientific Instruments*, 16(5):109–116, 1945.

[24] Supermagnete. Calculation of magnetic flux density. *http://www.supermagnete.de/*, August 2014.

[25] JM Camacho and V Sosa. Alternative method to calculate the magnetic field of permanent magnets with azimuthal symmetry. *Revista mexicana de física E*, 59(1):8–17, 2013.

[26] Hiroyuki Ohshima. Electrical double layer. *Surfactant science series*, pages 1–18, 1998.

[27] David C Grahame. The electrical double layer and the theory of electrocapillarity. *Chemical Reviews*, 41(3):441–501, 1947.

[28] Itamar Borukhov, David Andelman, and Henri Orland. Steric effects in electrolytes: A modified poisson-boltzmann equation. *Physical review letters*, 79(3):435, 1997.

[29] E. Hückel P. Debye. *Physik*, 35(183), 1923.

[30] Yongan Gu and Dongqing Li. The ζ-potential of glass surface in contact with aqueous solutions. *Journal of Colloid and Interface Science*, 226(2):328–339, 2000.

[31] P Fievet, M Sbaı, A Szymczyk, and A Vidonne. Determining the< i> ζ</i>-potential of plane membranes from tangential streaming potential measurements: effect of the membrane body conductance. *Journal of membrane science*, 226(1):227–236, 2003.

[32] Andriy Yaroshchuk and Volker Ribitsch. Role of channel wall conductance in the determination of ζ-potential from electrokinetic measurements. *Langmuir*, 18(6):2036–2038, 2002.

[33] Carsten Werner, Ralf Zimmermann, and Thomas Kratzmüller. Streaming potential and streaming current measurements at planar solid/liquid interfaces for simultaneous determination of zeta potential and surface conductivity. *Colloids and Surfaces A: Physicochemical and Engineering Aspects*, 192(1):205–213, 2001.

[34] Wouter Olthuis, Bob Schippers, Jan Eijkel, and Albert van den Berg. Energy from streaming current and potential. *Sensors and Actuators B: Chemical*, 111:385–389, 2005.

[35] Shapeways. 3d printing. *http://www.shapeways.com/*, September 2014.

[36] J Haneveld, TSJ Lammerink, MA Dijkstra, H Droogendijk, MJ de Boer, and RJ Wiegerink. Highly sensitive micro coriolis mass flow sensor. 2008.

[37] M Dijkstra, MJ De Boer, JW Berenschot, TSJ Lammerink, RJ Wiegerink, and M Elwenspoek. A versatile surface channel concept for microfluidic applications. *Journal of Micromechanics and Microengineering*, 17(10):1971, 2007.

[38] J Haneveld, TSJ Lammerink, MJ De Boer, RGP Sanders, Aditya Mehendale, JC Lötters, M Dijkstra, and RJ Wiegerink. Modeling, design, fabrication and characterization of a micro coriolis mass flow sensor. *Journal of Micromechanics and Microengineering*, 20(12):125001, 2010.

[39] George Green. *An essay on the application of mathematical analysis to the theories of electricity and magnetism*, volume 3. 1889.

[40] SS Bayin. Mathematical methods in science and engineering. 2006. *John Wiley&Sons, New York*.